Laser-Induced Graphene Electrochemical Sensors: Plasma Treatment, Lithium-Ion Detection via Printed Surface Modification, and Integrated 3D Printed Microfluidics

SAUMIK DEY SHOVAN

A THESIS SUBMITTED TO THE FACULTY OF GRADUATE STUDIES IN PARTIAL FULFILLMENT OF THE REQUIREMENTS FOR THE DEGREE OF MASTER OF APPLIED SCIENCE

GRADUATE PROGRAMME IN ELECTRICAL ENGINEERING AND COMPUTER SCIENCE YORK UNIVERSITY TORONTO, ONTARIO

JUNE 2025

Abstract

Laser-induced graphene (LIG) has gained attention as a cost-effective and sustainable alternative to traditional electrochemical sensing electrodes. It enables a simple, one-step fabrication process that eliminates the need for complex materials or procedures. While LIG has attracted significant attention for various sensing applications, its potential for lithium detection remains largely unexplored. Lithium detections are particularly noteworthy given that monitoring is an essential priority in both industrial processes and medical diagnostics. One known limitation of LIG is its hydrophobic surface, which limits sensor performance and was addressed in the first part of this study. Although plasma treatment has been used to improve LIG's surface wettability, the effect of treatment duration has not been fully explored. Overexposure can introduce surface defects and reduce conductivity. We optimized plasma treatment time to improve surface reactivity while preserving the structural and electrical properties of LIG. In the second part of this study, we developed a lithium-selective sensor to address the increasing demand for reliable lithium detection. To achieve lithium selectivity, we functionalized the LIG electrode with lithium manganese oxide (LMO) using dispense printing for better uniformity of the printed layer. LMO is chosen for its strong interaction with lithium ions. This thesis is the first report of LMO being combined with LIG for lithium sensing. Finally, this study introduced a fully additively manufactured electrochemical sensor that integrated functionalized LIG electrodes with 3D-printed microfluidic channels. By enabling both the formation of conductive LIG patterns and the 3D printing of microfluidic structures directly onto a 3D-printed substrate, this approach removes the need for complex alignment or assembly steps. The successful result is a compact, efficient, and scalable sensing platform that combines the strengths of LIG, lithium-selective functionalization, and additive manufacturing for practical and selective lithium detection.

Acknowledgements

I want to take this opportunity to express my deepest gratitude to all those who supported and guided me throughout this journey. First and foremost, I thank the Almighty for granting me good health, strength, and the opportunity to pursue this work.

I am profoundly grateful to my two exceptional supervisors, Dr. Gerd Grau and Dr. Pouya Rezai. Their unwavering support, encouragement, and insightful guidance have shaped me into the researcher I am today. From the very beginning, their mentorship has been instrumental in helping me navigate challenges and grow both academically and personally. I am incredibly fortunate to have worked under their supervision.

I would also like to sincerely thank Dr. Sylvie Morin for serving on my supervisory committee. My sincere thanks also go to Dr. Cuiying Jian for kindly agreeing to chair my oral examination.

I want to thank Veronica Di Cecco at the Royal Ontario Museum for her assistance with the Raman spectroscopy analysis. I also thank James Freemantle from York University for training me in scanning electron microscopy and Peter Brodersen from the University of Toronto for his help with X-ray photoelectron spectroscopy. I'm grateful to Dr. Xin (Shane) Guo for providing me access to the profilometry equipment.

I gratefully acknowledge the support of the Natural Sciences and Engineering Research Council of Canada (NSERC) and the York University Catalyzing Interdisciplinary Research Cluster for Detection and Remediation of Water Contaminants (CIRC-DRWC).

I would like to give special thanks to all my lab mates for creating a supportive and collaborative environment. I would especially like to thank Mohamad, whose help and friendly guidance made lab work more enjoyable and productive. I would also like to thank Dr. Shapour Jafargholinejad,

a research associate at York University, for mentoring me and offering constant support and encouragement.

Finally, I am deeply thankful to my family and friends. I am especially grateful to my parents, whose unwavering love, patience, and strength have supported me through every stage of this journey. Their constant encouragement made this accomplishment possible.

Table of Contents

List of Tables

List of Figures

Nomenclature

Symbol / Abbreviation	Description
CE	Counter electrode
C_{dl}	Electric double-layer capacitance
CV	Cyclic voltammetry
ΔI_p	Difference between anodic and cathodic peak current
EIS	Electrochemical impedance spectroscopy
FDM	Fused deposition modelling
GCE	Glassy carbon electrode
I_D/I_G	Ratio of D and G peaks after baseline correction from Raman spectroscopy (~1350 cm^{-1} and ~1580 cm^{-1})
K^+	Potassium ion
$K_3[Fe(CN)_6]$	Potassium ferricyanide
$K_4[Fe(CN)_6]\cdot 3H_2O$	Potassium hexacyanoferrate trihydrate (II) ($\cdot 3H_2O$)
KCl	Potassium chloride
Li^+	Lithium ion
LiCl	Lithium chloride
LIG	Laser-induced graphene
LMO	Lithium manganese oxide (Li_2MnO_4)
LOB	Limit of blank
LOD	Limit of detection
LOD_{conc}	Limit of detection in terms of concentration
$LOD_{current}$	Limit of detection in terms of current
LOQ	Limit of quantification
Na^+	Sodium ion
NaCl	Sodium chloride
PDMS	Polydimethylsiloxane
PEI	Polyetherimide
PI	Polyimide film
RE	Reference electrode
R_{ct}	Charge transfer resistance
R_s	Solution resistance

SEM	Scanning electron microscopy
SPE	Screen-printed electrode
WE	Working electrode
W_e	Warburg element
XPS	X-ray photoelectron spectroscopy
$(mean)_{blank}$	Mean response of blank sample
$(SD)_{blank}$	Standard deviation of five blank measurements
$(SD)_{low\ concentration\ sample}$	Standard deviation of response from a low concentration sample above the blank level

1 Introduction

1.1 Motivation of this research

Electrochemical sensing is becoming an important tool because it is simple to use, easy to access, and able to deliver rapid and reliable analysis [1]. These features make it useful in many areas, such as environmental monitoring, healthcare, food quality control, medical diagnostics, and industrial safety [2], [3], [4]. An important step in developing electrochemical sensors is the fabrication of electrodes, as their design and fabrication methods directly affect the sensor's performance and practicality. Fabrication techniques such as screen printing, electrodeposition, inkjet printing, and graphene pasting often involve complex processes and high costs, limiting scalability and practical deployment [5]. In comparison, laser-induced graphene (LIG) offers a more straightforward approach that may reduce fabrication complexity and cost, contributing to developing a user-friendly and easy-to-use sensing platform [6]. LIG has shown strong potential for electrochemical sensing due to its conductivity and ease of fabrication. However, its hydrophobic surface limits effective interaction with aqueous electrolytes, which reduces sensing efficiency. Plasma treatment can improve surface wettability and promote better electrochemical activity, but the duration of exposure plays a critical role. Insufficient treatment may not provide meaningful improvement, while overexposure can damage the LIG structure and reduce conductivity. The first part of this study is motivated by the need to identify an optimal treatment window that enhances wettability while preserving the structural and electrical integrity of the LIG network to improve sensing performance.

While this part focuses on improving LIG's surface properties, a separate and equally important goal is to apply LIG to detect specific target analytes.

The growing demand for accurate lithium detection across industrial and medical sectors underscores the need for low-cost, accessible sensing solutions. Lithium plays a critical role in battery manufacturing, where monitoring is essential for quality assurance and environmental compliance. In healthcare, lithium is prescribed for psychiatric treatment, requiring precise dosage control to prevent adverse effects [7]. Additionally, the increase in lithium extraction and recycling emphasizes the need for reliable detection tools[8]. However, existing lithium sensors are often costly and involve complex fabrication methods. The second part of this study is motivated by the opportunity to develop a cost-effective and straightforward LIG-based sensor that can facilitate lithium monitoring and contribute to ongoing advancements in this field.To translate the sensing platform into a practical and scalable device, the final part of this study is motivated by the need for a simplified and cost-effective method to integrate LIG-based electrodes with microfluidic structures for lithium sensing. While microfluidic integration offers benefits such as low sample consumption, enhanced analyte transport, and potential for portability, conventional fabrication approaches often involve separate processing steps that are costly, time-consuming, and prone to bonding issues [9]. This motivates the exploration of an integrated fabrication strategy combining 3D printing with LIG electrode induction that can streamline the process and support the development of compact, application-ready electrochemical sensing platforms.

1.2 Graphene: Overview and Applications

Graphene, known for its excellent electrical and thermal conductivity, is a unique form of carbon made of a single layer of atoms arranged in a honeycomb pattern. Carbon allotropes like graphite, carbon nanotubes, and fullerenes are made of these single-layer carbon atoms. Figure 1.1 shows a graphene layer with carbon atoms forming a honeycomb pattern, bonded through sp^2 hybridization. Graphene's honeycomb lattice structure arises from the sharing of sp^2 electrons between carbon atoms. Each unit cell consists of two carbon atoms, with a lattice constant of 2.46 Å and an interatomic covalent bond length of 1.42 Å. Weak van der Waals forces hold together several layers present in multi-layer graphene [10]. Graphene shows exceptional mechanical strength, flexibility, and high electrical and thermal conductivity because of sp^2 bonding in its structure**.** The sp^2 hybridization creates a delocalized π-electron system above and below the graphene sheet, enabling the free flow of electrons [11].

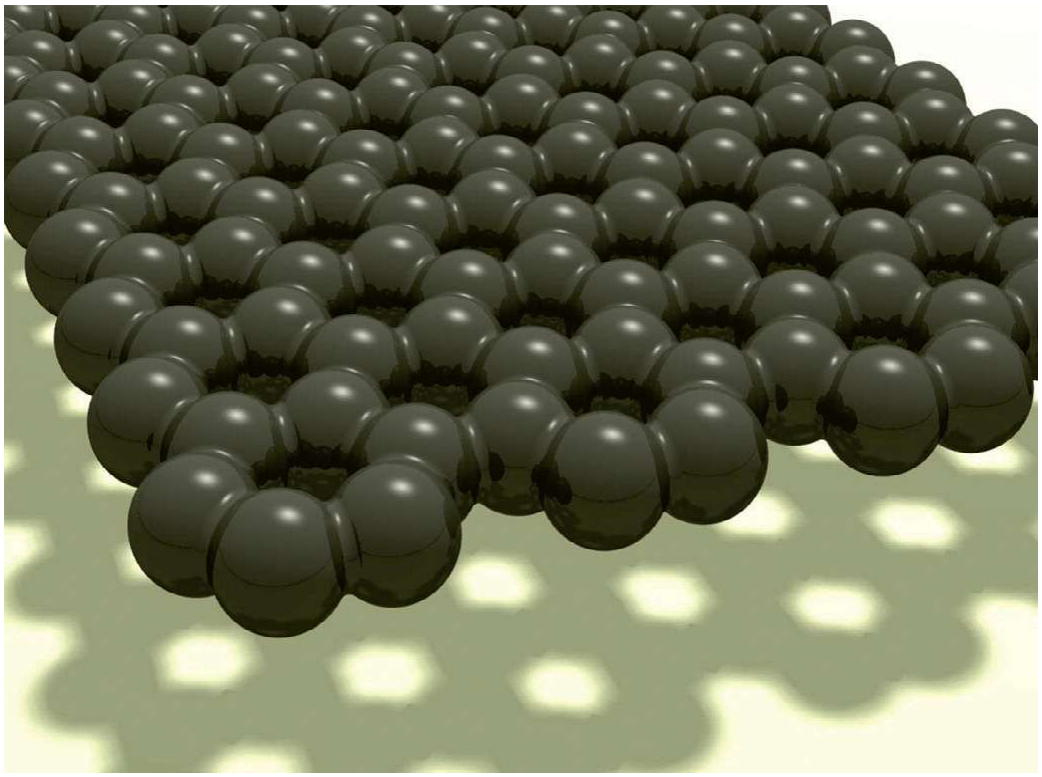

Figure 1.1 Graphene as a monolayer of graphite, consisting of sp²-bonded carbon atoms arranged in a honeycomb lattice. Reproduced with permission from Elsevier[12]. License Number: 6007330604193

Graphene is a lightweight and flexible material with good electrical and thermal conductivity. These properties make graphene valuable in light and bendable electronics like displays and circuits [13]. Another important use of graphene is in energy storage, where it is used in supercapacitors because it can store more energy, charge fast, and last longer, helping improve batteries for renewable energy and portable devices [14]. Graphene's biocompatibility and antibacterial nature make it helpful for drug delivery, biosensors, and advanced medical imaging. It adds strength without extra weight to cars and aircraft, making them efficient and durable [15]. As an electrode material which is relevant to this thesis, graphene is used in electrochemical sensors impacting healthcare, environmental monitoring, and industry [16].

1.3 From Graphene to LIG: Fundamentals and Fabrication

LIG is an emerging graphene fabrication method that uses laser energy to convert carbon-based precursor materials into a porous graphene structure. The precursor material can be commercially available or fabricated using 3D printing. Figure 1.2 presents a schematic of the LIG fabrication process, along with the scanning electron microscopy (SEM) image showing the fabricated LIG's porous structure.

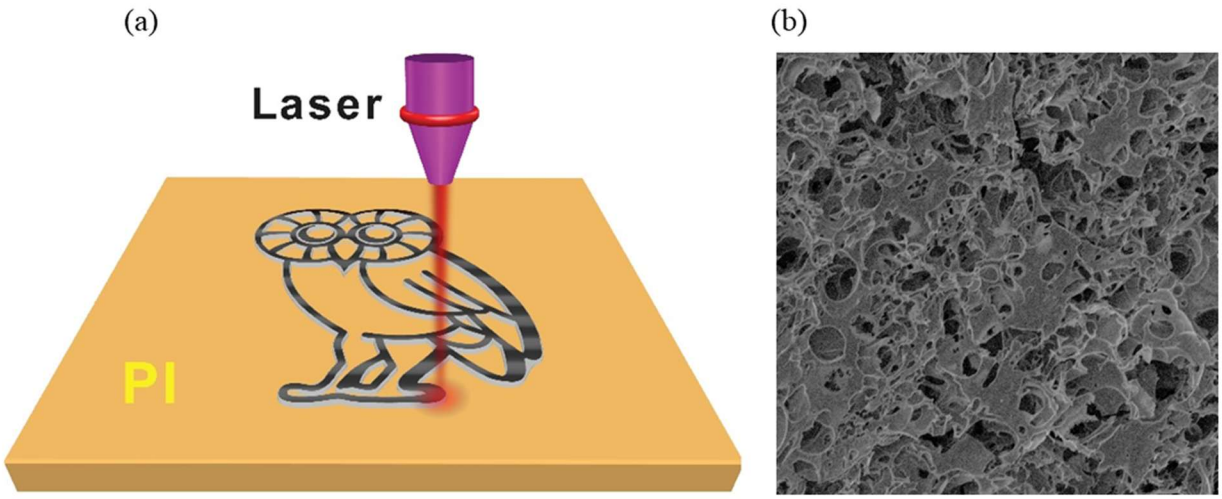

Figure 1.2. (a) Schematic representation of the LIG fabrication process on a polyimide (PI) film and (b) SEM image showcasing the scribed graphene structure.

This technology mainly produces graphene networks that are conductive, porous, and three-dimensional, with unique physical and chemical properties [17]. Compared to other graphene synthesis methods, LIG stands out as a cost-effective, scalable, and environmentally friendly technique that enables the direct writing of graphene onto various substrates, making it highly suitable for diverse applications.

LIG is formed through the photothermal conversion of carbonaceous materials such as polyimide (PI), polyetherimide (PEI), phenolic resin, wood, paper, cork, polysulfone (PSU), lignin, and even certain biopolymers and fabrics, using a laser source, a method increasingly applied to substrates prevalent in 3D printing [18]. This process involves localized heating, which breaks chemical bonds and forms a highly porous graphene. The laser selectively ablates and converts the top layer of the precursor material into a graphitized structure without requiring additional catalysts [17]. This method eliminates the need for complex chemical processing or high-temperature environments, making it an attractive alternative for fabricating electrode materials in electrochemical applications, including sensors, supercapacitors, and energy storage devices [19].

1.4 Applications of LIG

The key characteristics of LIG that have made it a promising material for diverse applications are:

Porous Structure: LIG features a three-dimensional porous graphene network that can enhance the electrochemical performance of electrodes with large surface area, which facilitates ion transport [20].

High Conductivity: The sp^2-hybridized carbon network of LIG contributes to its high electrical conductivity, making it suitable for electronic and sensing applications [14].

Tunable Properties: The material properties of LIG can be tuned for specific applications by changing the laser processing parameters like scan speed, power, and wavelength [17].

Due to its unique structural and electrochemical properties, LIG is gaining attention as a promising alternative to conventional graphene-based electrodes, making it an emerging material in various

fields. LIG is increasingly utilized in energy storage, sensing technologies, environmental monitoring, and biomedical applications. Numerous studies have demonstrated its effectiveness in these areas, showing its potential to enhance existing technologies and drive further advancements in electrode design. For instance, Minhas-Khan et al. [14] investigated the application of LIG as an electrode material for micro-supercapacitors. In their study, they demonstrated the utility of LIG fabricated with optimized laser power as a suitable candidate for energy storage applications. The prepared micro-supercapacitor devices showcased enhanced electrochemical performance, highlighting LIG's effectiveness in improving charge storage capabilities. A recent review from Lee et al. [21] demonstrates how LIG can be used in energy storage for wearables, implants, and drug delivery devices. The review offers a comparative analysis of LIG with traditional graphene and further discusses the challenges involved in LIG's applications in these sectors. Another review article [22] explores the synthesis and applications of LIG in electrochemical energy conversion and storage. It discusses key factors affecting LIG formation and its role in hydrogen evolution reaction, oxygen evolution reaction, and overall water splitting. The review also highlights LIG's use in oxygen reduction and zinc-air batteries, along with the efficiency of non-noble metal-based LIG hybrid materials (Figure 1.3).

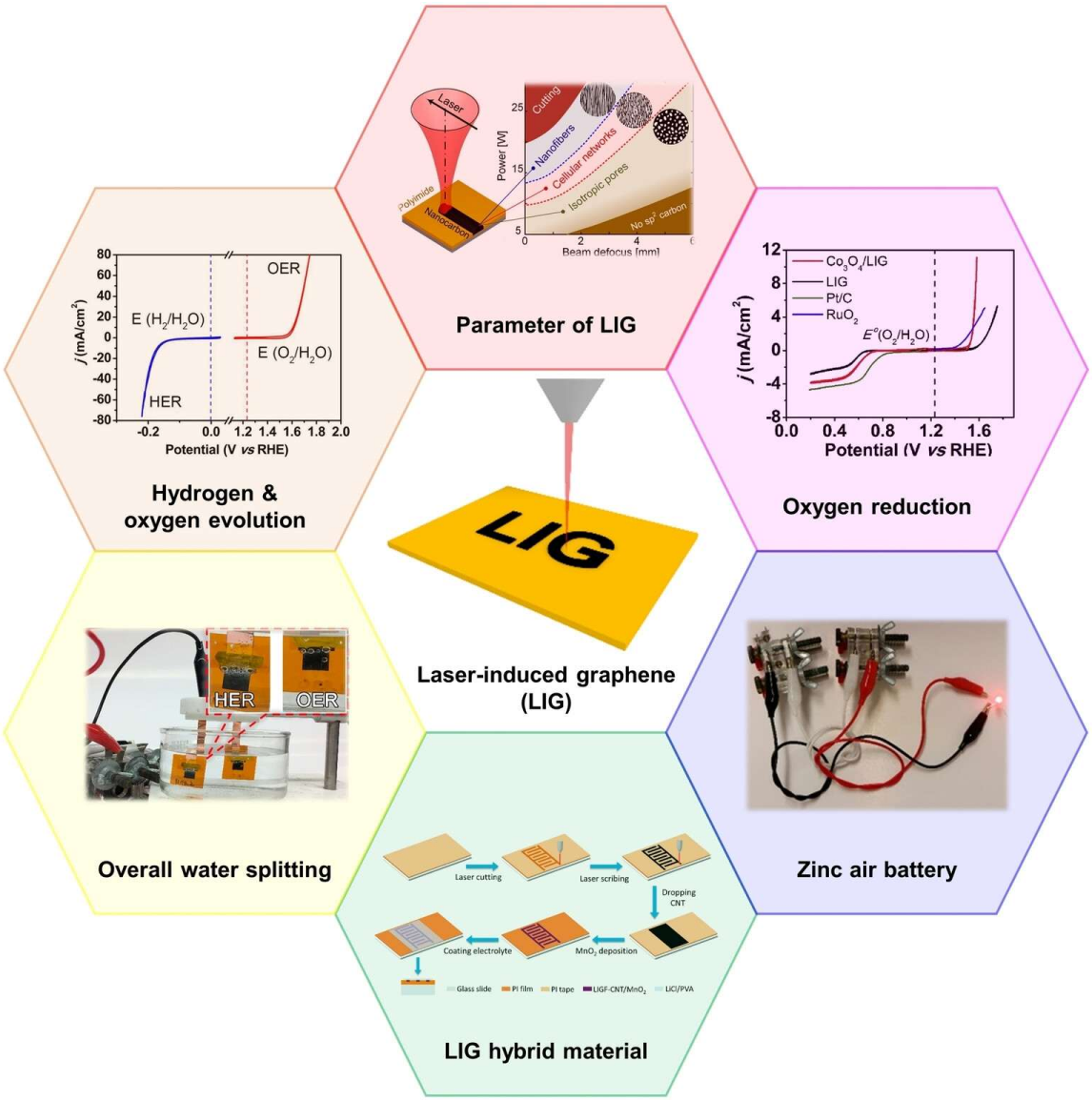

Figure 1.3. Schematic illustration of the LIG, its parameter, and its applications in the electrochemical system. Image reused with permission from John Wiley and Sons. License Number: 6007371325472 [22].

LIG-based biosensors showed great promise in non-invasive health monitoring by detecting glucose, lactate, and other biomarkers in bodily fluids. One of the key studies in this sector fabricated disposable sensors capable of detecting Na^+ in sweat using UV-Ozone irradiated

potentiometric LIG-based electrodes [23]. The ion response time for the sensing was ~1 min that shows its potential as a fast, non-invasive sweat-sensing wearable device. A study by Lee et al. [24] introduced a multifunctional LIG-based wearable sensor capable of simultaneously monitoring Na^+ and K^+ ion concentrations and detecting physical strain. The sensor was fabricated by UV-laser patterning on a composite substrate made of PDMS and lignin. It demonstrated high sensitivity, achieving 63.6 mV dec^{-1} for Na^+ and 59.2 mV dec^{-1} for K^+, highlighting its potential for real-time health monitoring applications. LIG has also been explored for non-invasive health monitoring, particularly in urine analysis. Kucherenko et al. [25] developed LIG-based ion-selective electrodes for detecting K^+ and NH_4^+ ions in urine, aimed at monitoring patient hydration levels. The sensors were fabricated by integrating ion-selective membranes with LIG electrodes, forming a potentiometric sensing platform. LIG has also shown great potential in flexible electronics. For example, a study demonstrated LIG-based strain gauges fabricated under UV laser irradiation, which exhibited high sensitivity and a widely tunable sensing range [26]. A pressure sensor combining LIG and multi-walled carbon nanotubes was developed, demonstrating outstanding performance [27]. The sensor exhibited high sensitivity (2.41 kPa^{-1}), a low detection limit (approximately 1.2 Pa), fast response and recovery time (as quick as 2 ms), and excellent durability over more than 2,000 cycles. All these findings reported here emphasize the potential of LIG in diverse fields, such as energy storage, biosensing, and flexible electronics. Beyond these applications, LIG also showed significant promise as an electrochemical sensing material, which is explored in detail in the following section.

1.5 Electrochemical Sensors with LIG Electrodes

Electrochemical sensing is a widely used analytical technique for detecting and quantifying chemical species based on their electrochemical properties. An electrochemical sensor converts electrochemical interactions such as redox (reduction and oxidation) reactions into measurable electric signals, enabling precise analysis [28]. Typically, a standard electrochemical sensor consists of three electrodes—working, reference, and counter—immersed in an electrolyte, where reaction kinetics at the electrode/electrolyte interface generate signals in the form of current, voltage, or impedance [29]. Working electrode (WE) is the primary sensing area where the analyte undergoes reactions like oxidation and reduction, producing electrical signals that can be measured to understand the analyte's signature behavior, like the presence of any target analyte or concentration [30]. Reference electrode (RE) ensures accurate and reproducible measurements by compensating for any fluctuations in the system by providing a stable and known potential against which the response from the WE is measured [31]. The counter electrode (CE) allows current to flow through the electrochemical cell, and, as a result, it completes the circuit. It undergoes an opposite reaction to support the redox reaction happening at the WE and helps maintain the flow of electrons without affecting the potential measured at the reference electrode. Another primary function of the CE is to minimize the interference of the RE in the electrochemical sensor [32].

Various types of electrodes are used in electrochemical sensing, each offering distinct advantages based on the application, along with some disadvantages. Below is a summary of widely used electrode materials and their use in different studies, followed by a discussion on how LIG can help address some of the electrode shortcomings in electrochemical detection.

1. Screen Printed Electrode (SPEs): SPEs are one of the most common electrode materials, the first for paper analytical devices [33]. Plenty of studies reported the use of SPEs for different analytical purposes. For example, Hong et al. [34] reported the successful detection of nitrate ions with SPEs as the sensor's working electrode. Using SPEs as amperometric detector a rapid and simple method was reported by Begamini et al. [35] for procaine determination. Another review article from Li et al. [36] reported the use of SPEs for different environmental analyses, including the detection of heavy metal ions, pesticides/herbicides, and phenolic compounds. In their review, they summarized research on this matter and also reported the modification of SPEs for the specific detection condition. SPEs pose advantages including easy to operate and on site and real time sensing. However, several challenges are associated with SPEs for sensing technologies. Common issues are inconsistency and reproducibility, which often arises from variations in ink composition, printing precision, and curing conditions. Although SPEs are often considered low-cost, the fabrication process can be resource-intensive when high precision and customization are required. Moreover, tailoring the electrode surface with affinity reagents for specific sensing applications, such as antibodies for biodetection and transition metal oxides for precious metal sensing, is not always straightforward and may involve complex modification steps [37].
2. Graphene Based Electrodes: Graphene has remained one of the top choices for the electrochemical sensor electrodes for years due to its unique physiochemical properties as discussed in section 1.2. There are numerous studies where scientists reported the use of

graphene as the electrode material for the electrochemical sensor. For instance, Benjamin et al. [38] reviewed the use of graphene for the electrochemical detection of environmental pollutants like heavy metals, steroid compounds, antibiotic residues, and pesticides. Another study from Adhikari et al. [39] showed detection of acetaminophen with graphene-based electrochemical sensor. Although single-layer graphene showed great promise in electrochemical sensing due to its excellent conductivity and surface properties, producing it through traditional methods is not always simple or practical. Standard fabrication techniques such as chemical exfoliation of graphite, reduction of graphene oxide, or use of graphene nanoplatelet pastes often involve complex chemical processes and multiple preparation steps [40]. These approaches can be time-consuming, inconsistent, and difficult to scale, making them less suitable for routine or large-scale sensor development.

3. Glassy Carbon Electrodes (GCE): GCE is a type of solid, carbon-based electrode known for its smooth surface, chemical stability, and wide potential window. It is commonly used in electrochemical sensing because it provides reliable performance and can be easily modified with other materials to improve sensitivity. GCEs are commonly used in electrochemical sensing due to their stability and ease of modification. For instance, Murugan et al. [41] reported the electrocatalytic reduction of hydrogen peroxide (H_2O_2) on an activated GCE. Salimi et al. [42] reported the electrochemical detection of trace amounts of arsenic(III) using a GCE modified with cobalt oxide nanoparticles. Although the modification of GCE is straightforward, it poses some challenges, such as difficulties in

achieving consistent surface preparation due to their brittleness, tendency for surface contamination, and a relatively low active surface area without modification.

4. Other electrode materials: Along with commonly used materials like SPEs, GCEs, and graphene, other electrodes such as gold, platinum, indium tin oxide (ITO), and metal oxides like cobalt oxide (Co_3O_4), zinc oxide (ZnO), and manganese dioxide (MnO_2) are also used in electrochemical sensing [43]. These materials can offer good sensitivity, conductivity, and biocompatibility. However, they are often expensive and require more complicated fabrication steps, which makes them less practical for large-scale or low-cost sensor development [44].

All the electrode materials mentioned above showed effectiveness in their respective way. However, there is increasing interest in novel alternatives that offer enhanced performance and greater scalability with a simple fabrication process. One such alternative material is LIG, which leverages the unique properties of laser-induced carbonization [45] [46]. LIG's binder-free nature and minimal material wastage make it a more efficient, sustainable, and accessible option for producing intricate, high-performance carbon or graphene-based electrodes for electrochemical sensing. Numerous studies demonstrated the utilization of LIG as the electrode material for electrochemical sensing. For instance, Park et al. [47] showed the development of an efficient and sensitive electrochemical sensor to detect dopamine. In their study, a PI film was first coated with CeO_2 and subjected to UV/ozone treatment before being patterned into electrodes using a CO_2 laser. Cyclic voltammetry (CV), electrochemical impedance spectroscopy (EIS), and differential pulse voltammetry (DPV) were used to evaluate electrochemical reactions. Another study from

Fenzl et al. [45] showed an example of a LIG-based aptasensor coupling pyrene butyric acid with a thrombin aptamer. They reported a highly sensitive and reliable biosensor by anchoring pyrene butyric acid onto graphene, enabling the covalent attachment of a thrombin-specific aptamer to the carboxyl groups. This biosensor achieved remarkably low detection limits of 1 pM in the buffer and 5 pM in the complex serum matrix. Beuer et al. [46] fabricated a LIG-based sensing platform for multi-analyte detection in human sweat. The outcome of their study showed that LIG can enable all three electrochemical sensing strategies—voltammetry, potentiometry, and impedance, within one system, highlighting its versatility for sweat analysis applications. Another study by Liu et al [48] demonstrated the use of LIG in medical sensors designed for health monitoring and disease diagnosis. Their study highlighted its applications in biochemical sensing, including the detection of ions, small molecules, microRNAs, proteins, and cells. Chiara et al. [49] reported the development of a high-performance electrochemical sensor by incorporating a metal-organic framework-derived $Co/Co_3O_4/C$ core-shell composite into LIG electrodes. In their design, cobalt-based nanoparticles with a core-shell structure consisting of metallic cobalt (Co) at the core and cobalt oxide (Co_3O_4) as the shell were embedded in a conductive carbon matrix, enhancing electrochemical activity. This process formed a porous, nitrogen-doped carbon network uniformly decorated with Co/Co_3O_4 nanoparticles. The resulting sensor exhibited significantly reduced impedance and a 400-fold increase in specific capacitance, efficient charge transfer, and low interfacial resistance. LIG has also been successfully integrated with microfluidic platforms to create efficient and compact sensing systems. Integrating microfluidics with electrodes enables improved analyte transport and contributes to better overall sensor functionality. Several studies

demonstrated the potential of using LIG electrodes within microfluidic channels for electrochemical sensing. For example, a microfluidic sensing platform with LIG-based electrodes was presented by Wagh et al. [50], integrating interdigitated electrodes (IDE) and a microchannel on the same platform which functioned as a taste sensor. Figure 1.4 shows the microchannel's design and the device's interdigitated electrodes used in the research. The LIG-IDE device demonstrated a detection limit lower than the human sensory threshold, showcasing its high sensitivity.

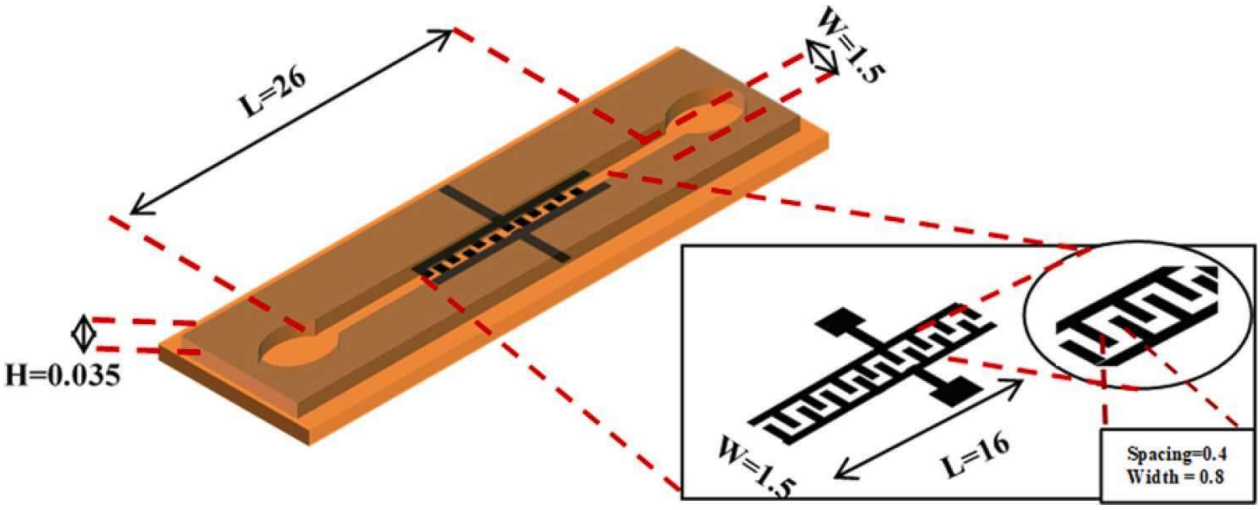

Figure 1.4. Schematic illustration of the device showing the microchannel design integrated with interdigitated electrodes used as taste sensors. Reused with permission from Elsevier. License number: 6010411447296, License date: April 15, 2025 [50].

Liu et al. [48] developed a flexible electrochemical microfluidic chip by directly writing a LIG electrode array onto a PI film and then integrating the microchannel with it. Integrating LIG with the microfluidic channel enabled high-throughput and multiplex detection of miRNAs with high sensitivity and selectivity. However, despite the effective integration of microfluidics and LIG, the microchannel fabrication mostly relied on PDMS-based soft lithography and subsequent bonding to the LIG layer. This technique depended on cleanroom-based fabrication steps and requires multiple precise steps, including mold preparation, casting, and alignment. This limited the fabrication process in terms of scalability, cost, and accessibility, particularly for rapid prototyping. More examples of LIG-based sensors have been discussed in several review papers, highlighting their development and use in different areas [51] [52]

1.6 Strategies to Improve Electrochemical Performance of LIG

LIG has emerged as a promising material for electrochemical sensors due to its excellent conductivity and surface area. However, surface modification is often required to enhance the electrochemical performance and tailor LIG electrodes towards specific sensing applications. These modifications enhance properties such as wettability, selectivity, sensitivity, and chemical compatibility of the modified electrodes. Different modification techniques have been applied to LIG. Among them, plasma treatment and coating of LIG can be used to address the hydrophobicity issue with LIG electrodes and make them feasible for different sensing application respectively.

1.6.1. Plasma Treatment

LIG's inherent hydrophobicity limits interaction with aqueous electrolytes, hindering electrochemical reactions [53]. Plasma treatment offers a widely used and effective solution to this problem by modifying surface properties without altering the material's bulk structure [54]. Plasma treatment modifies the surface by introducing defects and incorporating functional groups, which alter both the surface morphology and chemical functionality while preserving the bulk structure of the material [55]. This technique effectively introduces surface functional groups based on plasma chemistry, enhancing surface wettability and improving performance of LIG electrodes in electrochemical sensing.

Previous studies applied plasma treatment as a method for enhancing the performance of LIG in various applications. For instance, using a rapid, low-temperature oxygen plasma treatment, a humidity sensor was fabricated by anchoring MoS_2 nanoparticles within nitrogen-doped LIG (MoS_2@NLIG) [56]. Figure 1.5 shows the workflow of this study. This treatment significantly

improved the sensor's performance, resulting in an exceptional sensitivity of 61,219.97 Ω/%RH. The sensor performed effectively across a broad relative humidity (RH) range of 11% to 95% RH.

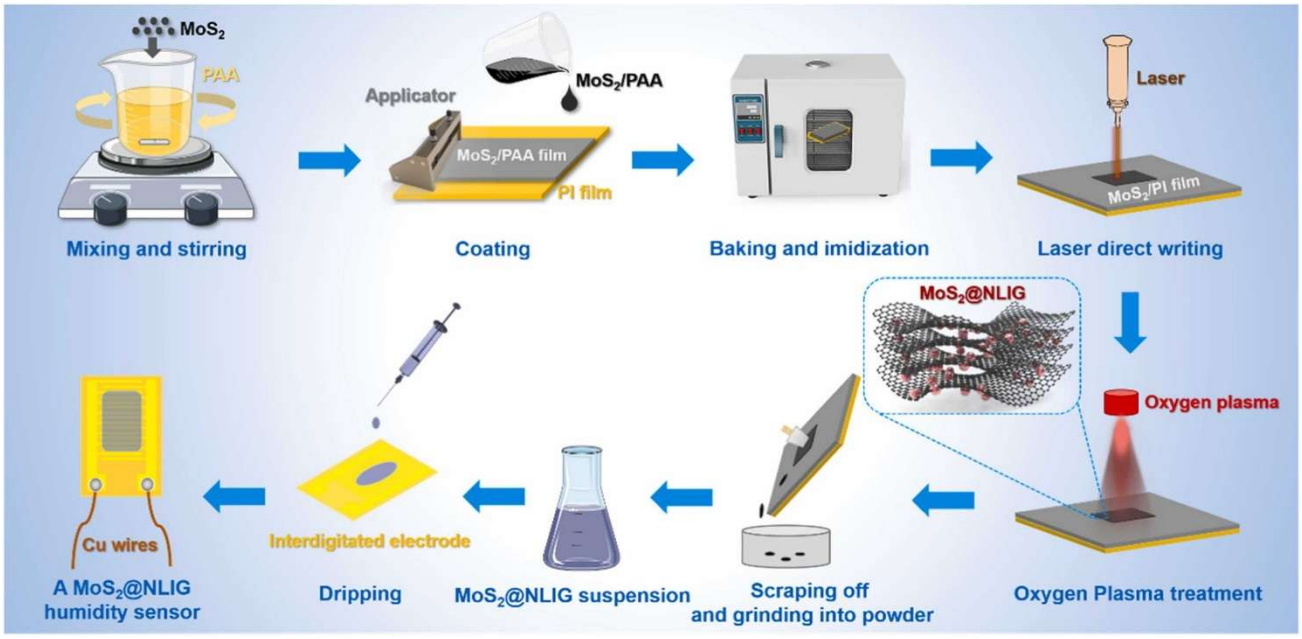

Figure 1.5. Schematic showing the structure and components of a MoS_2@NLIG-based humidity sensor enhanced by oxygen plasma treatment. Reused with permission from Elsevier [40]. License number: 6010430475866[56].

In another study, plasma oxidation was used to modify the surface of LIG, resulting in oxidized LIG with enhanced performance in the oxygen evolution reaction (OER). This treatment improved its catalytic activity, making it more suitable for energy-related electrochemical applications. [57].

Nazeri et al. [58] used plasma-treated LIG electrodes in organic electrochemical transistors (OECTs). The LIG-based devices showed high ON current, low contact resistance, and a strong ON/OFF ratio compared to other electrodes. Biswas et al. [59] showed that plasma treating the PI film before laser scribing helped improve the LIG quality. When they used a lower scan speed

(200 mm/min) and a low laser power (0.77 W), the crystallite size of the LIG increased by 21%, which led to a 51.13% boost in its conductivity compared to the LIG scribbled in untreated PI film.

These studies showed that plasma treatment can help to address the hydrophobic nature of LIG electrodes and improve their sensing performance in different applications. However, all these studies used a steady and short plasma treatment duration in their application, which opens up a question about the impact of different treatment durations on the electrochemical performance of LIG-based electrodes. Plasma can generate defects at the same time along with the improvement of wettability. So, there is a tradeoff between the increasing wettability and defect formation, which needs to be balanced to optimize the overall performance of LIG electrodes.

1.6.2. Coating

Another promising approach to enhance the performance of LIG-based electrochemical sensors is surface coating, which has been explored to improve LIG's sensing performance. LIG coating mainly involves coating a layer of conductive polymer or oxide material onto the graphene surface to enhance its selectivity for specific applications. This modification can make the LIG electrodes more mechanically stable, corrosion-resistant, and selective in electrochemical performance. Only a few studies have explored the benefits of coating LIG surfaces for various applications. This leaves a clear need to investigate other coating materials that could enhance LIG's performance for different uses. One study reported the enhancement of LIG by coating it with a blend of polyacrylic acid and activated carbon. This led to a remarkable improvement in its performance as a supercapacitor electrode [60]. The activated carbon-coated LIG exhibited higher capacitance and better cycling stability compared with traditional graphene-based electrodes and bare LIG

electrodes. Another study by Hashemi et al. demonstrated the feasibility and advantages of LIG coating. This study showed that LIG coated with an alkyd resin formed corrosion-resistant LIG patches. They manually sprayed the alkyd resin onto LIG to create a uniform coating layer. The coated patch showed strong protection against corrosion and good water resistance, making it helpful in protecting metals in flexible electronics and other applications [61]. Tabassum et al. [62], developed an electrochemical biosensor by coating LIG with a graphene-polyaniline (G-PANI) conductive ink. This modification significantly enhanced the sensor's electrical signals, enabling the detection of alpha-fetoprotein and 17β-Estradiol with high sensitivity in phosphate buffer saline and human serum. Meng et al. [63] reported the functionalization of LIG with poly(3,4-ethylenedioxythiophene) (PEDOT) to create a heterostructure three-dimensional transducer for flexible skin patch biosensors. The PEDOT coating improved the structural and contact stability of the LIG network and its electrochemical kinetics. Another study from Ghosh et al [64] presented a novel flexible LIG-based sensor platform modified with graphene-conductive inks such as G-PEDOT:PSS and G-PANI. The LIG/G-PANI sensor demonstrated outstanding performance, achieving a remarkably low limit of detection (LOD) of 0.4084 μM for dopamine and 2.6234 pg/mL for IL-6. The sensor also showed high mechanical durability, which is ideal for wearable bioelectronics. These studies highlighted the benefits of coating LIG, such as improved electrode selectivity and enhanced overall device performance. They also pointed to the potential for tailored coatings in emerging applications like lithium-ion detection.

1.7 Current Strategies for Lithium Detection and the Untapped Role of LIG

The high energy density of lithium-ion batteries has made them the dominant energy storage mechanism in the transportation sector, especially in electric vehicles [8]. As the demand for electric cars and their market share continue to boom, the use of lithium batteries is also increasing at a similar pace. Lithium-based batteries' high-speed charging characteristic is advantageous but drastically reduces cell capacity, significantly increasing battery disposal rates [65]. Improper disposal and inadequate recycling processes lead to lithium leaching into the environment, particularly groundwater sources [66].

While lithium concentration in groundwater has been rising rapidly, a potential health risk is also increasing because of water consumption. Moreover, lithium is commonly used reagent in psychiatric treatments, but its safe dosage range is very narrow. So, if the exposure to lithium in groundwater continues to rise, it can negatively impact neurological health, thyroid function, and kidney performance [67]. Apart from individual health concerns, there is another big issue of lithium accumulation in irrigation water, which can eventually affect soil health and raise food safety concerns [68]. In addition to environmental and health challenges, the need for efficient lithium extraction is becoming increasingly important. Lithium is an essential resource for next-generation energy technologies. Industries are now focusing on developing scalable, low-cost, and rapid detection techniques to identify lithium in complex aqueous systems.

Several studies have described different analytical methods for Li^+ detection. The techniques that have been used include capillary electrophoresis [69], inductively coupled plasma-atomic emission spectroscopy [70], fluorescence-based sensor [71], secondary ion mass spectrometry

[72], and spectrophotometry [73]. However, all the methods mentioned here have a common disadvantage, though they demonstrate promising performance. They involve extensive sample pretreatment and expensive instruments and are unsuitable for developing low-cost, rapid, and easy-to-use sensors that can be produced at scale. Electrochemical sensing offers a strong alternative of detection technique due to its many advantages. These include minimal sample preparation, low-cost electrode fabrication, and the potential for developing portable, user-friendly, point-of-care devices. Electrochemical techniques and voltammetry-based methods such as CV and linear sweep voltammetry (LSV) are straightforward and allow for rapid, cost-effective analysis with relatively simple data interpretation. Additionally, their ability to support in situ measurements makes them ideal for routine monitoring in both environmental and industrial applications. Although effective voltammetry detection of different materials has been reported, there is limited research on voltammetry for lithium detection. For instance, Suherman et al. [7] reported the detection and quantification of lithium-ion in authentic human saliva using CV and LSV using lithium manganese oxide (LMO) and modified SPE. However, the modification method of this research required multiple sample preparation steps, which resulted in a complex and time-consuming process. Vitale et al. [74] developed a smart sensor for lithium detection using CV. Their design involved a multi-step modification of graphite-based SPEs, starting with enhancing the electrode surface using gold and silver nanoparticles to boost conductivity. This was followed by depositing an ion-selective membrane directly onto the nanostructured surface. However, the modification of SPEs involved multiple complex steps, which could pose scalability and cost-effective production challenges. Criscuolo et al. [75] employed platinum and gold SPEs

modified with noble metal nanostructures through electrodeposition for lithium detection. While the resulting sensor demonstrated Nernstian behavior, rapid response time, excellent potential stability, expensive materials, and a complex fabrication process make it impractical for large-scale or routine applications.

LIG offers a cost-effective and straightforward fabrication process, making it a promising candidate for lithium-ion detection. To the best of our knowledge, no reported studies have used LIG for this purpose. In contrast to previous approaches that rely on complex and expensive electrode modifications, LIG can be easily functionalized, allowing for more straightforward sensor development. This presents an opportunity to explore LIG as a low-cost and scalable option for lithium sensing, potentially addressing key limitations in current methods.

1.8 Three-Dimensional Printing for LIG Substrate Fabrication and Integrated Sensing Architecture

3D printing is an additive manufacturing technology that creates physical parts by stacking material layers rather than subtracting material or using molds. This method offers benefits like lower setup costs, faster prototyping, and the ability to create complex designs using different types of materials. Initially, 3D printing was used mainly for rapid prototyping, allowing engineers to test and refine product designs quickly. However, it has evolved into a robust manufacturing method capable of producing functional end-use parts. Recently, 3D printing has been widely used across industries, not only for prototyping but also for making customized tools, components, and lightweight structures.

There are several types of 3D printing techniques such as fused deposition modeling (FDM), stereolithography (SLA), digital light processing (DLP), selective laser sintering (SLS), selective laser melting (SLM), direct metal laser sintering (DMLS), binder jetting, material jetting (MJ), electron beam melting (EBM), and laminated object manufacturing (LOM). Among the different 3D printing techniques, we focus on FDM because it allows using high-temperature thermoplastics such as PEI, which are well-suited for LIG scribing. Although other printing methods have their associated advantages, FDM stands out for its material compatibility, low cost, and ease of use, making it an ideal choice for fabricating substrates that can be effectively carbonized [76]. Another notable advantage of FDM printing is its capability to support multiple tool heads, enabling different fabrication processes to be carried out within a single setup. This includes printing the substrate using high-temperature thermoplastics, laser-scribing to form LIG, and applying functional layers through dispense printing. Integrating these steps without reconfiguration makes the workflow more efficient, precise, and suitable for producing complex, multilayered sensing platforms.

Figure 1.6 illustrates the steps involved in FDM 3D printing. The process begins with creating a 3D model using software such as AutoCAD or SolidWorks. The model is then sliced using slicing software to prepare it for printing, converting it into a gcode file. The extruder nozzle and bed temperatures are adjusted based on the filament type used. Finally, the printing process is carried out through computer-controlled software, such as repetrel, producing the final printed design.

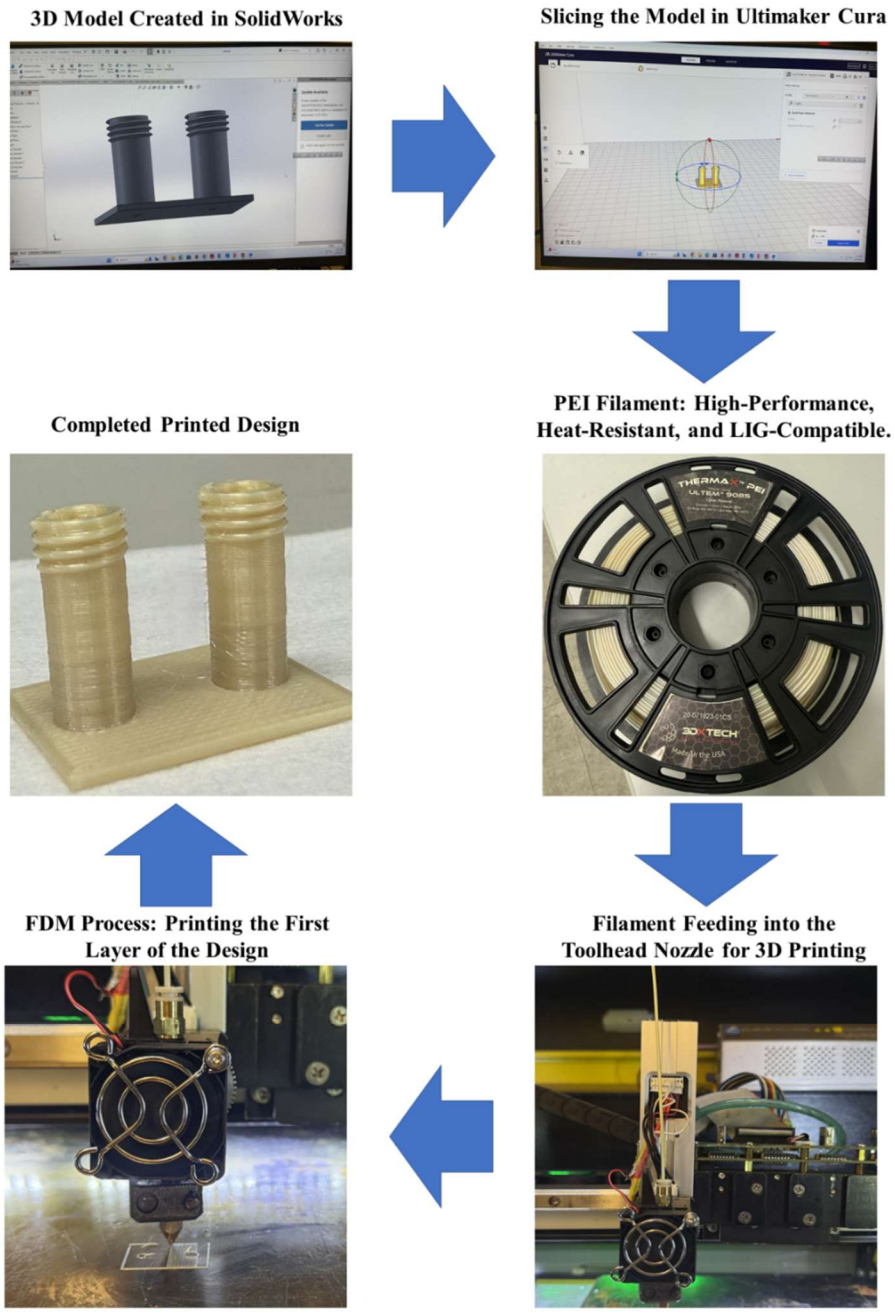

Figure 1.6. Step-by-step process of FDM printing, from 3D model creation in SolidWorks to the final printed object.

Integrating electronics with 3D printing significantly broadens potential applications, particularly in sensors and flexible electronics [77]. In the case of LIG, conductive graphene structures can be directly formed on 3D-printed substrates made from carbon-rich materials such as PEI, polyether ether ketone (PEEK), and PSU through controlled laser scribing. These polymers are suitable for carbonization, making them ideal for LIG fabrication. Figure 1.7 shows the process of fabricating LIG-based electrodes on a 3D-printed substrate as pursued in this thesis.

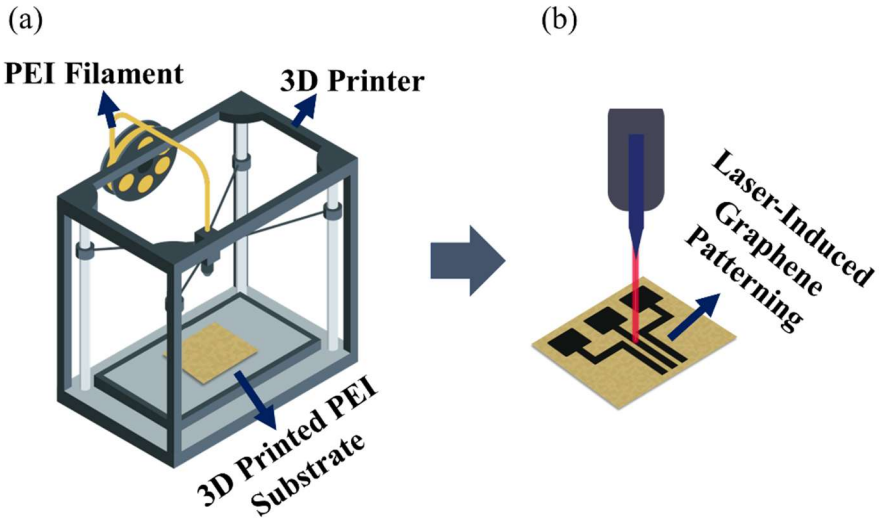

Figure 1.7. Schematic representation of the fabrication process for LIG-based electrodes on a 3D-printed substrate that was pursued in this thesis. (a) A 3D printer is used to fabricate a PEI substrate using PEI filament. (b) LIG patterning is performed.

Previous studies demonstrated the feasibility of LIG formation on carbon-based substrates. For example, Tavakkoli Gilavan et al. [78] in their research successfully fabricated LIG on 3D-printed PEI using a CO_2 laser, achieving the lowest reported sheet resistance (0.30 Ω/sq) by optimizing laser power and pattern. Wu et al. [79] demonstrated another fabrication example of LIG on a 3D-printed substrate. In their study, they formed a thin LIG layer (~50 μm) that served as an active

material for sensor applications. The resulting PEEK–LIG smart components exhibited real-time self-monitoring capabilities, detecting bidirectional bending and stretching with high sensitivity. Vandervelde et al. [80] demonstrated the successful fabrication of LIG using a blue laser on pure and 3D-printed PEI and PEEK substrates. The resulting LIG revealed some of the lowest sheet resistances reported for these materials, highlighting its excellent electrical performance. Their study further showcased the potential of LIG-based devices, with heaters demonstrating broad operating ranges and strong electrothermal response. At the same time, LIG strain gauges delivered high gauge factors with minimal signal drift.

The studies discussed here highlight the successful fabrication of LIG on 3D-printed substrates, showing strong potential for combining additive manufacturing with LIG-based technologies. This approach opens new directions for advancing the field. With the help of modification and functionalization, the properties of LIG can be tailored to improve its selectivity and sensitivity for targeted sensing applications. Furthermore, embedding LIG within 3D-printed structures, specifically electrochemical platforms, especially when using the same 3D printed polymer for the substrate, LIG patterning, and microfluidic layer, offers a unified strategy to improve device performance by ensuring better analyte control and detection reliability. Adding a microfluidics platform to the electrochemical sensor can significantly improve how fluids are handled, reduce the need for complex sample preparation, and boost sensor performance. Features like microfluidic channels or chambers can make the system more efficient and reliable. The following section explains the role of microfluidics and the opportunity it presents when added to the electrochemical sensor.

1.9 Microfluidic Electrochemical Sensors

Microfluidics involves the precise control and manipulation of fluids at the microscale, using the principles of fluid mechanics and microfabrication to create systems, typically with channel dimensions ranging from tens to hundreds of micrometers [81]. Microfluidic devices are increasingly used in biological, chemical, and environmental sensing because they allow precise control of fluids, require minimal sample volumes, and enable rapid, high-throughput analysis. [82]. These platforms can integrate multiple processes, including sample preparation, mixing, and detection, on a single chip, enabling highly efficient and compact sensor systems. With the growing need for accurate on-site testing, microfluidic technology is progressively leading the field of portable analysis [83].

Microfluidic system fabrication usually involves multiple steps, including chip design, material selection, fabrication, and packaging. These steps often come with technical challenges in traditional methods like PDMS-based fabrication [84]. Numerous techniques have been used for the fabrication of microfluidics, such as photolithography [85], soft lithography [86], polymer molding such as hot embossing and injection molding [87], and laser ablation [88]. These methods allow the creation of precise microchannels and chambers on a substrate. However, a common challenge across all of them is the sealing of these open structures to form fully enclosed and functional microfluidic channels. Enclosing the microstructure can be challenging because adding an extra layer takes time and may lead to defects in the final stage. As a result, research is still needed to address the above-mentioned issues in this field.

To overcome these challenges, newer materials such as thermoplastics and fabrication techniques like 3D printing and injection molding have been introduced, offering more scalable, cost-effective, and portable alternatives [89]. Building on these advancements, a promising approach involves integrating 3D-printed microfluidics and substrates using the same thermoplastic material, allowing for the incorporation of LIG electrodes to create a fully additively manufactured chip suitable for sensing applications. 3D printing offers promising solutions by enabling the fabrication of complex structures through a single, streamlined process without the need for frequent adjustments to the fabrication setup [90]. Several studies have demonstrated the practicality of using 3D printing to fabricate microfluidic devices, aiming to overcome limitations commonly associated with traditional PDMS-based techniques. For instance, Costa et al. [91] demonstrated a reusable electrochemical microfluidic device fabricated via SLA-based 3D printing, integrating electrodes directly into the microchannel structure. Figure 1.8 shows the schematic workflow of their work. A composite of graphite/resin (C/resin) was embedded into a side-wall microchannel to form a working electrode. Electrochemical characterization using square wave voltammetry with ferrocene methanol showed excellent linearity ($R^2 = 0.995$) and low detection limits (LOD: 4.5 μM; LOQ: 15 μM). The system also performed reliably under flow conditions, highlighting its potential for integration into miniaturized analytical platforms.

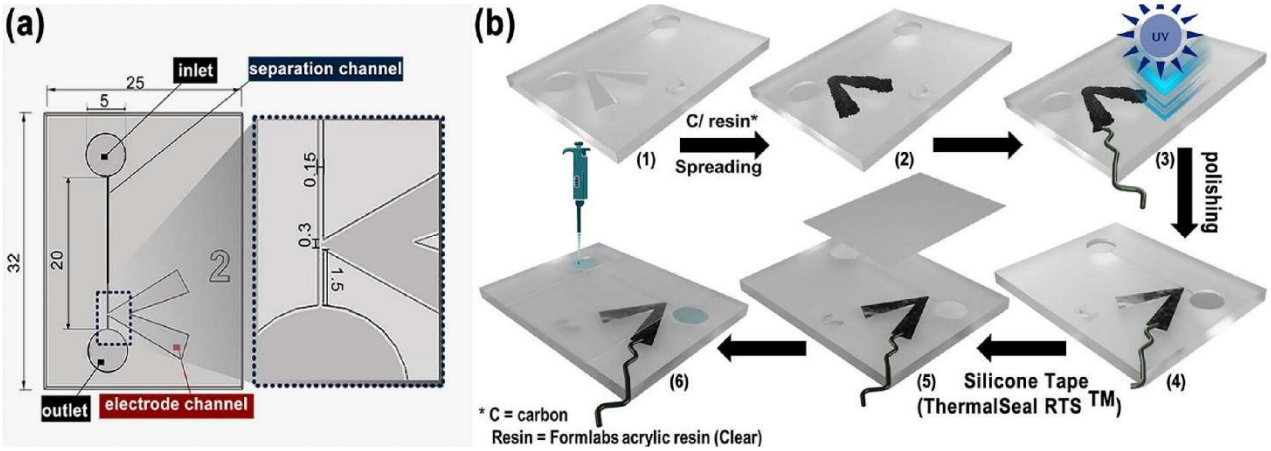

Figure 1.8. (a) Design sketch of the microfluidic device created using Fusion 360, with an inset illustrating the connection between the electrode channel and the separation channel, as well as the distance from the outlet reservoir to the electrode channel(b) Schematic of the assembly process for the fully integrated electrochemical microfluidic device. Reproduced with permission. License number: 6027760114389.

A review article from Su et al. [92] highlighted how 3D printing has become an important method for making microfluidic devices. It allows for fast design changes, easy prototyping, and the use of different materials on a single platform. These features are helpful in many fields, including biology, chemistry, medicine, and soft robotics. They discussed recent progress, such as printing on 3D surfaces, using flexible materials like thermosetting elastomers, and improving printing resolution and automation. Another review by Ho et al. [93] described how 3D printing is helping to advance the field of microfluidics, especially in biomedical applications. These studies show how 3D printing has improved the way microfluidic systems are made, making the process easier, faster, and more flexible.

In recent years, there have been notable advancements in the field of manufacturing electrochemical sensors as well as microfluidic devices. Developments in both fields have pursued

to focus research on integrating microfluidics with electrochemical sensors. By merging both technologies, it becomes possible to create versatile, compact devices capable of incorporating various electrode systems and microstructures on various materials, unlocking new opportunities for diverse applications. Figure 1.9 shows a layout that integrates microfluidics devices with electrode systems, forming a microfluidic device-based electrochemical sensor.

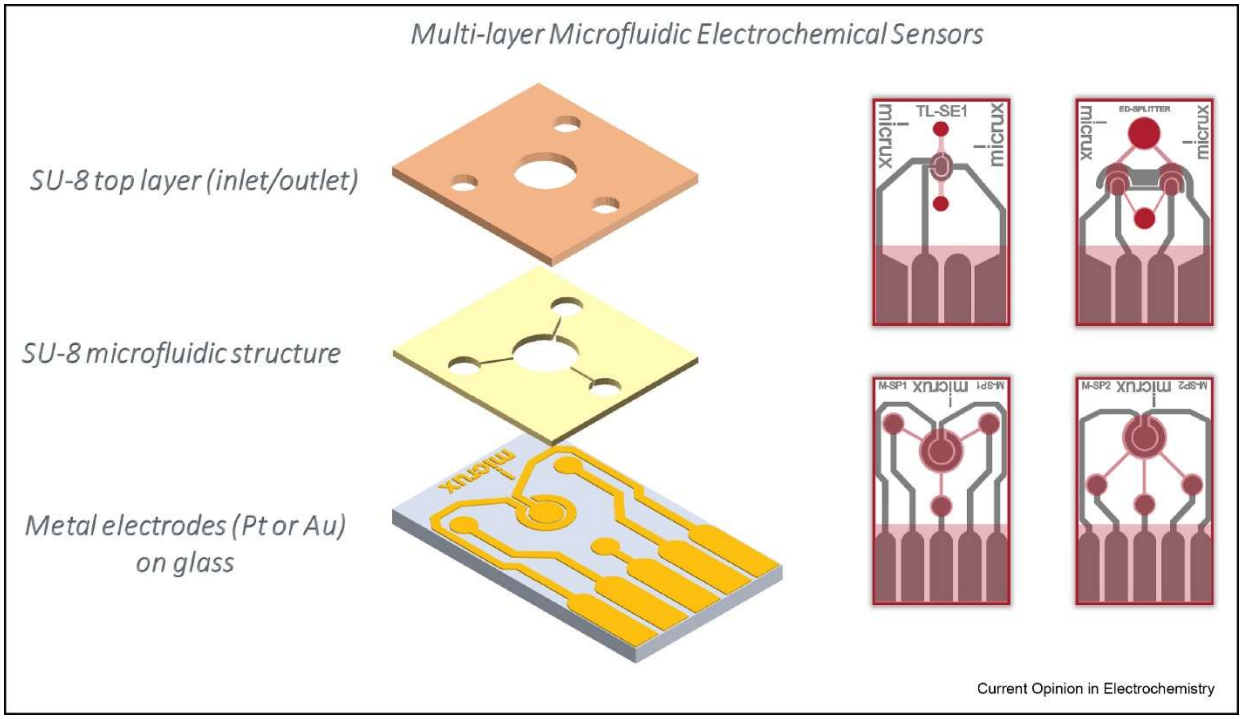

Figure 1.9. Schematic layout showing the integration of microfluidic channels with electrode systems to form a microfluidic-based electrochemical sensor. This configuration highlights the potential for compact, efficient, and real-time sensing application [9]. Figure reused with permission from Elsevier. License number: 6010991340027.

Several studies have explored the integration of microfluidic systems with electrochemical sensing technologies using a variety of electrode materials, including LIG-based electrodes. This combination takes advantage of microfluidics for controlling small amounts of liquid and uses

advanced electrodes to improve detection and overall sensor performance. For example, Ma et al.[94] developed a portable microfluidic electrochemical sensing system for detecting heavy metal ions, using lead ions (Pb^{2+}) as a proof-of-concept target. Differential pulse voltammetry was employed for the detection. As the WE, the device integrated a specially prepared nanocomposite Ag-rGO-f-$Ni(OH)_2$/NF. This nanocomposite consisted of silver nanoparticles (Ag) and functionalized nickel hydroxide [$Ni(OH)_2$] grown on reduced graphene oxide (rGO), all supported on a porous nickel foam (NF) substrate. The microfluidic channel was fabricated using soft lithography techniques with PDMS casting. To ensure stable operation, the connection points and exposed silver wire were encapsulated with cured PDMS to prevent contact with the electrolyte. The system successfully demonstrated a low LOD for detecting Pb^{2+} in river water, achieving 0.00498 μg/L. Shen et al. [95] presented a modifier free microfluidic electrochemical sensor for Cd^{+2} and Pb^{+2} detection using square-wave anodic stripping voltammetry. This work integrated a microfluidic paper-based channel with a miniaturized carbon-based electrochemical sensor. The sensor utilized pristine graphite foils for the WE, RE and CE. LIG has also shown great promise when integrated with a microfluidic channel. For example, Griesche et al.[96] demonstrated the successful integration of microfluidics with LIG-based electrochemical sensors by transferring LIG electrodes from PI films onto polymer substrates. Two microfluidic fabrication strategies were employed: indirect adhesive tape bonding and solvent bonding with PMMA. While the transferred LIG maintained comparable electrochemical performance, a reduction in active surface area was observed, along with the loss of the characteristic Raman 2D peak and a slight decrease in electron transfer efficiency. Johnson et al. [97] developed an electrochemical biosensor integrating LIG and

microfluidics for on-site biomedical and environmental monitoring. Key improvements in their design included Y-shaped reservoirs for stable fluid flow, PEI coatings to preserve surface wettability and modular components that allowed easier electrode biofunctionalization. Chen et al. [98] developed an LIG-based open microfluidic system for environmental biosensing and energy storage devices. The LIG was patterned on PI film, and the fabrication techniques were implemented to create an all-LIG open microfluidic cross pattern capable of dividing a single fluid sample into four branches to four distinct, independently electrically addressable LIG biosensors. The open microfluidic system was created by laser patterning a polyimide surface to form super hydrophilic tracks that guide fluid flow. A second laser pass was applied to modify the edges of these tracks to become superhydrophobic, which helped confine the fluid and enhance sensor performance. The electrodes were then functionalized with ion-selective membranes for K^+, NO_3^-, and NH_4^+.

Integrating microfluidics with electrochemical sensors has shown great potential but still faces challenges. Issues such as microchannel deformation, electrode damage during assembly, and poor system interconnection can affect performance. Techniques like 3D printing and LIG can offer promising solutions by enabling simultaneous fabrication of microfluidics and electrodes, improving integration and overall device functionality.

1.10 Research Gaps

Despite numerous studies implementing LIG-based electrodes as electrochemical sensing platforms, several challenges remain under research for advancing LIG-based electrochemical

sensors. In our work, we address three specific research gaps identified through a detailed review of the existing literature.

1. While previous studies demonstrated the benefits of plasma treatment in enhancing the properties of LIG, they did not study the effect of plasma on LIG in detail, and they have primarily focused on short treatment durations. As a result, the effect of extended plasma exposure on LIG's structural and electrochemical properties remains unexplored. Since longer treatment durations could enhance performance by further improving surface wettability, a detailed investigation is necessary to assess these effects thoroughly. This gap is addressed in chapter 2 of the thesis.
2. The rising demand for lithium-ion batteries, especially in electric vehicles, has increased the need for simple, low-cost, and effective lithium-ion sensors. With its excellent conductivity, large surface area, and ease of fabrication, LIG shows strong potential for this purpose. However, to date, no research has reported using LIG for fabricating lithium-ion sensors, indicating a potential gap and an opportunity for further investigation. Exploring modified LIG electrodes for this application could lead to developing practical, easy-to-fabricate sensors suited for real-world use. Modifying LIG-based working electrodes using dispense printing can be used to create a simple fabrication process for lithium sensors which is shown in chapter 3.
3. Existing research shows that integrating a microfluidic platform with electrode materials, including LIG, typically involves multiple fabrication steps. Each step requires precise control to ensure the final device is defect-free and all the layers are correctly aligned to

prevent the sensing efficiency from being hampered. By scribing LIG onto the base layer of a 3D-printed microfluidic system and printing the microfluidic channel directly on top using the same material and printing parameters, seamless integration between the electrode and the microfluidic system is achieved. This approach simplifies the fabrication process while enhancing the efficiency of the electrochemical sensors which is described in chapter 4.

1.11 Thesis Organization

This thesis presents a detailed study of LIG-based electrodes for electrochemical sensing and addresses the challenges discussed in the previous section. The research starts by optimizing plasma treatment on LIG electrodes to improve electrochemical performance while minimizing the adverse effects of plasma overexposure. Then, we modified LIG electrodes using LMO. The LMO functionalization of LIG electrodes demonstrated strong electrochemical performance, showing enhanced selective detection of lithium ions over interfering ions such as K^+ and Na^+. Finally, the integration of 3D printing with LIG fabrication is explored, enabling the creation of microfluidics-based electrochemical sensors. This insitu fabrication process offers a promising solution for developing effective electrochemical sensors for Li-ion detection.

Chapter 2 presents a comprehensive study on the impact of plasma treatment on the physical properties and electrochemical performance of LIG electrodes. This investigation involves both physical and electrochemical characterization of LIG after plasma processing, with varying treatment times to identify an optimal window for enhanced performance.

Chapter 3 provides a discussion on the modification of LIG electrodes using dispense printing of LMO. In this chapter, we optimize the dispense printing parameters and curing temperature for LMO deposition. Electrochemical tests are then conducted using LiCl in the presence of other salts to assess the selectivity of the LMO-LIG electrodes for Li^+ ion detection.

In Chapter 4, we present the development of a novel 3D-printed microfluidic electrochemical sensor featuring LIG-based three-electrode systems. The microfluidic channel was directly integrated onto the LIG electrodes using a laser-scribing process on 3D-printed PEI. Furthermore, LMO modification was applied to the LIG electrodes to enhance their capability for Li^+ detection.

In chapter 5, the main results of this study are summarized, and suggestions for future work are presented.

1.12 Research Contributions and Dissemination

1. Conference abstract (accepted)

S. D. Shovan, C. R. Perales, S. Jafargholinejad, M. K. Idris, P. Rezai, and G. Grau, "Laser-Induced Graphene Electrodes for Electrochemical Sensors with Enhanced Performance via Plasma Treatment," presented at the 247th ECS Meeting (May 18-22, 2025), ECS, May 2025. Available: https://ecs.confex.com/ecs/247/meetingapp.cgi/Paper/202014

2. Journal paper (Submitted)

Shovan, S. D., Jafargholinejad, S., Idris, M. K., Perales, C. R., Minhas-Khan, A., Rezai, P., Grau, G. "Electrochemical Sensing Performance Enhancement of Laser-Induced Graphene-Based Electrodes via Surface Oxygen Plasma Treatment".

3. Conference abstract (submitted)

S. D. Shovan, M. K. Idris, S. Jafargholinejad, P. Rezai, and G. Grau, “3D-Printed Microfluidic Electrochemical Sensor with Laser-Induced Graphene Electrodes and Printed Functionalization for Lithium Sensing,” abstract submitted to the 248th ECS Meeting, ECS.

4. Journal paper (under preparation)

Shovan, S. D., Idris, M. K., Jafargholinejad, S., Rezai, P., Grau, G. "3D-Printed Microfluidic Electrochemical Sensor with Laser-Induced Graphene Electrodes and Printed Functionalization for Lithium Sensing.

2 Effect of Plasma Treatment Duration on LIG Electrodes

2.1 Introduction

LIG has emerged as a promising alternative to traditional carbon-based electrode materials for electrochemical sensing applications. Despite their promising performance, LIG materials in these sensors face a critical challenge, i.e., their inherent hydrophobicity limits interaction with aqueous electrolytes, hindering electrochemical reactions [53]. Plasma treatment offers a widely used and effective solution to this problem by modifying surface properties without altering the material's bulk structure [54]. When a particular electrode surface is exposed to a plasma environment, reactive species attach to the material surface, promoting electrochemical reactions through chemically active polar oxygen functional groups such as C-O, C=O, and -CHO [99].

Previous studies used plasma to improve the performance of LIG with a short treatment duration. As a result, the effect of varying plasma exposure times on the electrochemical performance of LIG remains unclear and underexplored. Since longer treatment durations might enhance performance by further improving surface wettability, a detailed investigation is necessary to assess these effects thoroughly. This research addresses this gap by examining the effects of varying plasma treatment durations on the material characteristics and electrochemical performance of LIG-based sensors. By doing so, we established an optimal treatment window that enhances electrochemical performance while preventing overexposure that degrades material integrity.

2.2 Materials and Methods

2.2.1 Materials, Chemical Reagents and Sample Preparation

Potassium Ferricyanide $K_3[Fe\ (CN)_6]$; Potassium hexa-cyanoferrate (II) trihydrate $K_4Fe\ (CN)_6 \cdot 3H_2O$, and Potassium Chloride (KCl) were purchased from Sigma-Aldrich (Ontario, Canada) for making the analyte solution. PI film (Kapton tape) was purchased from Creative Global Services Limited (Ontario, Canada) as a substrate for formulating LIG.

In this study, we performed electrochemical characterization of the standard potassium ferrocyanide/potassium ferricyanide redox system using a fully integrated LIG based electrochemical sensor. Potassium ferricyanide $K_3[Fe(CN)_6]$ and potassium ferrocyanide $K_4[Fe(CN)_6]$ are widely used in physiological experiments for their role in modulating cellular redox reactions [100] [101]. $[Fe\ (CN)_6]^{4-/3-}$ was chosen from a variety of popular redox systems for its surface-sensitive electrochemical response, making it particularly suitable for the study of carbon-based materials [102], [103], [104], [105] . The analyte solution was prepared in DI water and mixed thoroughly using a vortex mixer. A 100 mM stock solution was initially prepared, and subsequent concentrations were obtained through serial dilution.

2.2.2 Electrode Fabrication and Plasma Treatment of the Fabricated Device

A LIG- based three-electrode system was designed using manual coding and converted into gcode for use in the Repetrel software of the Hydra 16 A printer (Hyrel, Georgia, USA) with a 40 W CO_2 laser. Graphene was fabricated by scribing a piece of Kapton tape of 125 μm thickness attached to a glass slide (Figure 2.1a (i, ii)). To identify the optimal laser settings for minimizing sheet

resistance, the laser power was studied and adjusted from 18 % to 28 % of its maximum 40 W output in 2 % increments, while the scan speed spanned from 60 to 360 mm/min with a step size of 60 mm/min.

After the fabrication of the three-electrode LIG system, the device underwent air plasma treatment using a MARCH PLASMOD plasma system (MARCH, California, USA), in conjunction with a T&C power converter (Figure 2.1a (iii)). The plasma treatment was conducted at a power level of 25 W, with treatment durations ranging from 10 to 60 seconds in 10-second increments, as well as an extended interval of 120 seconds.

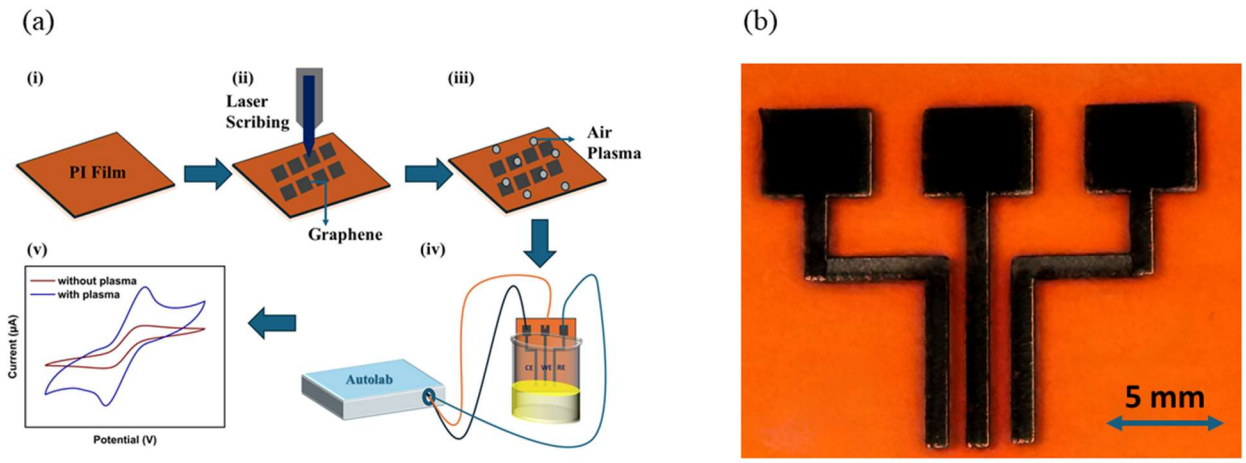

Figure 2.1. Schematic of the fabrication process (a) Fabrication steps, (i) Preparation of the PI film substrate, (ii) Laser scribing for LIG formation, (iii) Air plasma treatment of LIG electrodes to enhance surface properties, (iv) Electrochemical testing setup for performance evaluation, (v) Improved electrochemical performance observed through CV and EIS, (b) Optical micrograph of fabricated LIG three electrode system.

2.2.3 Electrochemical Characterization and Data Analysis

CV measurements were performed using the fabricated three-electrode system immersed in 20 mL of analyte solution in a beaker as shown in Figure 2.1a (iv). The experiments were conducted at room temperature with an Autolab potentiostat (Utrechat, Netherlands) controlled by Nova 2.1 software. The potential was swept from -0.8 V to 0.8 V at a scan rate of 100 mV/s. This potential window was selected to accurately capture the peak potential across different treatment times and analyte concentrations. While previous studies have typically used a narrower range of -0.3 V to 0.5 V for potassium ferrocyanide/ferricyanide analyte solutions [106], our extended range ensures precise detection of any subtle potential variations induced by treatment changes. Each experiment consisted of three consecutive scans, and the average was used for analysis. The anodic and cathodic peak currents for all the CV scans were determined by identifying the maximum (anodic) and minimum (cathodic) currents, where the peaks were observed in the scan plots, ensuring consistency. The difference between anodic and cathodic peak currents was calculated to determine ΔI_p. The LOD was determined based on the standard deviation of measurements from the blank solution and low-concentration samples. For lower analyte concentrations, where no detectable peaks were observed (precisely, 0.04 mM–0.5 mM for untreated devices and 0.04 mM–0.06 mM for plasma-treated devices), the ΔI_p was measured as the difference between the highest and lowest currents within the -0.5 V to 0.5 V range. This voltage range was chosen as it encompasses the redox peaks observed at higher concentrations, making it the relevant faradaic region for electrochemical analysis. Additionally, a blank solution of 0.1 M KCl, without the analyte, was analyzed within the same voltage range for both untreated and plasma-treated devices

to ensure a consistent comparison. A detailed description of the method to calculate LOD, limit of quantification (LOQ), and sensitivity from these results is given in the next section.

EIS measurements were carried out using an Autolab potentiostat over a frequency range from 0.1 Hz to 10 kHz, with a potential perturbation amplitude of 1 mV versus the open-circuit potential (OCP). These measurement settings were selected based on literature reference [106], as they provided accurate results with a well-fitted equivalent circuit model, eliminating the need for further adjustments. All experiments were conducted at room temperature to ensure consistency across measurements. Three devices were tested for each plasma treatment condition, and the averaged results were used to generate the Nyquist plot. To determine the EIS parameters—including solution resistance (R_s), charge transfer resistance (R_{ct}), electric double-layer capacitance (C_{dl}), and the Warburg element (W_e)—an equivalent circuit model was fitted to the data from all three devices. The measured values were then averaged, and error bars were calculated based on the standard deviation of these three datasets to represent variations in EIS parameters.

Statistical analysis was performed to evaluate the significance of changes in EIS parameters and LOD across different conditions. A t-test was conducted to assess whether the observed variations were statistically significant. For each condition, three measurements were taken, and the p-values from the t-test were calculated to quantify the significance of differences between datasets.

2.2.4 Determination of LOD, LOQ and Sensitivity

The determination of the LOD follows a structured methodology [107] that begins with the establishment of the limit of blank (LOB). This process starts by performing five independent measurements of a blank sample, specifically 0.1M KCl, under identical experimental conditions. The mean response, denoted as $(\text{mean})_{\text{blank}}$, is obtained by averaging the recorded current values within the Faradaic voltage range of -0.5V to 0.5V. The standard deviation of these 5 measurements is calculated and denoted by $(\text{SD})_{\text{blank}}$. Following this, LOB was calculated for both treated and untreated conditions using equation (1).

$$\text{Limit of Blank (LOB)} = (\text{mean})_{\text{bla}} \quad + \ 1.645\ (\text{SD})_{blank} \tag{1}$$

After determining the LOB, the LOD is calculated using equation (2).

$$\text{LOD}_{\text{current}} = \text{LOB} \ + \ 1.645\ (\text{SD})_{\text{low concentration sample}} \tag{2}$$

To calculate $(\text{SD})_{\text{low concentration sample}}$ we selected a sample containing a small amount of analyte just above the blank level. Five independent measurements were taken for both the untreated and 50 s treated devices. The standard deviation of these measurements was then used to determine $(\text{SD})_{\text{low concentration sample}}$, which was incorporated into the LOD calculation.

Initially, the LOD is expressed in terms of current (μA), providing a threshold to distinguish detectable signals from background noise. To make this value more practical and comparable, it is then converted to analyte concentration using the measured dose-response plot of peak current vs concentration (Figure 2.5 (a, b)) and equation (3).

$$\mathrm{LOD_{conc.}} = \frac{\mathrm{LOD_{current}} - \text{Y intercept of the plot (Sensor Response vs Analyte Concentration)}}{Sensitivity\ (Slope\ of\ the\ linear\ region\ of\ the\ plot)} \ldots\ldots\ldots (3)$$

To determine the slope and y-intercept of the calibration plot, the linear region of the data presented in Figure 2.4e was first identified. This was achieved by analyzing the range of analyte concentrations with the strongest linear correlation.

LOQ represents the lowest concentration of an analyte that can be reliably quantified with acceptable precision and accuracy. It is typically determined based on the response's SD at low analyte concentrations. LOQ can be estimated using a signal-to-noise (S/N) ratio of 10:1, and is commonly calculated using the following formula:

$$LOQ = \frac{10\ SD_{low\ concentration\ sample}}{Sensitivity\ (Slope\ of\ the\ linear\ region\ of\ the\ plot)} \quad (4)$$

Sensitivity refers to how much the output signal (e.g., voltage, current) changes per unit concentration of the analyte. Sensitivity is typically represented by the slope of the calibration curve in the linear dynamic range. In this study, sensitivity was determined by calculating the slope of the linear region of the dose–response curve that exhibited the highest R^2 value. These approaches described in this section were consistently used for determining the LOD, LOQ, and sensitivity throughout the subsequent chapters.

2.2.5 Material Characterization

Contact angle measurement: Contact angle measurements were performed using the Krüss FM 40 Easy Drop Contact Angle Measuring System (KRÜSS Scientific, Hamburg, Germany) and Drop Shape Analyzer software. A droplet was dispensed onto the substrate using a syringe pump

at a controlled flow rate of 500 μL/min. Images were captured once the droplet stabilized on the surface, ensuring accurate measurements. The acquired images were further processed and analyzed using ImageJ software. To account for surface variability, five measurements were taken at different locations on the LIG surface. The error bars were calculated based on the variation among these five readings.

Sheet resistance measurement: The sheet resistance of the inscribed LIG was measured using a four-point probe system (Ossila, Sheffield, UK). For each measurement, 5 × 5 mm square samples were prepared. To ensure accuracy, five measurements were taken from each of the five samples for every laser power and speed setting. The calculated error bars, based on measurement variations, were incorporated into the figures.

SEM analysis: The morphological and structural characterization of the LIG samples was performed using a TESCAN VEGA3 scanning electron microscope (TESCAN, Brno, Czech Republic). High-resolution images were captured to evaluate the quality and surface features of the fabricated LIG.

Raman spectroscopy Raman spectra were recorded using a LabRAM ARAMIS Raman Microscope (HORIBA Scientific, Piscataway, USA) with a 532 nm laser excitation and a laser power of 50 mW. The I_D/I_G ratio was determined using Origin software by performing Gaussian peak fitting on the D (~1350 cm^{-1}) and G (~1580 cm^{-1}) peaks after baseline correction. The integrated areas under these fitted peaks were then used to calculate the ratio, with the D-band area divided by the G-band area.

X-ray photoelectron spectroscopy (XPS): XPS analysis of the samples was performed using the K-Alpha XPS system (Thermo Fisher Scientific, Massachusetts, USA). Peak fitting of XPS spectra was performed in Origin software using a Gaussian function after baseline correction. The peaks were deconvoluted within the defined binding energy ranges corresponding to specific elements or functional groups. Fitting parameters were optimized to minimize residual error and ensure accuracy.

2.3. Results

2.3.1 Laser Operation Parameter Optimization for LIG Synthesis

The engraving of graphitic carbon on PI tape was conducted by evaluating the impact of two key laser parameters: laser power percentage and laser scan speed. These parameters were tested to determine their effectiveness in inducing graphitic carbon on the PI substrates while achieving the lowest possible sheet resistance. Sheet resistance is a crucial parameter for understanding and quantifying the electrical conductivity of thin films and two-dimensional materials like LIG [24]. Lower sheet resistance allows more current to pass through the material, making it an essential feature for applications like electrodes or interconnects [25]. Figure 2.2 illustrates the variation of sheet resistance in relation to both laser power and scan speed.

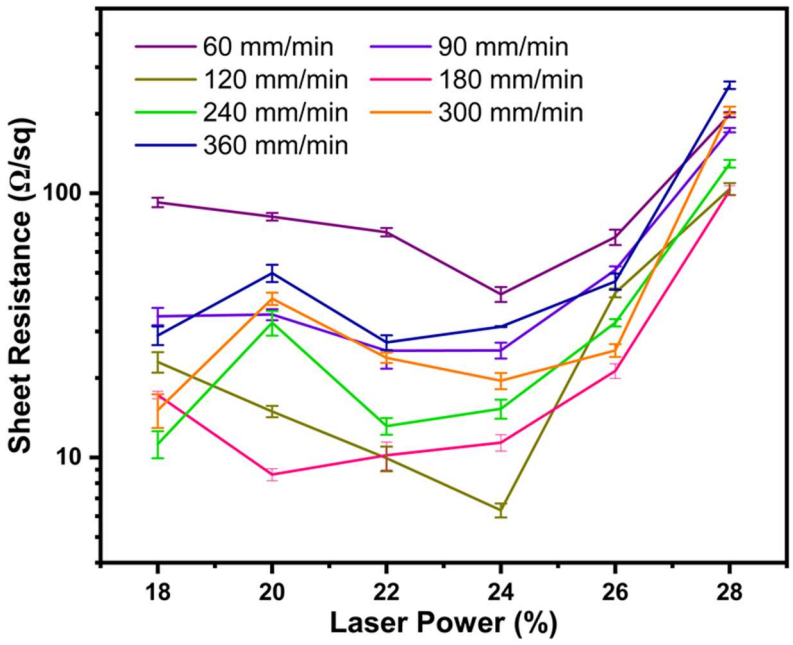

Figure 2.2. Optimizing the laser settings by examining the variation of sheet resistance as a function of laser power at different scan speeds (legend) during LIG formation on PI tape.

The data reveals that as the laser power increases, the sheet resistance decreases across all scan speeds. This occurs because the higher laser power delivers more energy to the PI tape, facilitating the formation of more conductive graphitic carbon [26]. However, when the laser power exceeds a certain threshold, an increase in sheet resistance is observed across all scan speeds, likely due to damage or over-carbonization of the LIG structure. This increase is attributed to the excessive energy input, which creates brittle electrodes prone to peeling off the substrate, leading to higher resistance in the graphitic carbon. [5]. At lower power settings (18%-22%) and higher scan speeds (240-360 mm/min), the PI substrate did not undergo proper or complete carbonization, resulting in LIG with higher sheet resistance. When examining the effect of laser scan speed, it becomes evident that extremely low speeds lead to significantly higher sheet resistance across all power

levels. However, as the scan speed increases, the sheet resistance of the fabricated LIG decreases. For example, at a fixed laser power of 24%, the sheet resistance was initially 41.46 ± 2.69 Ω/sq at a scan speed of 60 mm/min. This value decreased progressively, reaching a minimum of 6.31 ± 0.39 Ω/sq at 120 mm/min before rising again to 31.27 ± 0.15 Ω/sq at 360 mm/min. This variation in sheet resistance can be attributed to the effects of scan speed on carbonization. The extended exposure time can lead to over-carbonization at very low scan speeds, resulting in higher sheet resistance. The sheet resistance typically decreases as the scan speed increases, indicating a more conductive graphitic structure. However, sheet resistance rises again beyond an optimal speed due to insufficient energy exposure, leading to incomplete carbonization.

2.3.2 Effect of Plasma Treatment Time on CV of LIG Based Sensors

To assess the impact of plasma treatment with different exposure times on the sensor's performance of a three-electrode LIG system, both untreated and plasma-treated samples were analyzed using CV at room temperature. For Faradaic testing, a redox probe solution of 5 mM ferricyanide/ferrocyanide was used with 100 mM potassium chloride as the supporting electrolyte. The CV data of the devices treated with different plasma treatment times is shown in Figure 2.3a.

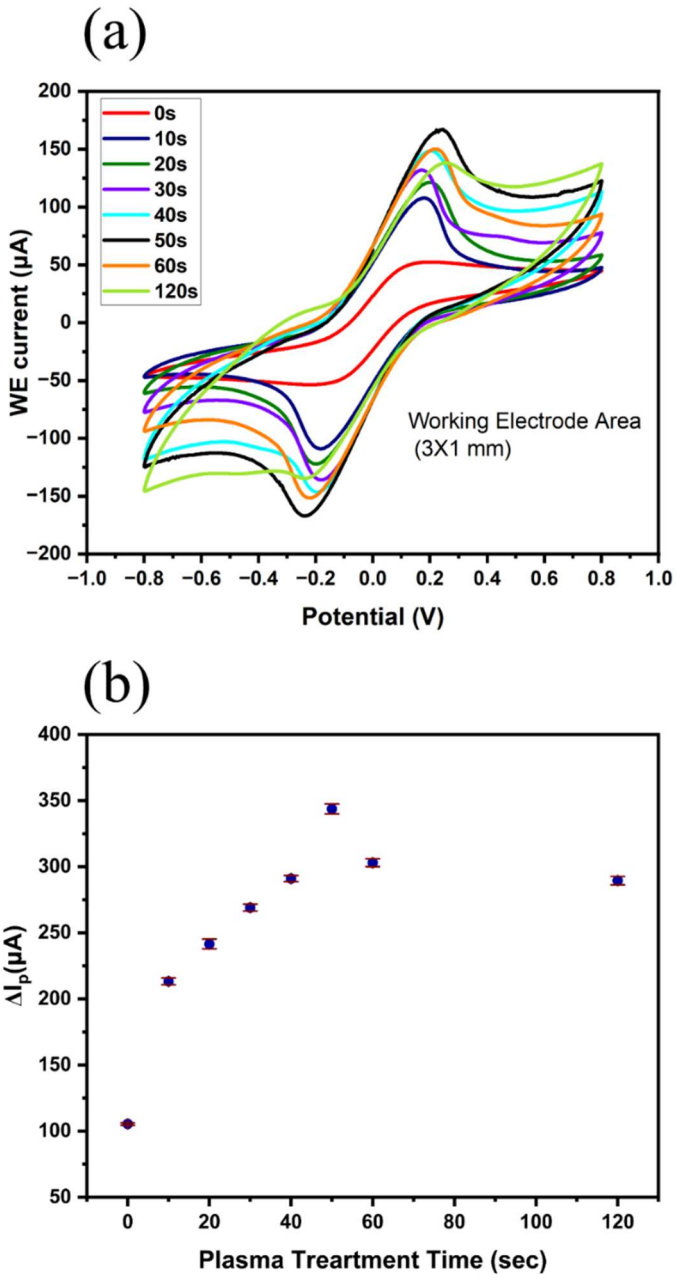

Figure 2.3. Effect of plasma treatment time on electrochemical performance (a) CV measurements for devices subjected to different plasma treatment durations as shown in the legend. (b) Plot of peak-to-peak current (ΔIp) as a function of plasma treatment.

The y-axis represents the WE current in this figure, while the x-axis corresponds to the applied potential. The difference between the anodic and cathodic peak currents (ΔI_p) as a function of plasma treatment time is shown in Figure 2.3b. The oxidation peaks in all measurements are observed within the potential range of 0.15 V to 0.25 V. In comparison, the reduction peaks are detected between -0.1 V and -0.25 V. These values closely correspond to those reported in the literature for this analyte, confirming the consistency of the results [106].

The results presented in Figures 2.3(a,b) demonstrate that air plasma treatment significantly enhances the performance of the three-electrode LIG system. For instance, the ΔI_p value of the untreated three-electrode system is 105.4 μA which improved markedly to 213.3 μA following 10 seconds of plasma exposure. The value continues to rise, reaching 343.7 μA at 50 seconds of plasma treatment. However, a decline in performance was observed with extended plasma exposure, with ΔI_p values decreasing to 303 μA at 60 seconds and 289.66 μA at 120 seconds. The improved sensor performance after air plasma treatment is attributed to changes in LIG surface properties, including increased hydrophilicity and electrocatalytic activity. However, overexposure (>50 s) introduces defects that reduce conductivity and sensor performance. The following sections will discuss these trends in detail.

2.3.3 CV Based LOD and LOQ Analysis

To determine the LOD and LOQ for both untreated and optimized plasma-treated devices (50s treatment), CV scans were conducted at varying analyte concentrations to generate a dose-response curve for each device. A detailed explanation about how the LOD and LOQ was determined is provided in the method section. Figure 2.4(a, b) show the CV data for all analyte concentrations

under untreated and plasma-treated conditions. To provide a clearer view of the variations at lower concentrations, Figures 2.4(c, d) show a zoomed-in analysis focusing on the 0.04 mM–1 mM range. Figure 2.4e illustrates the dose-response curves of the two devices and the variation in peak-to-peak current across these conditions.

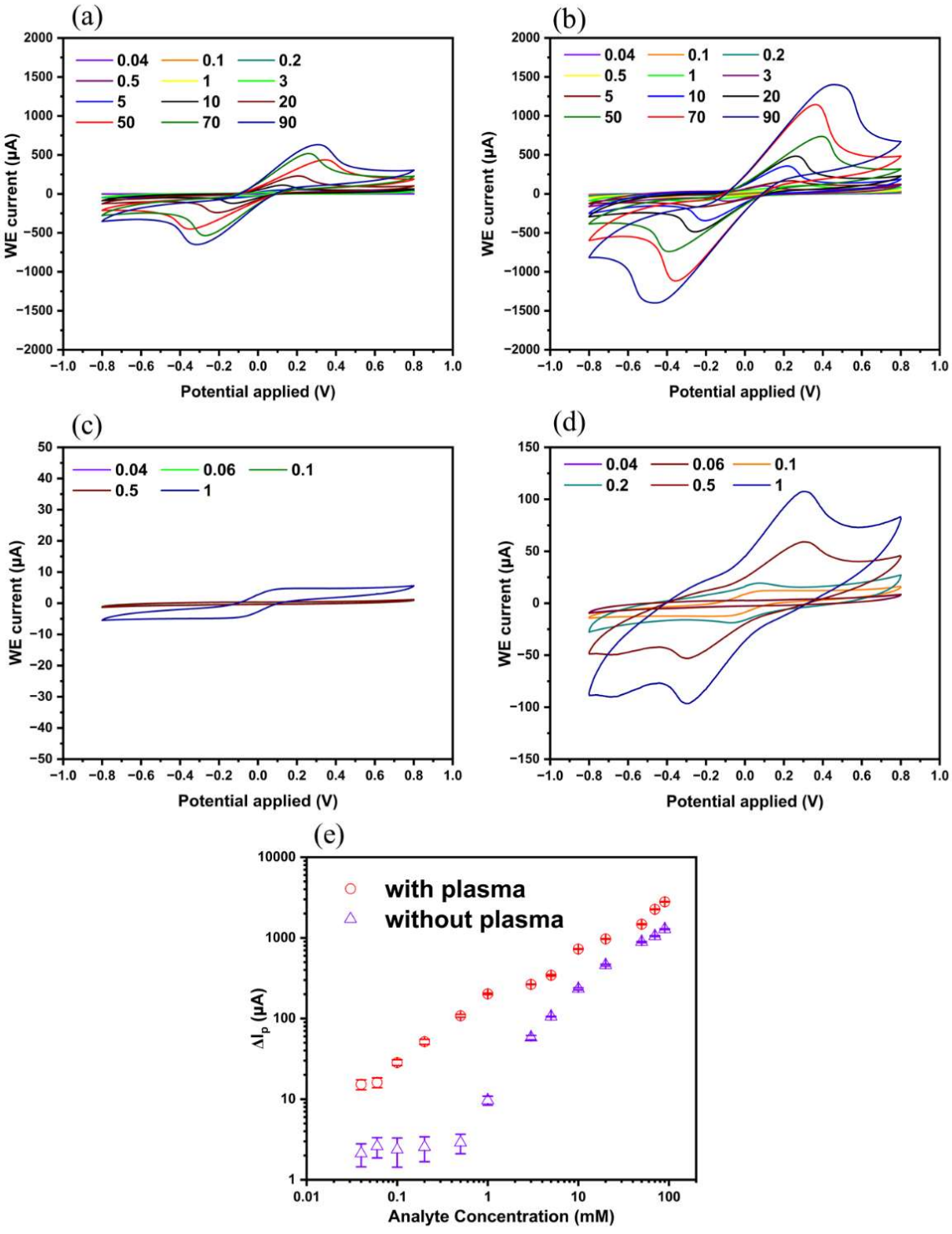
(a)
0.04
0.1
0.2
0.5
1
3
5
10
20
50
70
90
WE current (μA)
Potential applied (V)
(b)
0.04
0.1
0.2
0.5
1
3
5
10
20
50
70
90
WE current (μA)
Potential applied (V)
(c)
0.04
0.06
0.1
0.5
1
WE current (μA)
Potential applied (V)
(d)
0.04
0.06
0.1
0.2
0.5
1
WE current (μA)
Potential applied (V)
(e)
with plasma
without plasma
ΔIp (μA)
Analyte Concentration (mM)

Figure 2.4. CV responses for varying analyte concentrations (legends in mM) in (a) untreated devices and (b) devices subjected to a 50-second oxygen plasma treatment. To examine peak current at lower analyte concentrations (0.04 mM–1 mM), CV results are presented for (c) untreated and (d) plasma-treated devices. (e) Plot of ΔIp as a function of analyte concentration. At high concentrations, ΔIp increases monotonically with concentration. At very low concentrations, ΔIp is not a function of concentration and no detectable peaks were observed. The concentration at which the peak becomes distinguishable from the blank solution transitioning between regimes is higher for untreated electrodes.

The analysis reveals that detectable peaks were observed for untreated devices at a minimum concentration of 1 mM. For the untreated sensors, concentrations below 1 mM did not produce detectable peaks, resulting in ΔI_p values comparable to those of the blank solution. However, a linear increase in current was observed from 1 mM onwards, continuing with higher concentrations. In contrast, the plasma-treated devices (treated for 50 seconds) showed detectable peaks at concentrations as low as 100 µM, with a corresponding linear rise in current as concentration increased. Based on this observation, the LOD for the treated devices was calculated according to the methods mentioned earlier. As illustrated in Figure 2.5(a, b), a linearity assessment was performed using the coefficient of determination (R^2) to evaluate the relationship between the current response and analyte concentration for both untreated and 50 s plasma-treated samples. The analysis revealed that the concentration range of 1–20 mM for untreated devices demonstrated the highest R^2 value, whereas for plasma-treated devices, the optimal linear range was found between 0.1–1 mM. Based on the identified linear regions, the calculated sensitivity (slope values) were 24.3 µA/mM for untreated samples and 192.9 µA/mM for plasma-treated samples, while the corresponding y-intercepts were determined as -14.7 µA and 10.24 µA.

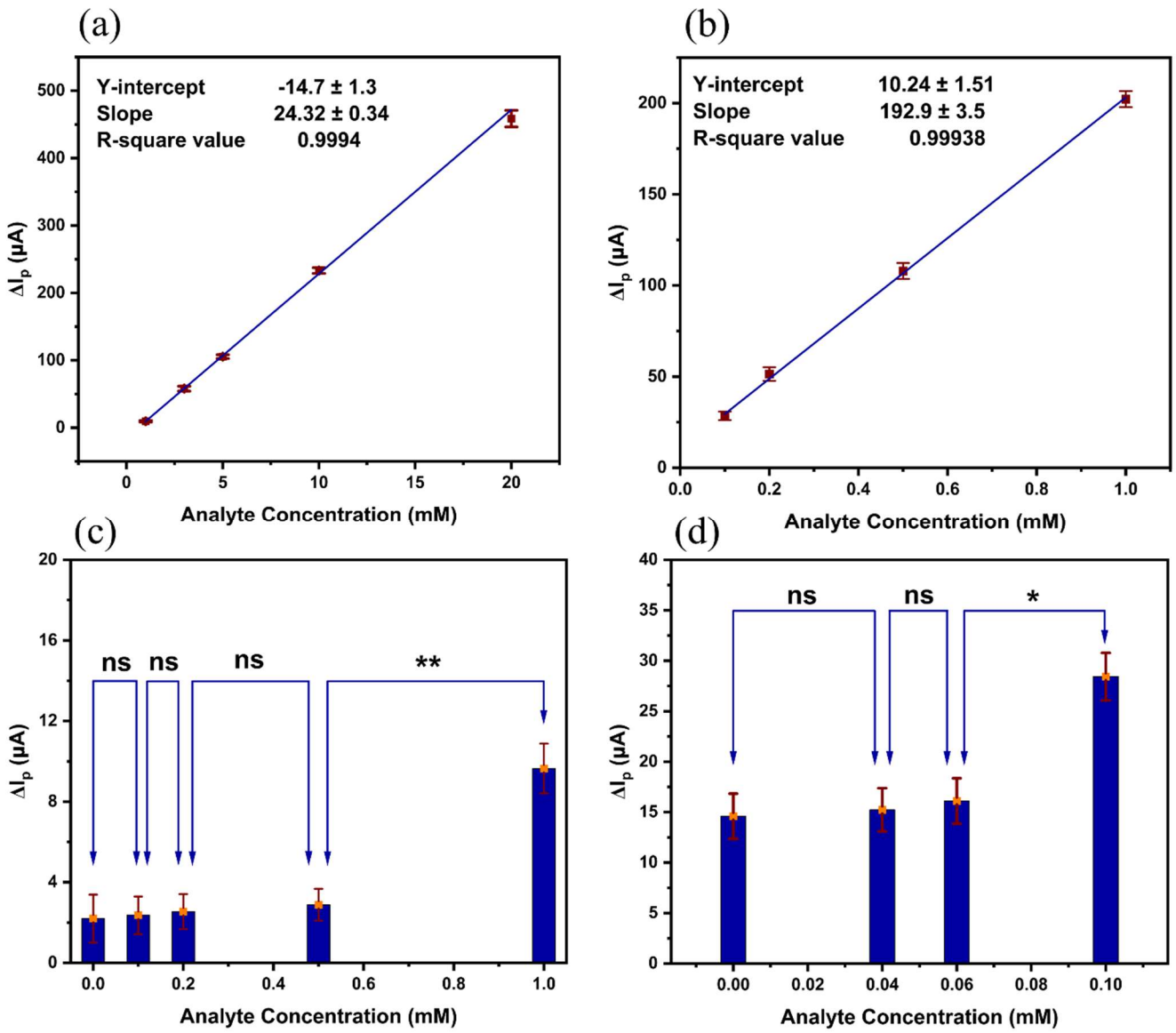

*Figure 2.5. Linear region of the ΔIp vs analyte concentration plot used to determine the y-intercept and slope for sensitivity, LOD and LOQ calculation under (a) untreated conditions (1–20 mM) and (b) 50s plasma-treated conditions (0.1–1 mM). T-test results evaluating the statistical reliability of the LOD calculation for (c) untreated devices within the concentration range of 0–1 mM and (d) plasma-treated devices within the concentration range of 0–0.1 mM. Statistical significance is denoted as $p < 0.05$ (significant, *), $p < 0.01$ (highly significant, **), and $p < 0.001$ (very highly significant, ***)*

Furthermore, statistical analysis was conducted to validate the calculated LOD values. Figure 2.5c presents a t-test analysis assessing the statistical differences in peak current across various analyte concentrations. For the untreated sensor, no distinguishable peaks were detected at 0, 0.1, 0.2, and 0.5 mM, whereas at 1 mM, a statistically significant increase in peak current was observed, confirming a detectable sensor response. This indicates that the LOD for the untreated sensor falls within the transition range of 0.5–1 mM, where the device begins to exhibit a measurable signal. Similarly, Figure 2.5d provides a t-test analysis for the plasma-treated sensor, demonstrating that no significant peak currents were detected at 0, 0.04, and 0.06 mM. However, at 0.1 mM, a statistically significant increase in peak current was observed, signifying a meaningful sensor response. These results confirm that the LOD for the plasma-treated sensor lies between 0.06 mM and 0.1 mM, marking the threshold at which the peak current becomes significantly distinguishable from baseline levels. Using the established equation (3), the LOD in terms of concentration was calculated as 0.07 mM (70 μM) for the plasma-treated sensors, while it was significantly higher at 0.927 mM for the untreated sensors. The LOQ was determined to be 0.132 mM for the treated devices and 1.837 mM for the untreated devices. The sensitivities of both the 50s treated and untreated sensors were calculated to be 192.9 μA/mM and 24.32 μA/mM, respectively. This significant enhancement in sensitivity, LOD, and LOQ highlights the role of plasma treatment in improving device performance.

2.3.4 Electrochemical Impedance Spectroscopy

To investigate the impact of different plasma exposure times on the properties of the electrode-electrolyte interface, EIS was conducted on the fabricated devices with three different plasma

treatment conditions: untreated, optimized treatment (50 seconds, as determined in the previous section), and extended treatment (120 seconds) to assess the effects of overexposure. The Nyquist plots of the impedance of the three plasma conditions are shown in Figure 2.6(a-c), including the fitted line based on the equivalent circuit model shown in Figure 2.6d. Figure 2.6e shows a comparison of all three conditions. A comparison of the R_s, R_{ct}, C_{dl}, and W_e is presented in Figure 2.6(e-h) with the result of a t-test showing the significance of the difference between the conditions.

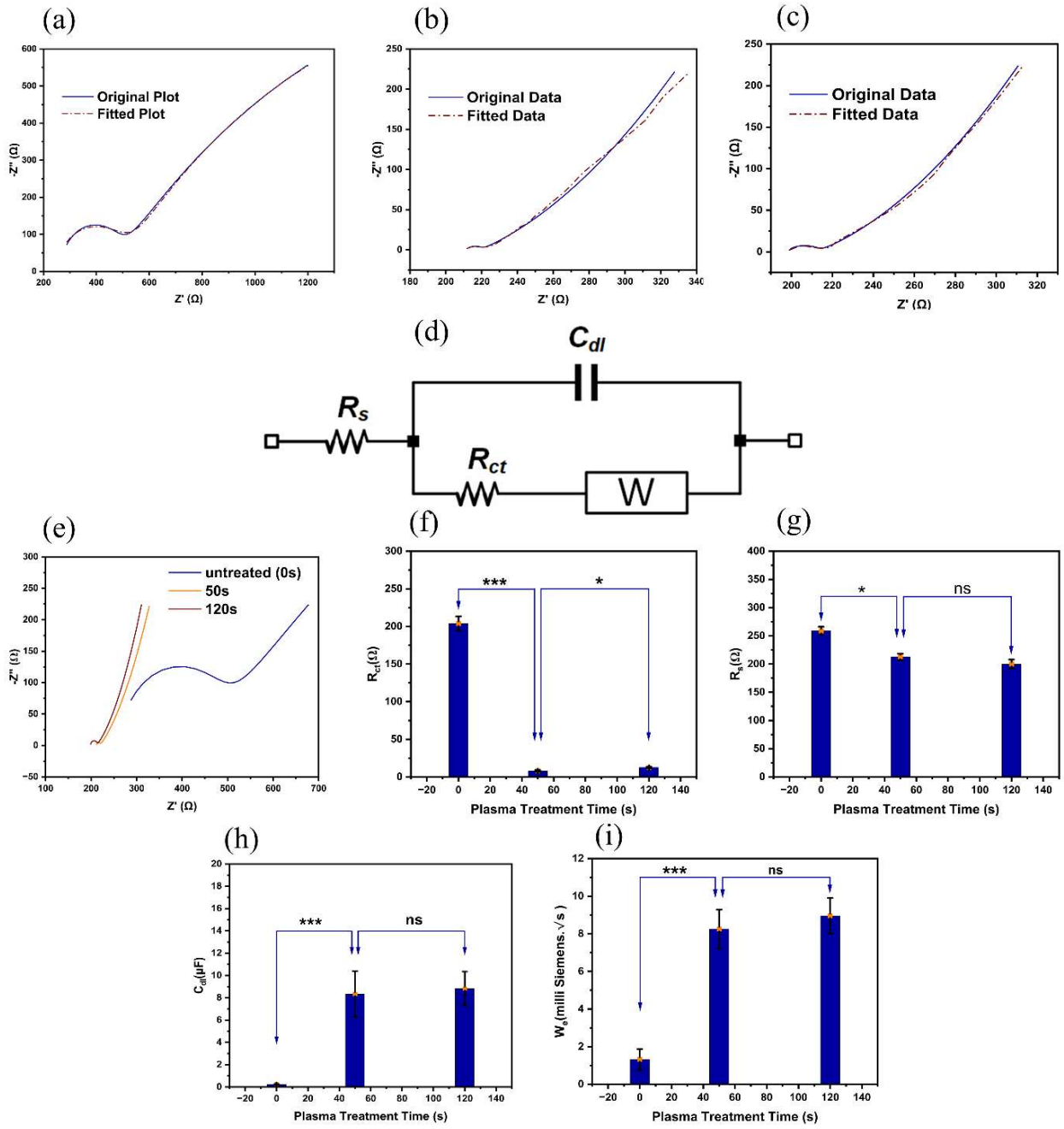

Figure 2.6. EIS analysis of LIG electrodes. Nyquist plots showing the impedance responses of electrodes with different plasma treatment times: (a) untreated, (b) 50 s plasma-treated, and (c) 120 s plasma-treated electrodes. (d) The equivalent circuit model is used for calculating R_s, R_{ct}, C_{dl}, and W_e. (e) Comparative analysis of the impedance data for all three conditions presented on a single plot. (f–i)

Effect of plasma treatment time on key electrochemical parameters, with statistical significance indicated by p-values: (f) R_{ct} decreases significantly from 0 to 50 s ($p = 0.00015$) but increases at 120 s ($p = 0.014$) (g) R_s shows a moderate decrease from 0 to 50 s ($p = 0.016$) but remains largely unchanged from 50 to 120 s ($p = 0.073$). (h) C_{dl} increases significantly from 0 to 50 s ($p = 0.000726$) but stabilizes between 50 and 120 s ($p = 0.41$) (i) W_e follow a similar trend, with a significant increase from 0 to 50 s ($p = 0.00013$) but no substantial change beyond 50 s ($p = 0.14$). Statistical significance is denoted as follows: $p < 0.05$ *(*),* $p < 0.01$ *(**), and* $p < 0.001$ *(***).*

The data indicate that plasma treatment significantly reduces charge transfer resistance, which represents the resistance ions encounter when moving from the electrolyte to the electrode during a reaction [108]. Plasma treatment introduces oxygen-containing functional groups onto the electrode surface, significantly improving its affinity for the electrolyte. This enhanced electrode-electrolyte interaction facilitates more efficient charge transfer, leading to a marked reduction in R_{ct} (Figure 2.6(f)). For instance, the device treated for 50 seconds shows a R_{ct} of 7.86 ± 1.12 Ω, a significant decrease compared to the untreated sample, which has a R_{ct} of 203.65 ± 9.56 Ω. However, prolonged plasma exposure (120 seconds) increases R_{ct}, reaching 12.4 ± 0.85 Ω. This rise in R_{ct} highlights that while plasma treatment enhances electrochemical performance at 50 s, excessive exposure (120 s) leads to an increase in R_{ct}, reducing charge transfer efficiency. It is likely due to the disruption of the conductive network at the surface of the electrode, which is caused by an overabundance of defects on the surface. These defects negatively impact the electrode-electrolyte interaction, reducing charge transfer efficiency [109]. The 50-second treatment duration provides optimal performance, as also evidenced by the improved CV results in Figure 2.3.

As plasma treatment duration increases, the solution resistance R_s decreases (Figure 2.6(g)). Precisely, R_s is measured at 258.7 ± 7.45 Ω for the untreated sample, reducing to 212.6 ± 5.96 Ω after 50 seconds of plasma treatment. A further decline to 199.2 ± 8.12 Ω is observed following 120 seconds of treatment, indicating a progressive reduction in R_s with extended plasma exposure. This reduction in solution resistance can be attributed to the enhanced wettability of the porous electrode, which allows more liquid electrolyte to penetrate it, thus lowering its electrical resistance. As the treatment time increases, the plasma effectively removes contaminants and residues from the electrode surface, resulting in a cleaner, more accessible surface. This improved surface integrity allows ions to approach the electrode more easily, enhancing ionic conduction.

The electric double layer formed at the interface between an electrode and an electrolyte functions as a capacitor [110]. Therefore, an increase in the electrode's active surface area enhances the capacitance of this double layer. Plasma treatment of the electrode surface significantly increases its active area, promoting greater interaction between the electrode and the analyte. As a result, the capacitance of the plasma-treated electrodes is substantially higher (Figure 2.6h). Specifically, for electrodes treated for 50 seconds and 120 seconds, the C_{dl} values are 8.33 ± 2.07 μF and 8.82 ± 1.53 μF, respectively, compared to the much lower capacitance of the untreated devices, which is 0.235 ± 0.04 μF. This increase in capacitance highlights the improved electrode-analyte interaction enabled by plasma treatment, enhancing the overall electrochemical performance.

The Warburg element values (Figure 2.6i) for plasma-treated devices are significantly higher than those of the untreated devices, which exhibit a value of 1.32 ± 0.56 $mS \cdot s^{0.5}$. There is no substantial difference between the plasma-treated devices, with W_e values of 8.25 ± 1.03 $mS \cdot s^{0.5}$ for the 50-

second treatment and 8.95 ± 0.95 $mS \cdot s^{0.5}$ for the 120-second treatment. These results indicate that plasma exposure enhances analyte diffusion at the electrode surface, which is markedly weaker in the untreated devices.

2.3.5 Effect of Plasma Treatment on the Contact Angle of LIG Surface Over Time

To understand the impact of plasma treatment duration on electrochemical performance, we conducted physical characterization of LIG, beginning with wettability analysis. To investigate the wettability, change as a function of varied plasma treatment duration, contact angle of deionized water on LIG samples subjected to varying plasma treatment durations was measured and is shown in Figure 2.7a. The inset images illustrate the variation in contact angle on the LIG samples, corresponding to different plasma treatment durations. The treatment times range from no plasma treatment up to 120 seconds, with a constant power setting of 25 W. The data shows that the contact angle decreases significantly with increasing plasma treatment time. Initially, without plasma treatment, the contact angle was 123.4° ± 7.04°. After just 10 seconds of treatment, it drops to 31.2° ± 5.81°, representing a reduction of approximately 75%. As the treatment time increases, the contact angle decreases progressively, reaching 0° at 120 seconds of plasma exposure. The observed variations can be explained by changes in the amount of oxygen containing chemical groups on the surface of the LIG samples, which will be examined in detail in the following section. Figure 2.7b illustrates the effect of plasma treatment duration on LIG samples over a 14-day storage period under ambient conditions.

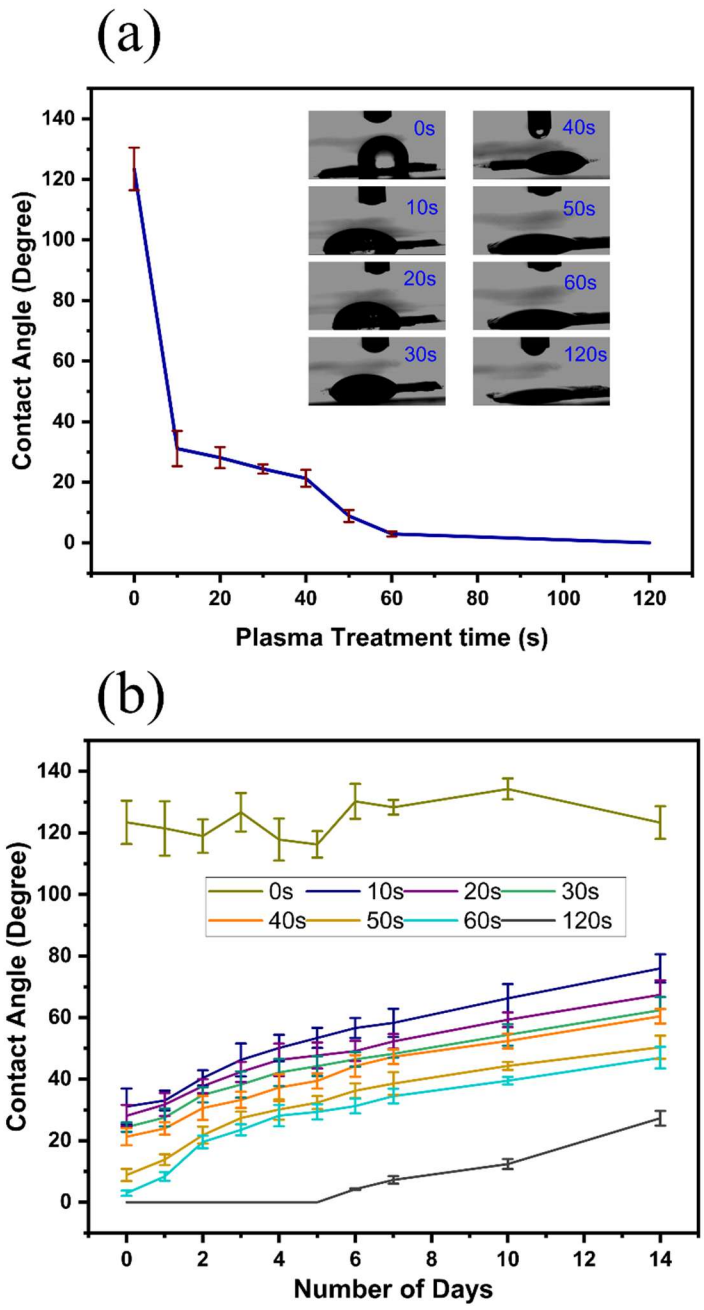

Figure 2.7. Effect of plasma treatment on wettability and its long-term stability(a) Influence of plasma treatment duration on the wettability of LIG surfaces, measured by the contact angle of a DI water droplet, with inset images showing droplet behavior on treated surfaces. (b) Long-term stability of wettability over 14 days for LIG surfaces with different plasma treatment durations.

The data show that while the contact angle remains constant for the untreated sample, it gradually increases over time for all plasma-treated samples, indicating a decrease in wettability. However, the effect of plasma treatment persists even after 14 days, as none of the treated surfaces return to the contact angle of the untreated sample.

Specifically, the sample treated for 10 seconds exhibited a contact angle increase of approximately 45° over 14 days, reaching 76°, suggesting that it remained hydrophilic. Similarly, the 50-second treated sample showed an increase of 41°, with a final contact angle of 50.37°, while the 120-second treated sample exhibited a smaller increase of 27°. These findings demonstrate that although wettability gradually decreases over time, plasma treatment effectively enhances surface hydrophilicity, with its influence remaining evident even after two weeks.

These results indicate that increasing plasma treatment duration enhances surface wettability. However, the underlying reason why excessive exposure negatively impacts performance remains unclear. Further investigation, presented in the following sections, explores additional factors influencing this phenomenon.

2.3.6 X-ray Photoelectron Spectroscopy (XPS) Analysis

To examine the reason behind the effect of plasma treatment duration on the wettability of LIG samples, XPS analysis was conducted on three sample groups: untreated, 50 s plasma-treated, and 120 s plasma-treated. Figure 2.8(a-c) presents the elemental composition of the surface. The data indicate a progressive increase in oxygen concentration on the surface of the LIG samples with extended plasma treatment time, accompanied by a corresponding decrease in carbon concentration. This trend is quantitatively represented in the atomic concentration plot in Figure

2.8j, where the carbon content is shown to decrease from 75.4% in untreated samples to 64.4% and 54.7% after 50 s and 120 s of plasma exposure, respectively.

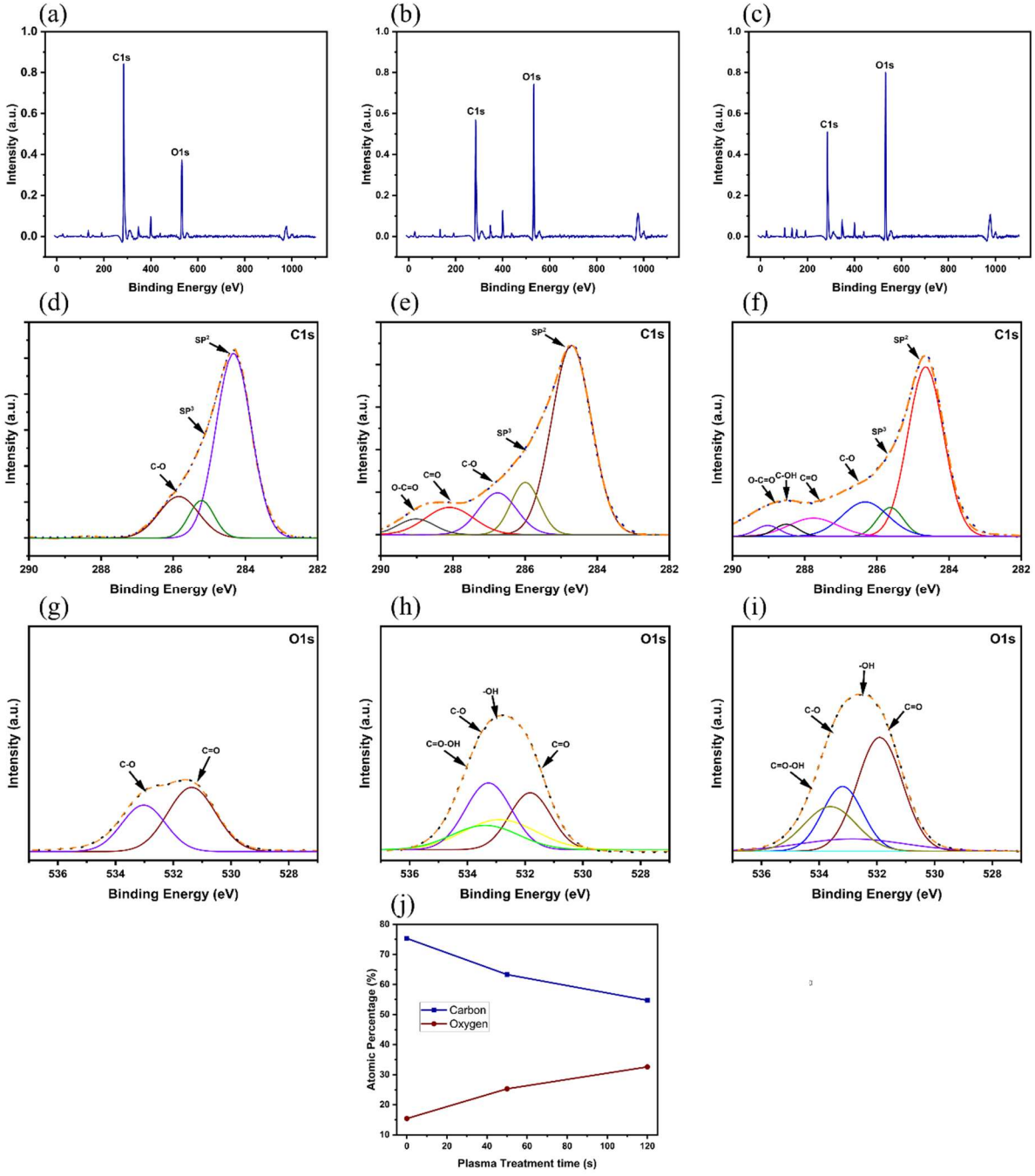

*Figure **2**.8. XPS survey spectra for LIG samples at varying plasma treatment durations: (a) untreated, (b) 50 s treated, and (c) 120 s treated. Detailed C1s spectra for (d) untreated, (e) 50 s treated, and (f) 120 s treated samples, alongside O1s spectra for (g) untreated, (h) 50 s treated, and (i) 120 s treated LIG, illustrating changes in surface chemistry with increasing treatment time. (j) Atomic percentages of carbon and oxygen as a function of plasma treatment duration, showing increasing oxygen and decreasing carbon content with increasing exposure time.*

Conversely, oxygen concentration of the untreated sample is 15.8% which is found higher as 25.4% and 32.6% for 50 s and 120 s plasma treated samples, respectively. The C1s spectrum, presented in Figure 2.8(d-f) was deconvoluted into distinct peaks corresponding to different chemical states, based on their individual binding energies: sp^2 (284.5 eV), C-O (285.9 eV), C=O (288.2 eV), O-C=O (289.1 eV), and -CHO (288.4 eV) [111]. The results indicate that the 120s plasma-treated sample shows a prominent presence of all the peaks mentioned, including C–O, C=O, and O–C=O and CHO. However, in the 50 s treated sample, the presence of all the functional groups was found but their intensity was significantly less compared to the 120 s plasma treated sample. These findings show that as the treatment time increased, the intensity of polar oxygen functional groups increased significantly. As a result, the interaction of water with the surface was much stronger, causing the increase in the wettability of the surface as observed in Figure 2.7 [99]. The O1s spectra also contain C-O (≈533.5 eV) and C=O (≈531.9 eV) groups as presented in Figure 2.8(g- i) [57]. The findings highlight the significant influence of plasma treatment duration on the peak intensity of oxygen-containing surface groups in LIG samples. Functional groups such as carbonyl (C=O) and carbon-oxygen (C-O) forming on the LIG surface during plasma exposure are

critical in enhancing wettability. Increased wettability, in turn, improves the interaction between the electrolyte and the electrode surface, facilitating more effective electrochemical performance [112]. These surface groups may also create active sites that facilitate the interaction of electroactive atoms. Consequently, as plasma treatment time increases, the number of active sites and the wettability of the LIG surface are enhanced, leading to improved electrochemical reactivity and overall performance.

2.3.7 Raman spectroscopy analysis of the LIG samples

Raman spectroscopy was conducted to evaluate the quality of LIG and to understand the factors influencing the performance of the LIG-based sensor. This analysis aimed to identify the reasons behind the initial increase in sensor performance and the subsequent decrease observed after a specific time limit. It is a widely utilized non-destructive technique that identifies structural defects within carbon-based materials like LIG. Raman spectra of the LIG samples with different plasma treatment times are depicted in Figure 2.9a.

The Raman spectrum of the untreated (0s) LIG material reveals the presence of distinct peaks positioned around 1349.6 cm^{-1} and 1587.9 cm^{-1}, representative of the D and G bands, respectively. Correspondingly, the oxygen plasma-treated LIG materials with different treatment times exhibit symmetrical representative peaks within the identical spectral region. The G band in the Raman spectrum, typically observed around 1580 cm^{-1}, is attributed to the in-plane vibrations of sp^2-bonded carbon atoms within the graphene lattice. Conversely, the D band, located near 1350 cm^{-1},

signifies structural defects, disorder, and the presence of sp^3-hybridized carbon atoms in the graphene structure [113] [114].

The intensity ratios of D and G peaks (I_D/I_G) for LIG with different exposure times to oxygen plasma treatment is shown in Figure 2.9b.

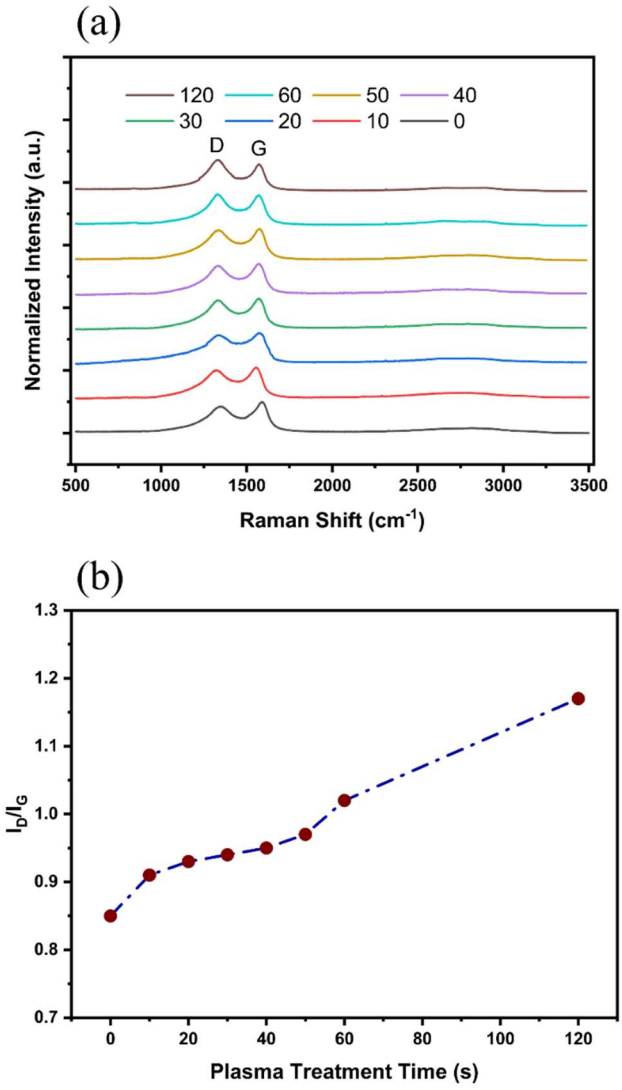

Figure 2.9. (a) Raman spectroscopy analysis of LIG samples subjected to varying plasma treatment durations. (b) ID/IG ratio as a function of plasma treatment duration shows a rise in the ratio, corresponding to an increasing defect density with longer exposure times, ultimately affecting the overall quality of graphene.

The I_D/I_G ratio in the Raman spectra is a key indicator of the quality and structural properties of graphene, serving as an indication of heightened disorder within the structure as the oxygen plasma-treatment time increases. A higher ratio indicates more defects in the graphene structure. Defects can increase the density of active sites, and internal roughness within the material, which might enhance electron transfer [115].

2.3.8 Variation of Sheet Resistance with Different Plasma Treatment Time

The sheet resistance of the LIG samples was measured as a function of plasma treatment duration to assess the impact of extended exposure on conductivity. The results in Figure 2.10 illustrate the variations in sheet resistance following different plasma treatment times.

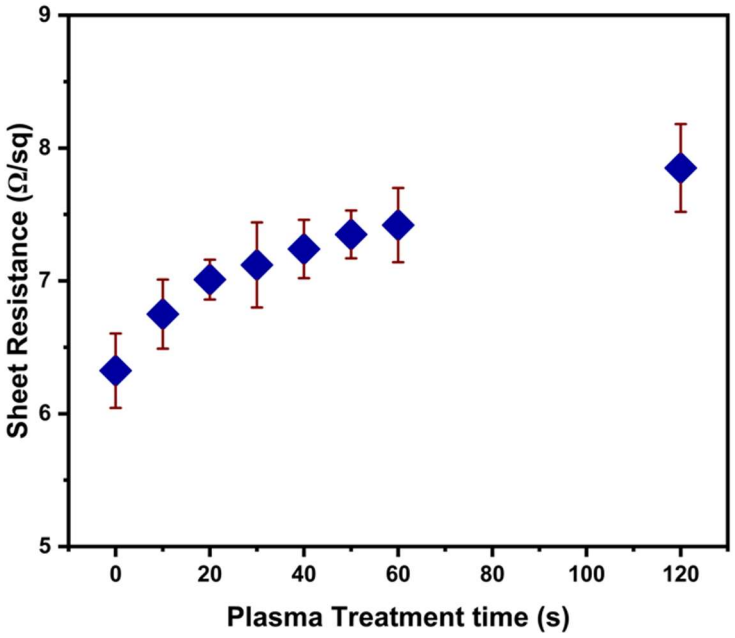

Figure 2.10. Sheet resistance of LIG samples to assess the impact of plasma treatment on their electrical properties. The resistance slightly increases with longer treatment durations, indicating changes in the material's conductivity due to extended plasma exposure.

The sheet resistance measurements indicate that increasing the plasma treatment time affects the conductive network of LIG electrodes, leading to a rise in sheet resistance. Initially, the untreated samples exhibited a sheet resistance of 6.324 ± 0.28 Ω/sq. However, with increased treatment duration, the resistance gradually rises, reaching 7.35 ± 0.18 Ω/sq at 50 seconds of plasma exposure, and further extending the treatment time to 120 seconds results in an even higher sheet resistance of 7.85 ± 0.35 Ω/sq. This trend suggests that prolonged plasma treatment can disrupt the conductive network of LIG due to the excessive introduction of surface defects, which are known to hinder electrical conductivity [109] .

2.3.9 Scanning Electron Microscopy (SEM) of the LIG samples

SEM analysis was performed to compare the surface morphology of LIG samples following different types of plasma treatment. The images captured after varying treatment durations are presented in Figure 2.11.

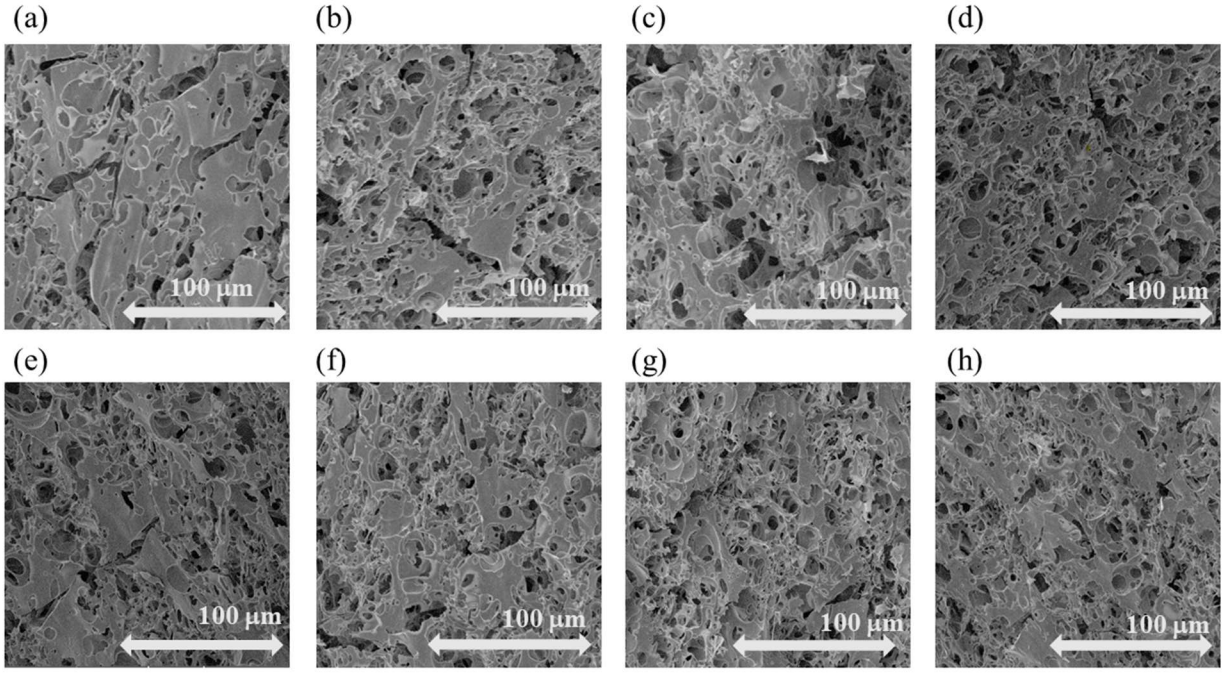

Figure 2.11. SEM images of LIG samples show no significant impact of plasma treatment on their morphological properties. The samples were subjected to plasma treatment for varying times: (a) 0 seconds, (b) 10 seconds, (c) 20 seconds, (d) 30 seconds, (e) 40 seconds, (f) 50 seconds, (g) 60 seconds, and (h) 120 seconds.

Plasma treatment is a simple and non-destructive technique primarily used to enhance surface wettability and is not expected to cause significant structural or morphological changes to the LIG surface. The findings from SEM analysis support this, showing no notable alterations in the morphology of LIG samples subjected to varying plasma treatment durations. These results

suggest that while plasma introduces defects and surface functional groups, they do not lead to any substantial morphological modifications in the LIG structure.

2.3.10 Durability and Stability of Plasma-Treated Sensors

To assess the durability of the sensors after plasma treatment, their performance was evaluated over a 14-day period using the same CV setup. Two conditions were tested: a control group consisting of sensors without plasma treatment and a test group treated with 50 seconds of plasma, which had demonstrated the highest CV performance based on peak current. Each day, two devices from each group were analyzed, and the average difference between the anodic and cathodic peak currents was plotted. The results presented in Figure 2.12 indicate that over the 14-day period, the performance of both sensor groups remained stable. This suggests excellent durability and long-term stability of the sensors even after the plasma treatment.

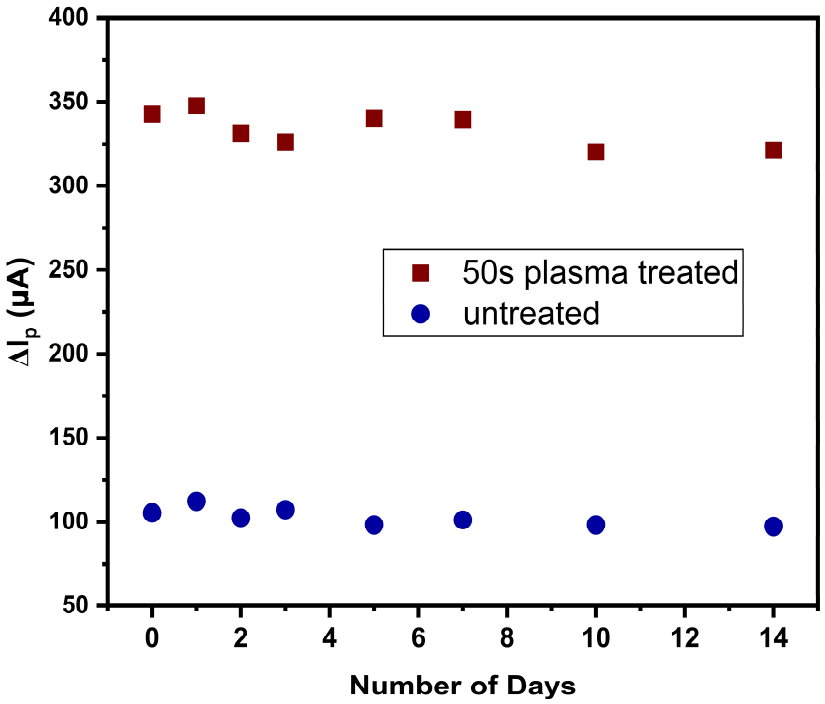

Figure 2.12. Comparative analysis of CV peak to peak currents for untreated and 50 s plasma-treated sensors, recorded daily over a 14-day period. Both untreated and 50 s plasma-treated sensors exhibit consistent electrochemical performance, indicating stability and reliability over time.

2.4. Discussion

The impact of plasma treatment duration on the performance of LIG-based electrochemical sensors reveals a key balance between beneficial surface modifications and excessive structural changes. The observed trends in CV and EIS indicate that moderate plasma exposure enhances sensor performance, whereas prolonged treatment introduces adverse effects.

The initial increase in anodic and cathodic peak currents with plasma treatment up to 50 seconds can be attributed to introducing oxygen-containing functional groups, as confirmed by XPS. These functional groups enhance surface hydrophilicity, improving electrolyte accessibility and charge

transfer dynamics [57]. The reduction in solution and charge transfer resistances observed in EIS further supports this, indicating an improvement in ionic conductivity and charge transfer efficiency. Additionally, the increase in electric double-layer capacitance and the reduction in the Warburg impedance suggest more efficient ion diffusion and enhanced interfacial charge transfer, which is crucial for optimal sensor performance [106].

Prolonging the plasma treatment led to a decline in electrochemical performance, as the increase in charge transfer resistance by approximately 20% suggests that excessive surface modification may introduce defects that hinder electron mobility. Raman spectroscopy further corroborates this observation, showing a progressive increase in the I_D/I_G ratio with longer treatment times, indicative of defect formation [115]. While moderate defect density improves conductivity, excessive defects disrupt the conductive network, leading to performance degradation [109]. The balance between functionalization and structural integrity is thus a key determinant in optimizing plasma treatment duration.

An important performance indicator of electrochemical sensors is their LOD, LOQ, and sensitivity. Our results demonstrate significant improvement in these sensor performance parameters for the 50-second plasma-treated device compared to the untreated sensor. This substantial enhancement underscores the effectiveness of plasma treatment in increasing the sensitivity of LIG-based sensors. The durability tests further confirm the stability of both untreated and treated devices over 14 days, reinforcing the reliability of these sensors for prolonged use.

2.5 Conclusion

In conclusion, this study demonstrates the significant impact of plasma treatment time, at a specific power level, on performance of LIG-based electrochemical sensors. Our findings reveal that plasma treatment enhances sensor performance only up to an optimal threshold time, beyond which further treatment time leads to decreased performance compared to the optimal point. At 25 W plasma power, a treatment duration of 50 s resulted in a 225% increase in peak current, significantly improving CV response. However, exceeding this duration did not improve the sensor's performance; instead, compared to 50 s, it decreased. This trend can be attributed to increased wettability and defect formation due to plasma exposure. While enhanced wettability generally improves electrochemical interactions, excessive defects beyond a specific treatment duration disrupt charge transfer, despite wettability reaching its maximum. Defect formation becomes the dominant factor, emphasizing that wettability alone is insufficient for effective electrochemical performance. These results emphasize the need for precise control of plasma treatment parameters to maximize the electrochemical efficiency of LIG-based sensors and avoid detrimental over-processing effects. All three sensor electrodes were fabricated without additional modifications through direct laser scribing on a Kapton tape. This approach significantly simplifies the fabrication process compared to traditional methods, making it both cost-effective and scalable for large-scale production. Such a method holds immense potential for the development of affordable, high-performance sensors. Additionally, the durability testing of the sensors offers valuable insights into their long-term stability and reliability, further underscoring the viability of this fabrication technique for practical, long-term applications in various sensing environments.

3. Lithium Manganese Oxide-Modified Laser Induced Graphene Electrodes for Lithium Detection

3.1 Introduction

The widespread use of lithium-ion batteries in electric vehicles has increased the amount of battery waste, where improper disposal and limited recycling contribute to lithium contamination in groundwater [8]. Another primary application of lithium detection is lithium extraction. Lithium is considered one of the most essential energy metals of the 21st century [116]. Due to the limited global supply, extracting lithium from natural sources remains essential for supporting the rapid growth of emerging industries. In both field detection and extraction processes, there is a pressing need for effective, easy-to-fabricate lithium sensors that are user-friendly and suitable for real-world applications.

In Chapter 2, we investigated the effect of plasma treatment duration on LIG electrodes. We observed improved CV current and a lower LOD for the potassium ferrocyanide/potassium ferricyanide redox system with an optimized treatment time of 50s. However, when tested in LiCl solution, the plasma-treated electrodes with optimized treatment time of 50s failed to exhibit any distinct electrochemical peaks, indicating a lack of selectivity toward lithium ions. This limitation highlighted the need for further surface modification to impart lithium-ion detection. Accordingly, this study presents a simple and cost-effective method for lithium detection using LIG modified with LMO. LMO is known for its strong selectivity toward lithium, enabling efficient lithium-ion insertion into the electrode [7]. While previous studies applied LMO to traditional electrodes such as SPEs and GCEs, our work is the first to utilize LIG as the electrode for lithium detection. By

integrating LMO onto the LIG surface through dispense printing, we achieved a uniform coating for the modified layer. This approach offers a rapid, low-cost, and easy-to-fabricate detection technique, highlighting the credibility of LIG-based platforms for lithium sensing applications.

3.2 Material and Methods

3.2.1 Materials and Chemical Reagents

In addition to the materials and chemicals reported in Chapter 2, lithium chloride (LiCl), potassium chloride (KCl), sodium chloride (NaCl) and lithium manganese oxide (Li_2MnO_4) were purchased from Sigma-Aldrich (Oakville, Canada).

3.2.2 LIG Electrode Fabrication and Dispense Printing of LMO Layer

The three electrodes of LIG were fabricated as mentioned in the method mentioned in section 2.2 (Figure 3.1a (i, ii)). After the fabrication of three electrodes, the LMO layer was printed using dispense printing with an SDS-5 3D printer extruder and Hydra 16 A printer. Following the dispense printing of the LMO layer, the three-electrode system was thermally cured in an oven at an elevated temperature for 30 minutes, which was optimized between 60 and 210°C with 30°C steps. Figures 3.1(b, c) show the optical micrographs of the three-electrode system before and after the modification of the WE with LMO, respectively. Figure 3.1b shows the unmodified system, while Figure 3.1c illustrates the LMO-modified WE following thermal curing.

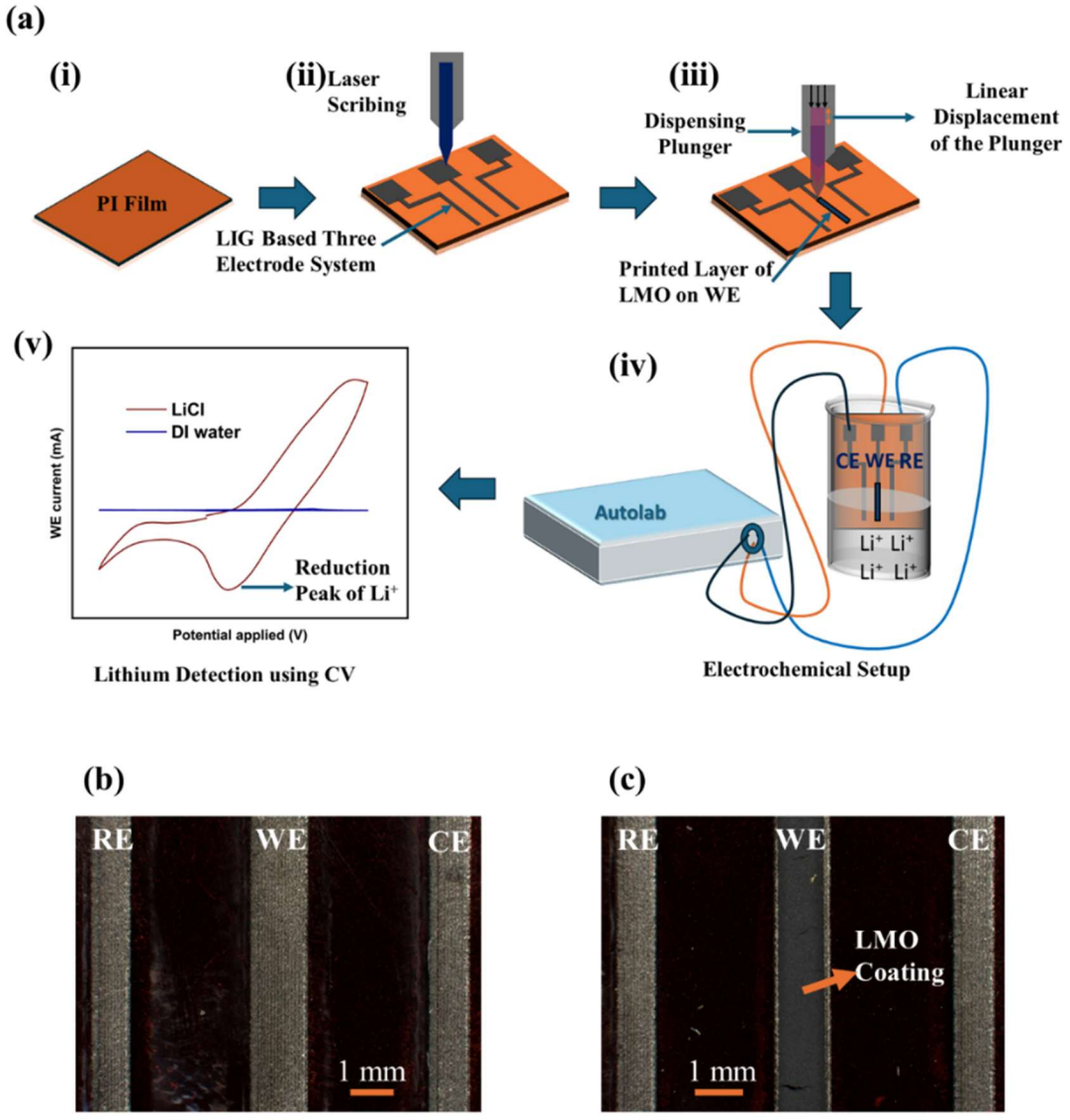

Figure 3.1. LIG electrodes fabricated for electrochemical detection of lithium (a) Schematic representation of the fabrication process: (i) preparation of the PI film substrate, (ii) laser scribing to form the LIG-based three-electrode system, (iii) dispense printing of the LMO layer onto LIG WE to enhance lithium detection, (iv) electrochemical testing setup for performance evaluation, and (v) CV results demonstrating lithium detection. (b) Optical micrograph of the fabricated LIG three electrode system (RE, WE, and CE) without LMO modification. (c) Optical micrograph of the fabricated LIG three-electrode system (RE, WE, and CE) with LMO modification on WE.

3.2.3 Dimension Assessment

All dimensional measurements were performed using the Keyence VHX-970F Digital Microscope (Keyence, Mississauga, Canada). The length and width of the printed lines were measured using the built-in parallel measurement tool. This function allowed for accurate horizontal distance analysis between the edges of the printed features directly from high-resolution optical micrographs.

To measure the thickness (or height) of the printed layer, the microscope's fine-depth composition mode was employed. This process involved manually adjusting the Z-stage to focus on two reference planes:

1. Top Surface – the highest point of the printed line, brought into sharp focus and set as the upper Z-limit.
2. Bottom Surface – the Surface of the underlying PI film (unprinted area), set as the lower Z-limit.

Once these two focal planes were defined, the system captured a stack of images between them. These images were used to reconstruct a 3D surface profile of the printed feature. The thickness of the printed layer was then determined by calculating the vertical distance between the maximum and minimum points on the 3D profile.

3.2.4 Electrochemical Characterization and Data Analysis

CV measurements were performed using the fabricated three-electrode system immersed in 20 mL of analyte solution in a beaker as shown in Figure 1a (iv). The experiments were conducted at

room temperature with an Autolab potentiostat (Utrecht, Netherlands) controlled by Nova 2.1 software. The potential was swept from -0.8 V to 1.2 V at different scan rates. This potential window was selected to accurately capture the reduction peak potential for lithium detection. While previous studies have typically used a narrower range of -0.2 V to 1.2 V for lithium detection [7], our extended range ensures precise detection of any subtle potential variations induced by LMO modification changes. Each experiment consisted of three consecutive scans, and the average was used for analysis. The reduction peak currents for all the CV scans were determined by identifying the minimum (cathodic) currents, where the peaks were observed in the scan plots, ensuring consistency. Data processing and graph generation were performed using Origin 2024b software.

3.3 Results

3.3.1 CV Analysis for Lithium Detection Using Untreated and Plasma-Treated Bare LIG Electrodes

We started by testing a three-electrode system made from LIG to see if it could detect lithium without any extra functionalization. Two types of electrodes were tested: untreated LIG and plasma- treated LIG, with the latter treated for 50 seconds — the optimized condition identified in Chapter 2 for improved electrochemical performance. As shown in Figure 3.2, the CV results showed no apparent oxidation or reduction peaks for lithium. However, the plasma-treated electrode demonstrated a higher current response than the untreated one, consistent with the enhanced sensor performance observed in Chapter 2.

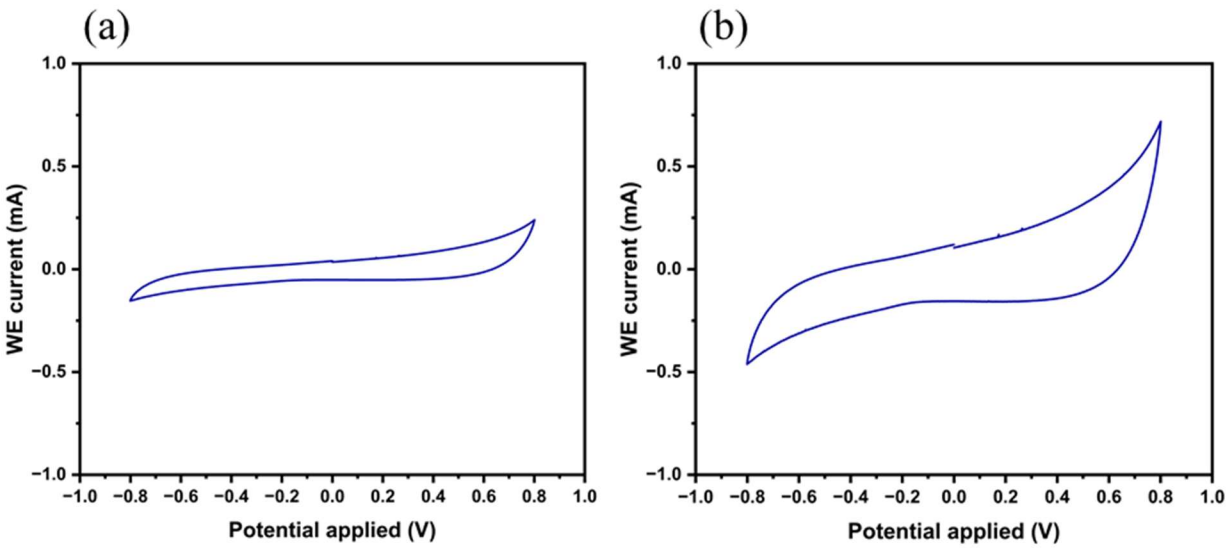

Figure 3.2. CV analysis of 1 M LiCl solution for lithium detection. (a) CV response using a three-electrode system fabricated without plasma treatment or additional functionalization. (b) CV response using a three-electrode system fabricated with 50 seconds of plasma treatment, without further functionalization.

3.3.2 Optimization of LMO Printing via Linear Plunger Displacement of Dispensing Plunger

Since the bare LIG electrodes—untreated and plasma-treated—could not detect lithium in the analyte solution, LMO functionalization became essential. The WE was modified to improve lithium sensitivity by depositing a layer of LMO using dispense printing. Linear displacement of the dispensing plunger is an important parameter of dispense printing, which is defined as the straight-line movement of the dispensing plunger, as shown in Figure 3.1a (iii). This displacement directly controls the volume of ink extruded and determines the pressure applied to the ink reservoir in dispense printing. As a result, it affects the printed material's thickness, uniformity, and spread. The LMO ink was first extruded in our printing process by advancing the plunger based on a predefined linear displacement value. Once the initial deposition was made, the nozzle

moved across the substrate in a straight line to spread the ink. At the end of the motion, the plunger was actuated again to release additional ink, after which the nozzle returned to its starting position. This sequence ensured consistent ink deposition and helped to achieve a uniform coating. Figure 3.3a presents the optical micrograph used to determine the width and length of the LMO layer printed on a PI film.

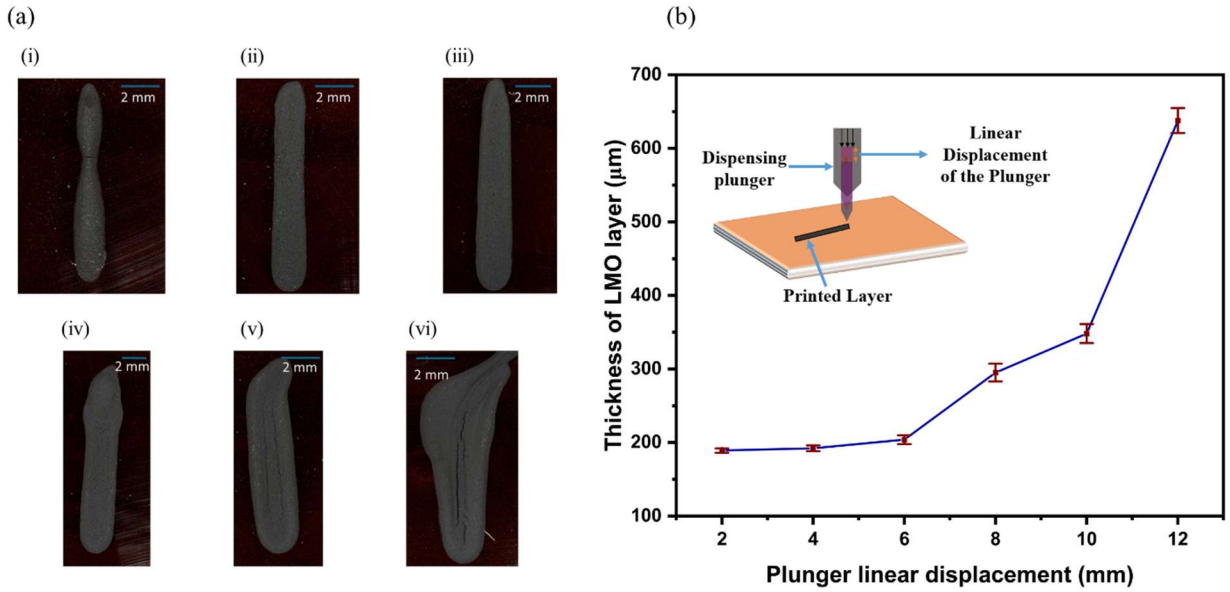

Figure 3.3. Evaluation of the effect of plunger linear displacement on the uniformity and continuity of the printed LMO layer. (a) Optical micrographs of the LMO patterns printed on PI film at plunger displacements of: (i) 2 mm, (ii) 4 mm, (iii) 6 mm, (iv) 8 mm, (v) 10 mm, and (vi) 12 mm, to identify the most suitable setting for achieving a consistent and uniform printed layer. (b) Variation in the thickness of the printed LMO layer at different linear displacements of the dispensing plunger. (Inset: Schematic illustration showing the concept of linear displacement during dispensing.)

The micrographs demonstrate that increasing the linear displacement of the dispensing plunger led to distortion in the printed LMO layer. At the lowest linear displacement of 2 mm, the printed line was narrow (average width ≈ 1.14 mm) (Figure 3.3a (i)). It showed discontinuities in the middle

and non-uniform thickness, making it unsuitable as the optimal setting. Increasing the displacement to 4 mm (Figure 3.3a (ii)) resulted in the most uniform and continuous print, with an average width of 1.42 mm (±0.11 mm), closely aligning with the target WE width. The layer showed thickness uniformity, minimal edge waviness, and no visible cracks, making this setting optimal.

Further increases in displacement led to progressively poor print quality. At 6 mm (Figure 3.3a (iii)), the line became overly broad (1.93 mm ± 0.13 mm), slightly overfilling the desired area. Displacements of 8 mm and higher (Figure 3.3a (iv–vi)) introduced significant distortions, such as irregular edges, non-uniform thickness across the length, and increased cracking. The cracks in the electrode surfaces were especially prominent at 12 mm (Figure 3.3a (vi)), where material assembly at the edges and internal cracks were visible. Edge waviness was also notable at these higher displacements, indicating an over-deposition of material. Based on these assessments, 4 mm was picked as the optimal setting for LMO printing.

Figure 3.3b presents the thickness variation of the printed LMO layer as a function of plunger linear displacement, with an inset schematic illustrating the dispensing process and the concept of plunger linear displacement. Based on the dimensional assessments, a linear plunger displacement of 4 mm was identified as the optimized setting, yielding dimensions closest to the target values. Correspondingly, the measured thickness at 4 mm displacement was 192.13 (±4) µm**.** For 2 mm and 6 mm plunger displacements, the thicknesses were 189.07 (±3) µm and 203.83 (±5) µm**,** respectively—both relatively close to that of the 4 mm linear displacement. However, combining

the dimensional measurements and thickness values, the 4 mm displacement provided the most accurate and consistent results, making it the optimized choice among these settings.

At higher plunger displacements, the printed layer thickness increased significantly. As the plunger displacement increased to 8 mm**,** 10 mm, and 12 mm, the thickness of the printed LMO layer increased substantially, reaching, 295.05 (±3) µm, 348.08 (±13) µm, and 637.77 (±17) µm respectively. This increasing trend of thickness shows that at higher plunger displacements, excessive material is deposed, which leads to significantly thicker layers and reduced control over the printed feature dimensions.

3.3.3 Curing Temperature Optimization for Printed LMO

One of the key factors in printing conductive inks is the temperature used during the curing process after printing. This step is important because proper curing helps the LMO layer reach its best possible conductivity. We tested different curing temperatures, all for 30 minutes, once the LMO ink was printed to find the most suitable condition. As shown in Figure 3.4, curing the printed LMO layer at 120 °C for 30 minutes resulted in the best electrical performance, with a sheet resistance of 110.89 ± 2.56 Ω/sq.

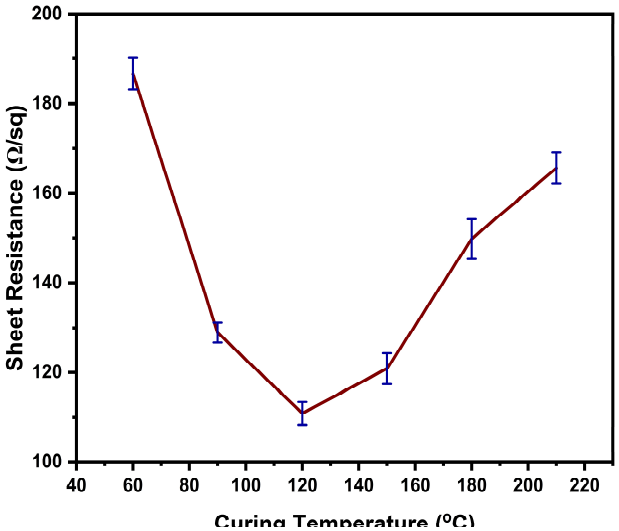

Figure 3.4. Variation of sheet resistance of the printed LMO layer as a function of curing temperature.

In comparison, lower curing temperatures of 60 °C and 90 °C led to significantly higher sheet resistances of 186.67 (± 3.45) Ω/sq and 128.92 (± 2.56) Ω/sq, respectively. When the curing temperature was raised above 120 °C to 150 °C, 180 °C and 210 °C, the conductivity decreased, as reflected by a rise in sheet resistance to 120.89 ± 3.45 Ω/sq, 149.79 ± 4.27 Ω/sq, and 165.68 ± 3.49 Ω/sq, respectively. This was likely due to damage or changes in the structure of the printed LMO layer caused by the higher heat. This outcome aligns with previous research, suggesting that the conductive nanoparticles remain surrounded by residual solvents and organic binders during the initial curing phase. These materials act as insulating barriers, preventing the formation of effective conductive pathways. As the curing process continues, the solvent content gradually decreases through evaporation, allowing the nanoparticles to come into closer contact and form continuous networks that support electron flow. However, when the curing temperature exceeds an optimal level, the structure of the printed layer may degrade, leading to increased

resistance and reduced conductivity [117], [109]. Based on these observations, a curing condition of 120 °C for 30 minutes was selected as the most suitable for achieving reliable electrical performance.

3.3.4 CV Response of LMO-LIG Electrodes and Its Selective Detection Towards Li^+ Ions

We first measured the CV response of a three-electrode system incorporating an LMO-modified WE in a 1 M LiCl solution to evaluate the electrochemical detection capability for Li-ions. We also ran CV tests with 1 M KCl, 1 M NaCl, and DI water as control solutions to check if the response was specifically due to lithium ions. The results from these tests are shown in Figure 3.5.

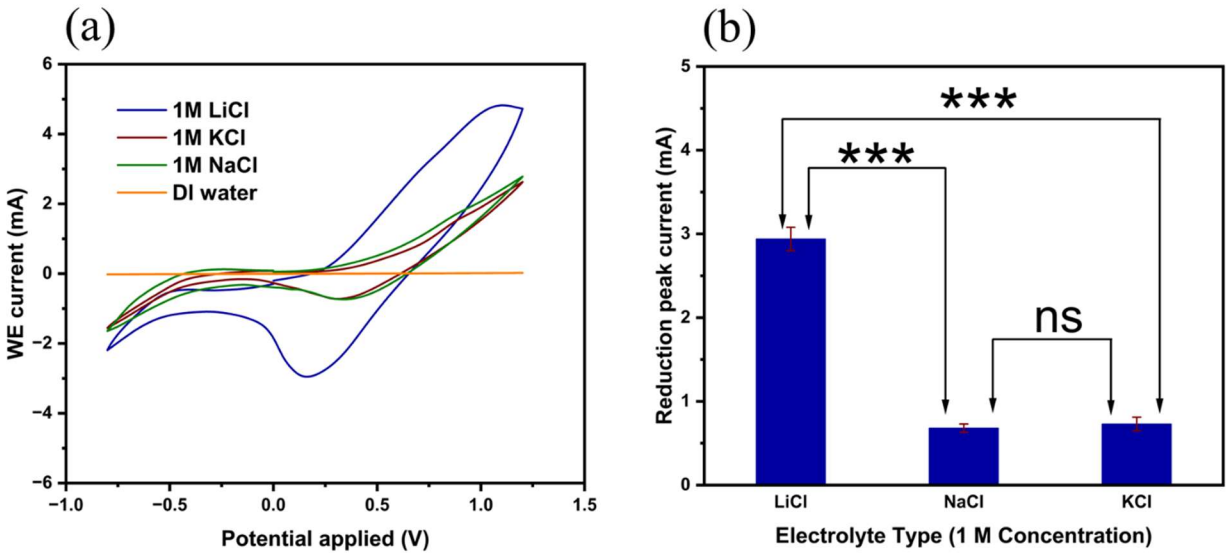

Figure 3.5. CV analysis of the LMO-modified WE for selective detection of lithium ions. (a) CV response of the three-electrode system using different analyte salts (LiCl, NaCl, KCl, and DI water) at 1 M concentration. (b) Difference in reduction peak current values between the analytes, with statistical analysis showing significant differences between LiCl and NaCl ($p = 0.0008$) and between LiCl and KCl ($p = 0.00093$), while no significant difference was observed between NaCl and KCl ($p = 0.12$). Statistical significance is denoted as follows: $p < 0.05$ (*), $p < 0.01$ (**), and $p < 0.001$ (***).

When tested with 1 M LiCl, the LMO-modified electrode showed a clear and strong reduction peak due to the lithiation in the WE, with a current of –2.95 ± 0.17 mA at a potential of 0.16 ± 0.04 V (Figure 3.5a). In contrast, no such peak was observed for the bare LIG electrodes, either with or without plasma treatment, further confirming the effectiveness of LMO modification in enabling lithium detection. Compared to LiCl, much smaller peak currents were recorded for 1 M KCl and NaCl. For KCl, the reduction peak was –0.71 ± 0.097 mA at 0.352 ± 0.021 V, and for NaCl, it was –0.71 ± 0.083 mA at 0.36 ± 0.032 V. The noticeably higher reduction current observed with LiCl indicates that Li^+ ions insert more efficiently into the electrode material compared to Na^+ and K^+ ions. This suggests selective electrochemical response of the sensors toward Li^+. Additionally, the reduction peak potentials for Na^+ and K^+ were similar to each other and appeared slightly earlier than that of Li^+.

3.3.5 Effect of Scan Rate on the CV Response of LMO-LIG Electrodes

To investigate the effect of scan rate on the CV response of LMO-LIG electrodes using a 1 M LiCl solution, five different scan rates were examined, and the corresponding CV responses were recorded. Figure 3.6 presents the resulting CV curves.

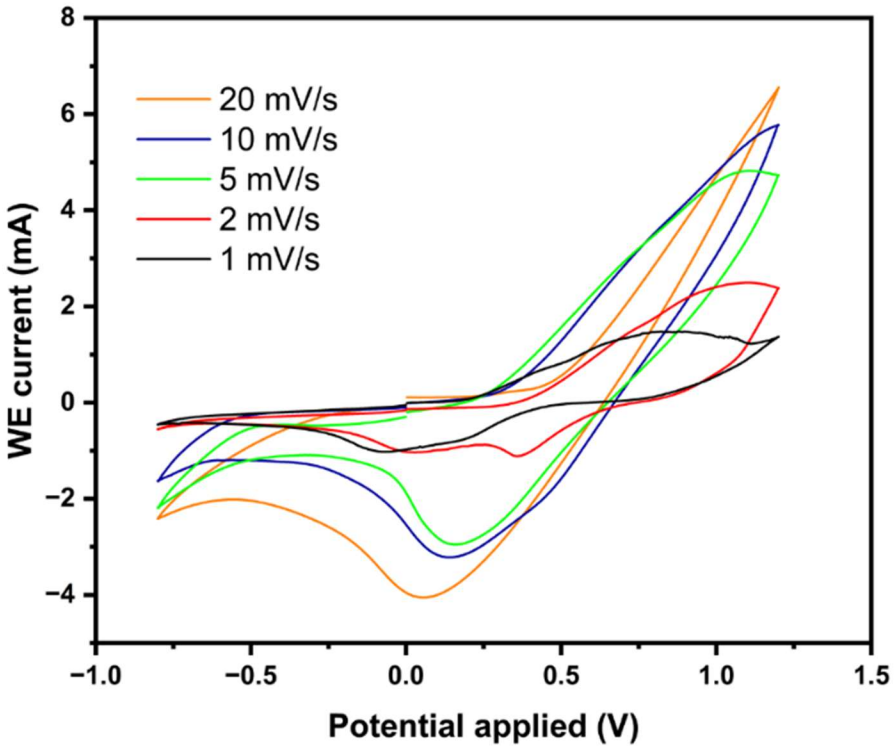

Figure 3.6. CV responses of 1 M LiCl solution at various scan rates, illustrating the effect of scan rate on electrochemical behavior of LIG-LMO electrodes.

The results indicate that scan rate plays a crucial role in influencing both the shape and magnitude of the CV curves. When the scan rate is low (1-5 mV/s), the CV response showed a quasi-reversible manner with a likely symmetric manner between the oxidation and reduction processes. Both the oxidation and reduction peaks were visible in the CV curves at these scan rates, though the oxidation peak appears weaker and less distinct than the reduction peak [118].

On the other hand, when the voltage was swept at a higher scan rate (10 and 20 mV/s), the current response increased, but the oxidation peaks gradually became poorly defined. A higher scan rate can cause this decrease in oxidation peak clarity, the CV process becoming irreversible due to

kinetic limitations and the reduced time available for the system to reach electrochemical equilibrium [119]. Additionally, the higher current value as a function of increased scan rate indicates the higher contribution of capacitive response (non-Faradaic), which can hinder the redox features. The broadening of the CV curves at these scan rates (10 mV/s and 20 mV/s) further supports the idea that redox becomes less reversible. As the diffusion layer becomes thinner at higher scan rates, higher current values are observed. Based on the results, 5 mV/s was chosen as the scan rate for further tests. It showed clear, quasi-reversible peaks and was also suitable considering the total testing time.3.3.6 CV Comparison of LMO-LIG and Bare LMO WE

To evaluate the effect of LMO modification of LIG based WE on the CV response, we tested two sets of devices. One set had bare LMO as the WE, while the other employed LMO-modified LIG as the WE. Figure 3.7 presents the CV responses obtained from both groups.

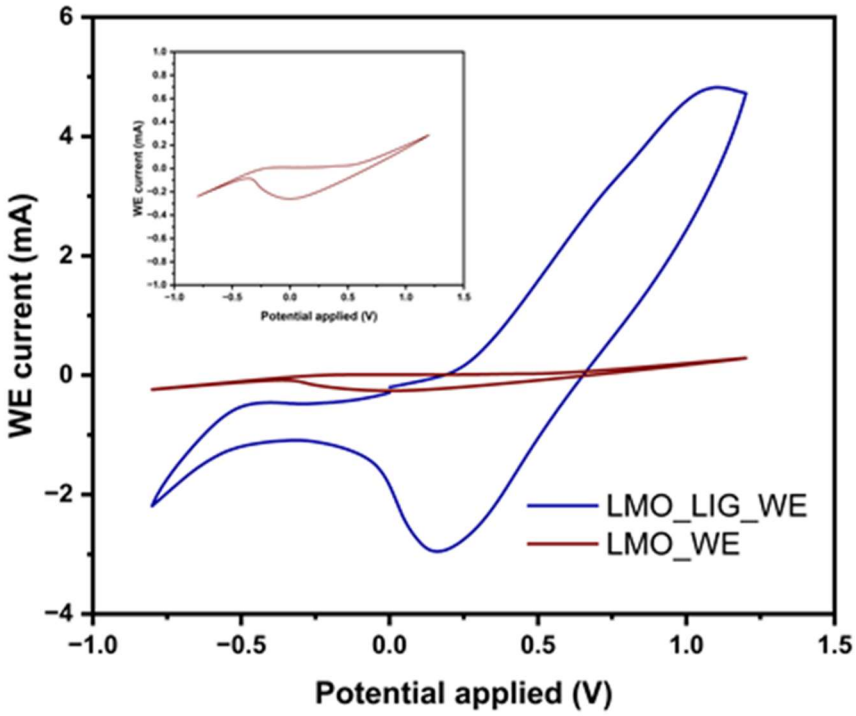

Figure 3.7. Comparison of CV responses between LMO-modified LIG electrodes and electrodes with only an LMO layer as the WE. The inset shows a magnified view of the CV response for the electrode with only the LMO layer, illustrating the comparatively lower current response.

The CV curves depict that when the LMO layer is dispense-printed onto a LIG-based working electrode, the electrochemical performance is significantly enhanced compared to a WE composed of only the LMO layer. Specifically, the LMO-LIG-based WE yields a reduction current of –2.95 ± 0.17 mA at a reduction potential of 0.16 ± 0.04 V. In contrast, the electrode with only the LMO layer yields a much lower reduction current of –0.26 ± 0.06 mA at –0.03 ± 0.01 V. This comparison shows that modifying the LIG based WE with LMO notably improves conductivity, resulting in a higher CV current.

The measured sheet resistance further explains the difference above, i.e., the electrode with only the LMO layer exhibited a resistance of $110.89 \pm 2.56\ \Omega$/sq, while the LMO-modified LIG electrode showed a much lower resistance of $16.78 \pm 1.89\ \Omega$/sq. Although this value is still higher than that of bare LIG ($6.32 \pm 0.38\ \Omega$/sq), it represents a substantial improvement compared to the LMO-only electrode. These results indicate that while the addition of LMO slightly reduces the conductivity relative to bare LIG, the integration with LIG significantly enhances the overall conductivity compared to using LMO alone. This improvement in conductivity contributes to the higher CV current observed during testing with 1 M LiCl solution. Notably, the RE and CE remained the same (LIG-based) in both setups, further confirming that the improvement arises from the enhanced WE configuration.

3.3.7 Interference CV Response of LMO-LIG Electrodes

To examine the selectivity of the LMO-modified LIG electrodes towards Li detection, a series of CV measurements were studied in the presence of potentially interfering ions such as Na^+ and K^+. First, a duplex study was performed using a mixture of 1 M LiCl and 1 M NaCl to see how the presence of Na^+ affects the Li^+ signal. Another duplex test was carried out with 1 M LiCl and 1 M KCl to study the effect of K^+. Next, a triplex study was done using the mixture of all three salts at 1M concentration to observe the electrode's performance in a more complex mixture containing all three ions. Lastly, a mixture of 1 M NaCl and 1 M KCl (without LiCl) was tested to see how the electrode responds when Li^+ is absent, which helps to check if Na^+ and K^+ alone cause any signal close to what we got for Li^+. The CV results from all these tests are shown in Figure 3.8.

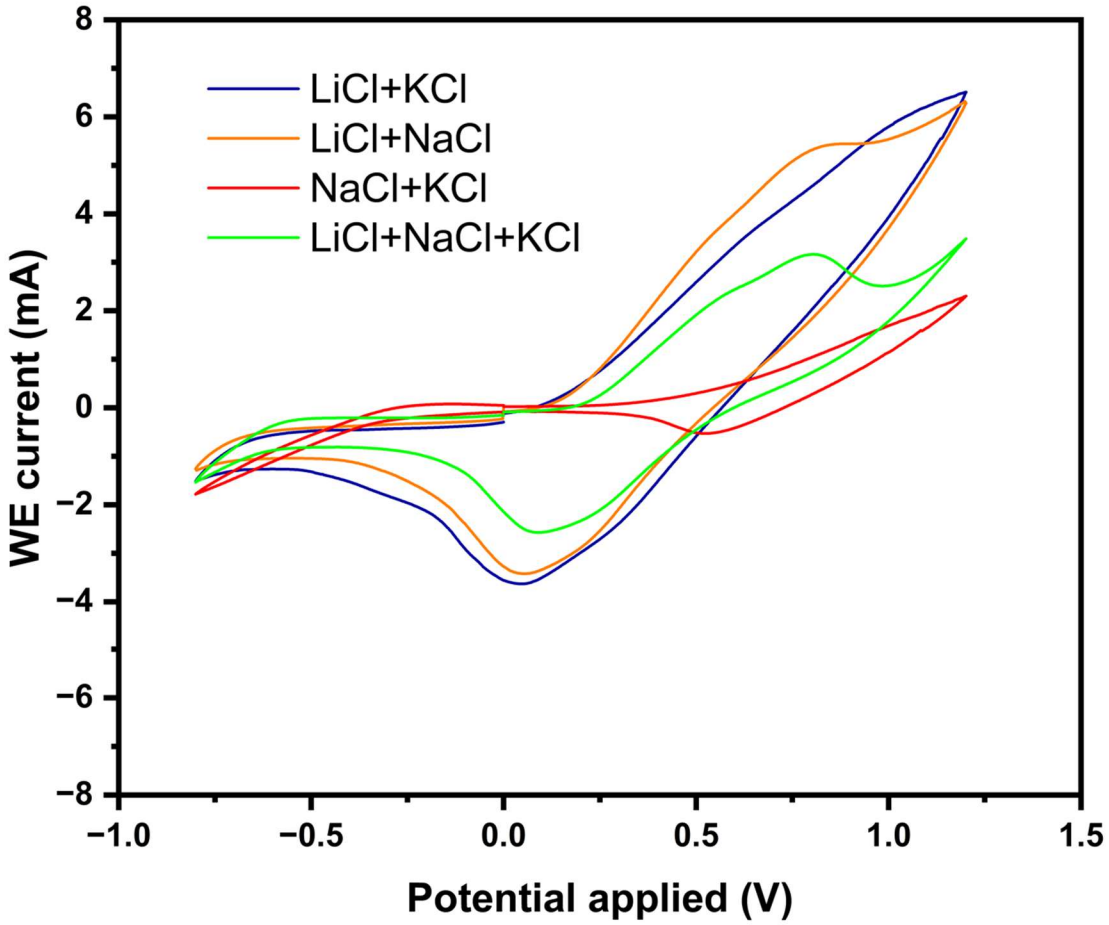

Figure 3.8. CV responses of the LMO-modified LIG electrode in different ionic mixtures. Duplex studies were performed using 1 M LiCl with 1 M NaCl, 1 M LiCl with 1 M KCl, and 1 M NaCl with 1 M KCl. A triplex study was also conducted using a mixture of 1 M LiCl, 1 M NaCl, and 1 M KCl.

The CV results show that when 1 M LiCl was present in the analyte solution—whether in a duplex or triplex mixture—a clear and noticeable reduction peak appeared around 0.15 V. This peak indicates that Li^+ ions were successfully inserted into the LMO-modified electrode. However, the overall CV current was lower in the triplex mixture, where LiCl was mixed with NaCl and KCl. This lower current could be explained by the large number of different ions in the solution, which

might have made it harder for Li^+ to reach the electrode surface and interact with the electrode surface. In contrast, a poor reduction peak appeared when the solution did not include any LiCl and had only NaCl and KCl. This confirms that the electrode does not show the same electrochemical activity without Li^+ meaning no Li^+ was inserted.

These results suggest that the LMO-modified electrode can selectively detect Li^+ even when similar ions like Na^+ and K^+ are present. The system responds only when Li^+ is in the solution, showing reasonable selectivity in mixed-ion environments.

3.3.8 Determination of the LOD, LOQ and sensitivity of the LMO-LIG Electrodes

To determine the LOD of the device with an LMO-LIG based WE, CV responses were recorded for varying concentrations of LiCl analyte solutions. The reduction peak current was extracted from each CV curve by identifying the minimum current within the voltage range of -0.3 V to 0.3 V, as all prominent reduction peaks were observed within this potential window. Clear reduction peaks were not appropriately distinguishable in the CV curves for the lower concentrations, such as 0.001 M, 0.0005 M, and DI water. In this case, the lowest current within the same voltage range (-0.3 V to 0.3 V) was still the representative reduction current for consistency. These values were then plotted against the concentrations of LiCl to evaluate the sensor's response. A linear regression over the widest possible LiCl concentration range was performed to identify the linear region of the dose-response curve, which was subsequently used to calculate the sensor's LOD. The results of the CV responses, along with the dose-response curve and the linear region with the highest R^2 value, are plotted in Figure 3.9.

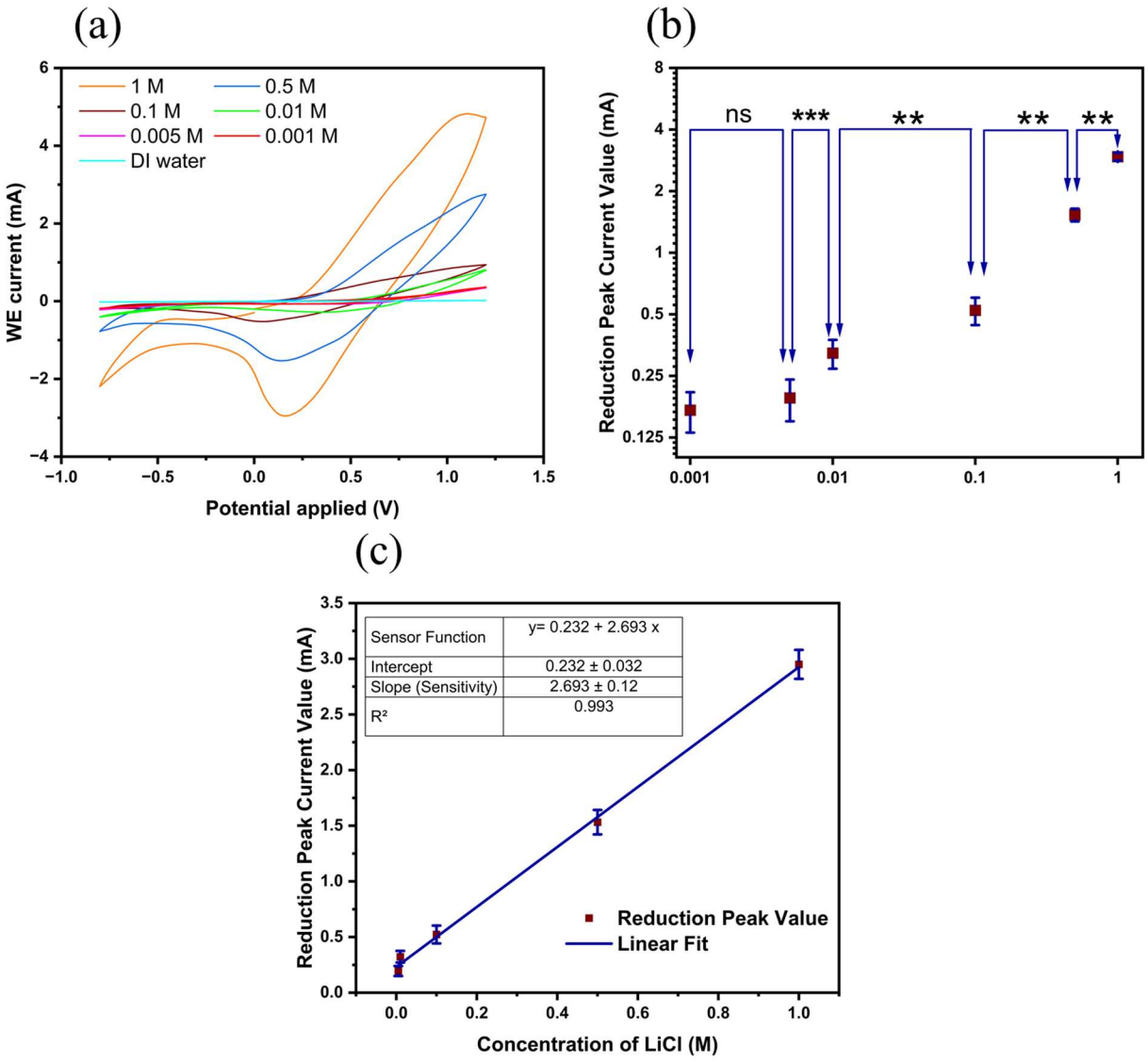

Figure 3.9: (a) *CV responses of LMO_LIG devices as a function of varying concentrations of LiCl, showing the electrochemical behavior across the concentration range.* (b) *Reduction peak current for different LiCl concentrations to generate the device's dose-response curve along with the t-test result. T-test analysis confirms significant differences between most concentrations, with no statistical difference between 0.001 M and 0.005 M.* **(c)** *(c) Linear regression analysis performed for concentrations between 0.005 M and 1 M. The sensor function* y=0.232+2.693x *was derived with a slope representing sensitivity (2.693 mA/M), and a coefficient of determination (R^2) of 0.993, indicating excellent linearity.*

The results in Figure 3.9a indicate that the CV current becomes more prominent with the higher LiCl concentration, with a more substantial reduction peak at higher concentrations. In contrast, the overall CV current and the reduction peak current gradually decrease at lower concentrations. A distinguishable reduction peak was observed only down to a concentration of 0.01 M (10 mM); below this threshold, the Li^+ reduction peak became indistinct and hard to detect.

The corresponding dose-response curve shown in Figure 3.9b also supports this observation. While the concentrations were 0.005 M and 0.001 M, the reduction peak current was either too small to be reliably measured or indistinguishable from the background. This is consistent with the t-test analysis, which revealed no statistically significant difference between the reduction currents at these two concentrations. In contrast, significant differences in current were observed at concentrations above this range, where clearly defined reduction peaks became more prominent. A linear regression analysis was performed to assess the sensor's performance further. The linear fit shown in Figure 3.9c shows that in the concentration range of (0.005 M-1 M), the dose response curve showed excellent linearity with a R^2 value of 0.993. The sensor function in this range was determined to be y=0.232+2.693x.

The linear region's y-intercept and slope were used to calculate the LOD, following the method described in Section 3.4. The LOB was determined to be 0.192 mA, calculated using a blank mean current of 0.161 mA and a SD of 0.019 mA. The LOD current was calculated as 0.262 mA, based on the standard deviation of a low-concentration sample (0.001 M) (SD = 0.042 mA). Finally, using the slope and y-intercept obtained from the linear region, the LOD in terms of concentration was calculated using equation (3) to be 0.0108 M (10.8 mM). The LOQ, which measures the lowest

concentration of analyte where it can be quantitatively detected with acceptable precision and accuracy, is calculated using equation (4) to be 0.155M (155 mM). The sensitivity of the sensor was 2.693 mA/M, as defined by the slope of sensor function.

3.4 Discussion

Developing a Li^+ sensor using LIG and a dispense-printing technique for functionalizing the WE of the LIG system presents a significant development in cost-effective and scalable electrochemical sensing. LMO was chosen to functionalize the WE of the three-electrode system due to its excellent electrochemical selectivity toward Li^+. In electrochemical sensing, such selectivity is essential for achieving selective and accurate detection, making LMO a highly suitable material for this application. [7] . Two WE configurations were tested for Li^+ detection: (1) LMO printed directly on PI and (2) LMO printed on LIG. The comparison of CV results from both groups demonstrated that the integration of LIG with LMO significantly enhanced the sensor's performance. This improvement is due to LIG's role in facilitating electron mobility and having a high surface area [47]. Further experiments were done with this configuration. Additionally, the scan rate was optimized as 5 mV/s because this scan rate balances the detection time with the emergence of a quasi-reversible CV response.

Moreover, the ion interference study provided strong evidence for the selectivity of the LMO-LIG-based electrode toward Li^+. Unlike Na^+ and K^+, which produced minimal currents and separate peak potentials, Li^+ generated a pronounced reduction peak, affirming the selective detection of the lithium. The LMO-modified working electrode exhibits strong selectivity toward Li^+ ions, resulting in significantly greater lithium insertion compared to the interfering ions Na^+ and K^+.

Consequently, the reduction current observed for Li^+ is substantially higher. [120]. This characteristic is significant for applications such as medical diagnostics or groundwater monitoring, where competing ions are familiar.

While the LOD and LOQ of our sensor, 10.8 mM and 155 mM respectively, are not among the lowest compared to some reports in the literature [7], the results still show great promise for using LIG in Li^+ detection. For example, although the sensor in [7] achieved a lower LOD, it required a non-portable setup involving GCE modified with LMO. Similarly, lithium sensors employing materials like $LiFePO_4$ have reported electrode synthesis times nearing 20 hours [121]. In contrast, our sensor offers significant advantages in fabrication simplicity and speed, requiring only approximately 45 minutes without complex or prolonged processing steps. Moreover, the device design eliminates the need for additional conditioning equipment, enhancing its portability and field applicability. Compared to existing electrochemical lithium sensors, which often demand 10–12 times longer fabrication periods and involve intricate material processing, our approach achieves a strong trade-off between performance, scalability, and ease of deployment.

Because of this simplicity, our sensor is suitable for real-time and on-site testing, especially in cases where very low detection limits are not necessary in industrial applications such as lithium extraction and environmental monitoring. It also shows good selectivity for Li^+, even in the presence of other ions like Na^+ and K^+. This highlights the feasibility of our sensor and supports the potential of LIG as a reliable platform for lithium-ion sensing.

3.5. Conclusion

In this study, we present a cost-effective and easy-to-fabricate lithium sensor using LIG functionalized with a dispense-printing approach. Lithium detection is essential for various applications, including resource recovery, medical diagnostics, and groundwater monitoring. Although LIG is user-friendly and has high conductivity, its potential for lithium detection has not been explored to date. To address this, we applied a simple functionalization of LIG with an LMO layer, which was selected for its affinity towards Li^+ to modify the WE. The optimized dispense-printing conditions enabled a uniform and consistent deposition of the LMO layer onto the LIG working electrode, while the selected curing temperature ensured both high conductivity and proper material stabilization. The resulting sensor exhibits strong selectivity toward Li^+, producing a reduction current nearly four times higher than that of Na^+ and K^+ ions. Additionally, the reduction peaks were clearly distinguishable based on their potential values, reinforcing the effectiveness for lithium detection.

Interference studies confirmed the device's ability to selectively detect lithium in the presence of competing ions, highlighting the effective performance of the LIG-modified electrode system. These findings form the basis for a promising sensing platform, where LIG is integrated for lithium detection for the first time. While the sensor’s sensitivity, LOD, and LOQ are promising, they demonstrate the potential of this platform for practical applications. Moving forward, further optimization in the patterning and functionalization of LIG could unlock enhanced sensing performance and deeper insights into its role in lithium detection.

4 3D-Printed Microfluidic Electrochemical Sensor with Laser-Induced Graphene Electrodes and Printed Functionalization for Lithium Sensing

4.1 Introduction

Electrochemical sensors have gained significant research interest as powerful sensing tools for real-time, sensitive, and selective detection. The efficiency of these sensors can be enhanced when integrated with microfluidic systems like channels or chambers. This integration of the sensing platform with an electrochemical sensor offers controlled fluid handling, rapid response, and reduced reagent consumption [122]. Another prime advantage of this combination is the ability to manipulate small fluid volumes precisely, ensuring consistent interaction between the analyte and the sensing electrode [123]. Moreover, microfluidic platforms allow for faster mass transport of analytes to the electrode surface, improving the sensor's sensitivity and response time.

Recent studies demonstrated the integration of microfluidics with electrochemical sensors using PDMS microchannels coupled to a glass/silicon substrate with patterned electrodes. In this case, electrodes are patterned separately, using photolithographic processes and metal or carbon deposition on the substrates. However, these fabrication techniques involve multiple complex steps, including cleanroom processes and preparing photolithography masks. Such procedures increase both the time and cost of production and may limit accessibility for rapid or iterative prototyping [124]. The overall complexity of the process presents a significant barrier to scalable, low-cost sensor development. Because of these limitations, moving from lab-scale fabrication to industrial use can be challenging [9]. In contrast, additive manufacturing provides a more affordable and customizable approach, making it well-suited for scalable fabrication without the

need for extensive infrastructure. Specifically, 3D printing enables the fabrication of structural components and microfluidic sensing platforms, while LIG allows for the direct conversion of 3D-printed polymers into conductive electrodes [78]. Additionally, dispense printing can be used for electrode functionalization (e.g., with LMO), allowing sensors to be precisely customized for specific detection applications like lithium sensing. As demonstrated in the previous chapter, LMO-modified LIG electrodes showed promising feasibility for selective lithium sensing, highlighting the potential of this approach for targeted electrochemical applications with functionalized LIG.

In this study, we are leveraging the benefits of additive manufacturing to develop a novel 3D-printed microfluidic electrochemical sensor using a PEI-based filament featuring LIG-based electrodes functionalized with LMO for lithium detection. Combining microfluidics, LIG electrodes, and electrode functionalization using dispense printing makes this platform a miniature, substantial, highly selective sensor perfect for advanced electrochemical use.

4.2 Methods

4.2.1 Device Fabrication

This fabrication of the device underwent through 4 steps:

Substrate Fabrication: The process began with the fabrication of the substrate using PEI filament (3D Printing Canada, Hamilton, Canada) with a Hyrel 3D printer. The substrate was designed in SolidWorks 2023 and was sliced using Ultimaker Cura 5.4 (Figure 4.1a). The substrate design included an alignment notch for accurate positioning during subsequent steps. The design and

dimensions of the substrate are shown in Figure 4.1a. To improve the surface quality, the top layer of the substrate was ironed in-situ immediately after printing. This step significantly reduced surface roughness, as detailed in earlier study on FDM surface ironing. The FDM printing and ironing settings, listed in Table 4.1, to achieve the lowest possible surface roughness to fabricate the LIG electrodes on it. The final printed substrate is shown in Figure 4.1b.

Table 4-1 FDM printing parameters

Printing parameter	Value
Nozzle Size	0.4 [mm]
Layer Height	0.2 [mm]
Top/Bottom Layer Thickness	0.8 [mm]
Top Layers	1
Bottom Layers	1
All Patterns	Zig Zag
Top/Bottom Line Direction	0
Ironing Line Spacing	0.05 [mm]
Ironing Flow	50 [%]
Ironing Speed	60 [mm/s]
Infill Density	100 [%]
Flow	100 [%]
Printing Temperature	370 [ºC]
Build Plate Temperature	170 [ºC]

LIG Electrode Patterning: Three electrodes (WE, CE, and RE) were patterned directly onto the 3D-printed PEI substrate using a 40 W CO_2 laser. The LIG patterning was done with 17% laser power and a scan speed of 120 mm/min, as illustrated in Figure 4.1c and detailed in Section 2.2.3.

LMO-Functionalized Working Electrode: A uniform LMO layer was printed onto the WE to enable lithium detection. The process ensured consistent printing and functionalization, as shown in Figure 4.1d and discussed in Section 3.2.2.

Microfluidic Channel Integration: A microfluidic channel was designed in SolidWorks for integration on top of the LIG-patterned electrodes (Figure 4.1e) and sliced using Ultimaker Cura 5.4 software (Figure 4.1f). The channel was then 3D-printed directly over the LIG electrodes, forming a compact and integrated sensing platform that enables controlled fluid flow across the active sensing area (Figure 4.1g).

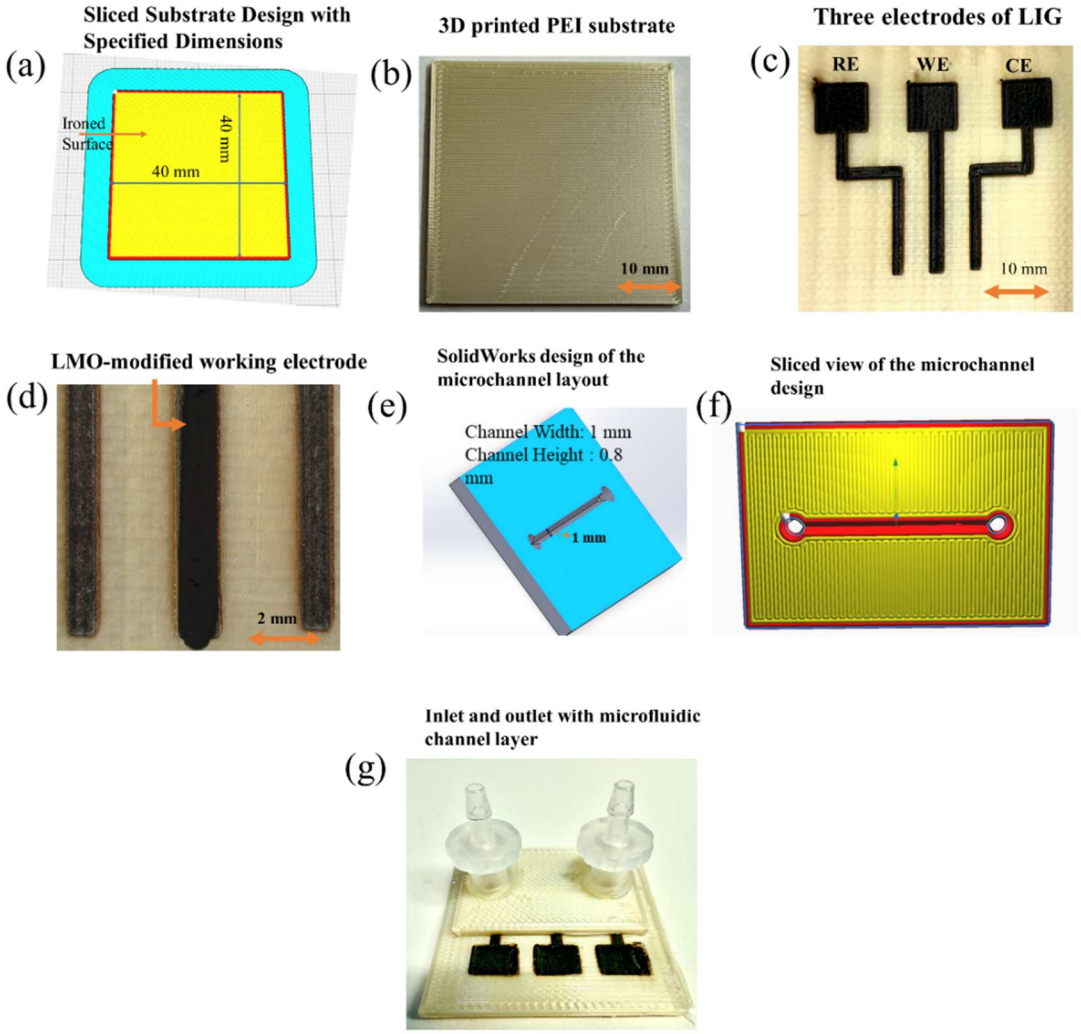

Figure 4.1. Fabrication process of the microfluidic LIG-based electrochemical sensor. (a) Sliced substrate design with specified dimensions prepared in slicing software for 3D printing (b) 3D-printed PEI substrate using FDM technique (c) LIG electrodes formed on the PEI substrate (RE: reference electrode, WE: working electrode, CE: counter electrode). (d) Optical micrograph showing the LMO-modified working electrode. (e) SolidWorks design of the microchannel layout with specified channel width and height. (f) Sliced view of the microchannel design showing the internal structure for 3D printing. (g) Final assembly of the device with inlet and outlet ports integrated on the microfluidic channel layer.

4.2.2 Device Characterization

After the complete microfluidic-based device was fabricated, cross-sectional cutting was performed on the microfluidic channels using the Diamond Wire Saw DWS.100 (Diamond Wiretac, Weinheim, Germany). Different microfluidic channel designs were analyzed using the Keyence VHX-970F Digital Microscope (Keyence, Mississauga, Canada).

4.2.3 Electrochemical Testing

Analyte solutions were injected into the microfluidic channel using a single-syringe infusion pump (KDScientific, Holliston, USA) at a 1 mL/min flow rate. CV measurements were carried out to evaluate the sensor's detection capability of lithium ions, as described in Section 3.2.2.

4.2 Results

4.3.1. Dimensional Assessment of Fabricated Microfluidic Channels

To evaluate the post-processing dimensions of two different channel designs, triangular and rectangular, both the channel designs were 3D printed, and then cross-sectional cutting was done using wire cutting to check their stability after printing. The analysis from the optical micrograph is shown in Figure 4.2(a, b).

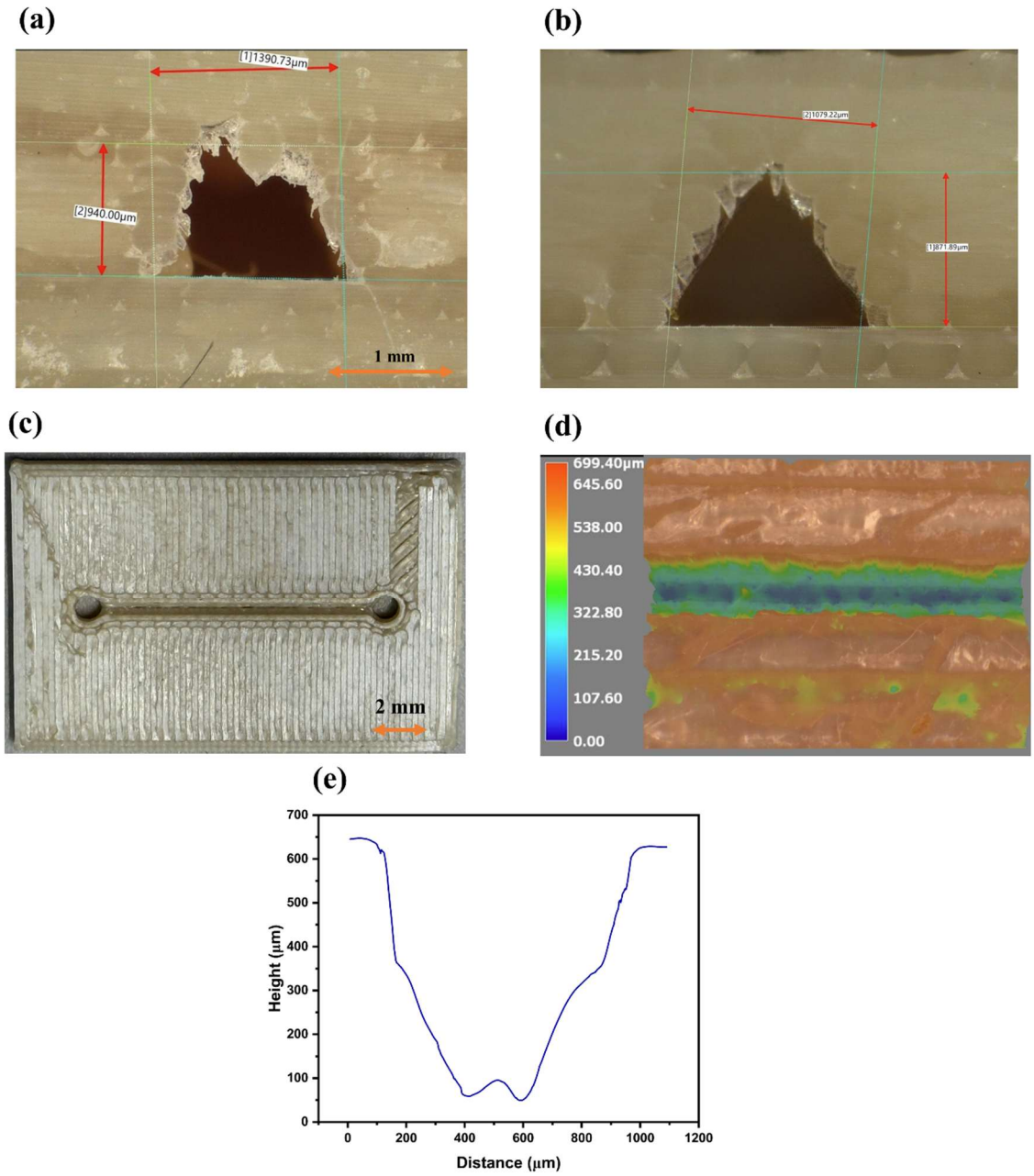

Figure 4.2. Cross-sectional views of (a) rectangular and (b) triangular microfluidic channels, fabricated through 3D printing followed by wire cutting. (c) 3D-printed triangular microfluidic channel fabricated with an open bottom. (d) 3D depth analysis of the channel, illustrating its structural features. (e) profile of the fabricated microfluidic channel, highlighting the channel's dimensions and surface topology.

The result shows that the rectangular channel design after the 3D printing showed structural instability and partially collapsed during fabrication (Figure 4.2a). In the original SolidWorks design, the rectangular microchannel was specified to have both a width and height of 1 mm. However, optical micrograph analysis revealed that the printed channel measured approximately 1.39 (± 0.13) mm in width and 0.94 (± 0.09) mm in height. In contrast, the triangular channel proved more robust and was successfully fabricated without collapsing (Figure 4.2b). The channel was originally designed with a width of 1 mm and a height of 0.8 mm. Post-fabrication measurements using optical microscopy revealed dimensions of approximately 1.08 (± 0.07) mm in width and 0.87 (± 0.09) mm in height, indicating strong structural stability and minimal deviation from the intended design. Based on these findings, the triangular channel was chosen for further dimensional analysis and subsequent electrochemical investigations.

To further check the reliability of the triangular channel design, it was printed without a substrate layer (Figure 4.2c) so that its 3D shape and depth could be directly analyzed. The depth and profile results are shown in Figures 4.2 (d, e). The height was determined by calculating the vertical distance between the starting edge of the dip and its lowest point on the profile curve. Similarly, the width was measured as the horizontal distance between the start and end points of the dip. From the 3D depth map (Figure 4.2d), the channel height was approximately 0.695 mm (± 0.01 mm). The 3D profile (Figure 4.2e) showed a channel height and width of 0.647 mm (± 0.009 mm) and 0.879 mm (± 0.007 mm), respectively. Based on these values, the aspect ratio of the channel was found to be 1.36, which is closely aligned with the aspect ratio obtained from the optical micrograph (1.24) and the original design specification (1.25). These results confirm that

the triangular channel retained its intended geometry post-printing, demonstrating structural stability and accurate depth formation.

4.3.2 Effect of Printing Gap Between the Microchannel Wall and LIG Surface on Electrode Resistance and Device Leakage

To optimize the gap between the patterned LIG electrodes and the first layer of the 3D-printed microfluidic channel wall printed above it, we studied the effect of vertical gap which is the distance between the top surface of the LIG and the bottom surface of the first printed microchannel layer. This gap plays a critical role in determining both the electrical and fluidic performance of the device. If the channel is printed too close without setting any predefined gap value in the settings, it might touch the LIG surface and damage it, which can increase the electrode's resistance. On the other hand, if the gap is too large, fluid can leak through the space, affecting sensing accuracy and device reliability. Therefore, several gap settings were tested to find the condition that maintained strong layer adhesion, prevented fluid leakage, and minimized changes in resistance. Table 4.2 presents the measured resistance values alongside the leakage test results for each configuration.

Table 4-2 Changes in resistance and leakage testing results as a function of the gap between the LIG layer and microfluidic channel.

Gap between LIG and microfluidic channel layer (mm)	Change of Resistance of LIG electrodes	Leakage testing
0.04	2% (±0.57%)	Leakage
0.03	2.2% (±0.32%)	Leakage
0.02	4% (±0.94%)	Leakage
0.01	7% (±1.37%)	No leakage
0.00	59% (±1.75%)	No leakage

When the microfluidic channel is 3D printed without maintaining a gap between the substrate where the LIG is patterned and the first printed layer of the microchannel, the nozzle tip comes into direct contact with the LIG surface. This contact physically disrupts the electrode and significantly increases its resistance, with observed values rising to 57%. As LIG electrodes contain surface roughness and height variation and are not properly blended with the substrate, the nozzle operating at high temperatures can scratch or damage the LIG structure during printing. This mechanical and thermal interference disrupts the continuity of the conductive LIG network, leading to a significant increase in electrode resistance, measured at approximately 57%. For an electrochemical sensor, this disruption is highly undesirable as loss in conductivity can

significantly degrade the sensor's overall performance and sensitivity. As a result, maintaining a proper gap between the substrate and the microchannel is essential to maintain the integrity and conductivity of the LIG electrodes. However, the gap must also be well enough not to provide any leakage at the interface of LIG and microchannel while the fluid is flowing. Leakage from the interface can compromise fluid control. Thus, balancing protecting the LIG surface and ensuring a closed, leak-free microchannel seal is essential for reliable device performance. However, the resistance increase was much less when the gap settings were increased, such as 0.02 mm and more, with 4% for 0.02 mm, 2.2% for 0.03 mm, and 2% for 0.04 mm. However, in all three cases with minimal conductivity change, there was leakage in the connection between the microfluidic and LIG electrode layers. The condition where there is no leakage with minimal change in resistance is a 0.01 mm gap. With this gap, the change in resistance is 7% with no leakage. When this gap is imposed for the printing, the nozzle does not affect the conductivity and has no leakage because with this gap, as the PEI filament is printed, it cools down after printing and blocks the gap between those two layers.

4.3.3 CV Analysis for Assessing Lithium Detection Performance of the Functionalized LIG-Based Microfluidic System

With the optimized settings, the microfluidic channel with inlet and outlet was successfully printed on top of the functionalized LIG electrodes, completing the integrated sensing device. CV analysis was performed using a 1 M LiCl solution injected into the microchannel to evaluate the sensing potential of the LMO-functionalized LIG-based microfluidic sensor. CV responses for 1 M NaCl

and KCl solutions were also recorded to compare and identify any similarities or differences in their electrochemical behavior relative to LiCl. The results are summarized in Figure 4.3.

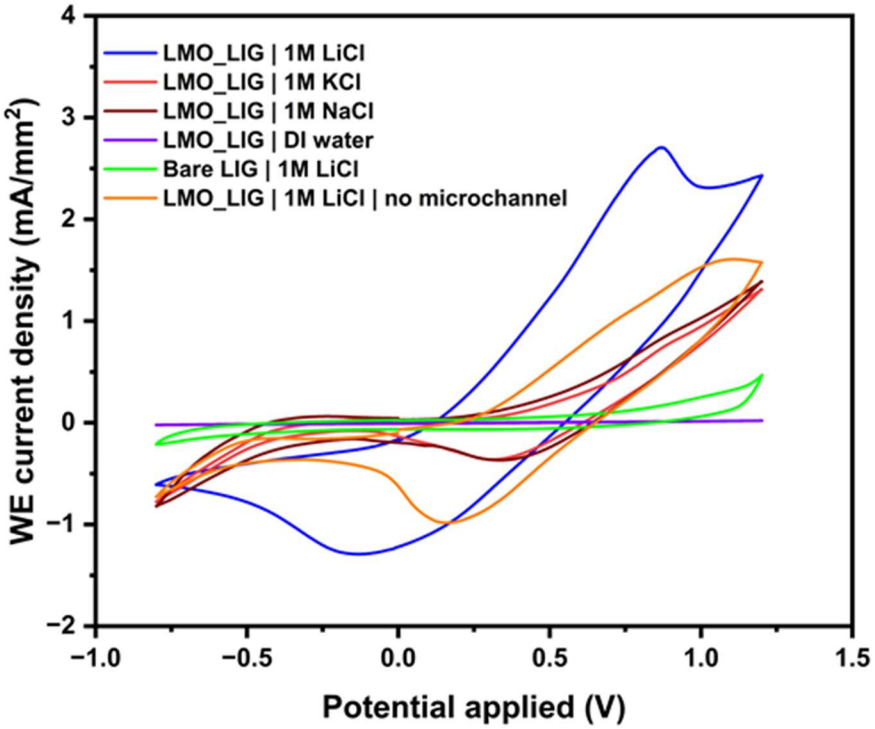

Figure 4.3. CV responses of LMO-modified LIG electrodes in different electrolyte solutions:1 M LiCl, NaCl, KCl, and DI water. Responses from bare LIG in 1 M LiCl and from an LMO_LIG electrode on a PI substrate without the microchannel are also included for comparison. All tests were performed under the same electrochemical conditions.

The results show that while the analyte solution contains LiCl, the LIG-based three-electrode system with no LMO modification did not produce any distinct peak in both case of oxidation and reduction phases. In comparison, devices with LMO-modified LIG-based WE demonstrated apparent oxidation and reduction peaks with the microchannel as the sensing platform. The oxidation peak is around 0.87 (± 0.06) V with a current density of 2.7 (± 0.11) mA/mm^2. Again,

the reduction peak appeared at -0.15 (± 0.04) V with a current of -1.29 (± 0.08) mA/mm^2. The oxidation peak corresponds to the delithiation of Li_2MnO_4 to MnO_4^{2-} on the WE in the presence of the LiCl solution, while the reduction peak represents the reverse process during lithiation [7].

Stronger oxidation and reduction peaks were observed when the functionalized LIG electrodes were integrated with the microfluidic sensing platform, compared to the setup without the microchannel where the LIG was scribed and modified directly on a PI film, as reported in the previous chapter. This improvement highlights the positive impact of microfluidic integration on the electrochemical performance of the sensor. The oxidation peak current density increased from 1.59 mA/mm² (without microchannel) to 2.69 mA/mm² (with microchannel), corresponding to an enhancement of approximately 69.2%. Similarly, the reduction peak current density increased from –0.98 mA/mm² to –1.29 mA/mm², representing an improvement of about 31.6%. These improvements highlight that integrating the microchannel directly on top of the electrodes significantly enhances electrolyte convection toward the electrode surface, resulting in a more efficient electrochemical response enabled by the microfluidic design. On top of that, the addition of a microfluidic sensing platform helps the electrochemical reaction to reach the equilibrium state and perform a reversible electrochemical reaction compared to the one without having it.

CV tests with 1 M KCl did not produce a distinct oxidation peak, showing only a reduction peak of current density of -0.36 ± 0.06 mA/mm^2 at approximately 0.34 ± 0.03 V. In the case of 1 M NaCl, only a weak reduction peak was observed with peak current density of -0.34 ± 0.04 mA/mm^2 near 0.34 ± 0.04 V. These responses were significantly weaker and appeared at different potentials compared to the peaks observed with LiCl, indicating a lack of lithium-specific electrochemical

activity. This further confirms that the LMO_LIG electrodes exhibit strong affinity toward Li^+ ions. With DI water, oxidation, and reduction peaks were absent. The results demonstrate the feasibility of a fully integrated electrochemical sensor with 3D-printed microfluidic channels and LMO-modified LIG-based electrodes.

4.3.4 LOD, LOQ, and Sensitivity Analysis

CV responses were recorded to determine LOD for analyte solutions with varying concentrations of LiCl. The corresponding reduction peak current values were measured and plotted as a function of their respective concentrations, and a dose-response curve was generated. Regression analysis was conducted to obtain the best-fit curve for the function and based on the R^2 value from the linear regression, a linear range was identified. This range was then used to derive the sensor function, which is applied for LOD calculation. The complete set of results, including the dose-response curve and linear regression to show the quality of the fit with the t-test result to show the differences between the responses of CV currents, is presented in Figure 4.4.

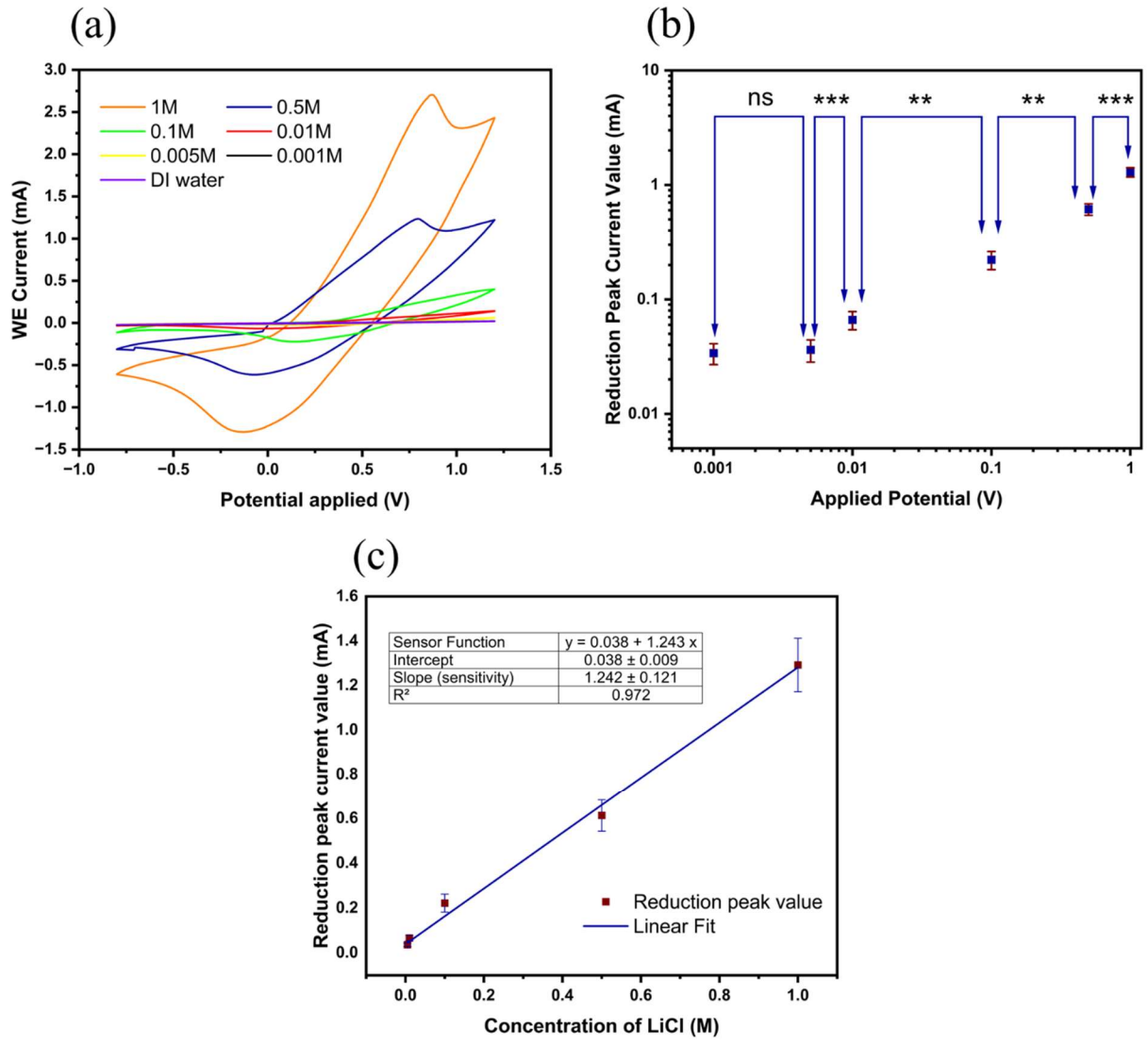

Figure 4.4. *(a) CV responses of LMO_LIG devices integrated with a microfluidic channel, showing the electrochemical behavior across different LiCl concentrations. (b) Reduction peak currents corresponding to various LiCl concentrations, used to generate the device's dose-response curve, along with t-test results indicating statistical differences between concentrations. (c) Linear regression analysis performed on the data from the linear range (0.005–1 M), with the extracted sensor function (slope and y-intercept) used for LOD, LOQ, and sensitivity calculations.*

As shown in Figure 4.4a, the CV responses show that higher LiCl concentrations result in greater reduction currents than lower concentrations. This trend can be seen more clearly in the dose-response curve (Figure 4.4b), where the differences in peak currents across the concentration range are more apparent. However, at lower concentrations, particularly at 0.005 M and 0.001 M, the current values appear almost identical to the DI water response, forming a plateau region supported by the t-test results, where there is no significant difference between the reduction currents on this range. The plateau region is likely due to the reduction peaks being too weak or indistinct to be reliably identified at these low levels.

To determine LOD, the approach described earlier in Section 3.3.8 was followed. Regression analysis was applied to the clearly defined portion of the dose-response curve to get the best fitting curve. The data of this region along with the R^2 value and fit quality are shown in Figure 4.4c, from which the sensor function was determined for the calculation of LOD, LOQ and sensitivity of the function. The sensor function of this sensor is y= 0.038 + 1.243x. From the sensor function the sensitivity of the sensor is 1.243 mA/M. The limit of blank was determined to be 0.038 mA using the $(mean)_{blank}$ = 0.028 mA and the SD_{blank} = 0.006. From this the $LOD_{current}$ was determined to be 0.049 mA, using the $SD_{(low\ concentration\ sample)}$= 0.007. The low concentration sample was determined to be 0.001 M which was close to the blank sample. The resulting value for LOD is calculated as 0.0093 M (9.3 mM), where the LOQ is determined to be 0.05635 M (56.3 mM). The LOD and LOQ are close to that achieved using LMO-modified LIG electrodes fabricated on PI film, demonstrating consistent performance even with integrating the microfluidic platform.

4.4 Discussion

This work presents a combined approach for electrochemical sensing and microfluidic integration using a 3D printing-based fabrication method. The entire process from printing the bottom layers of the device, fabricating the electrodes, and functionalizing them to printing the microfluidic channel was completed with one printer containing different toolheads. This made the full fabrication workflow seamless and easy to implement and is demonstrated here for the first time. Both the substrate for the LIG electrodes and the microchannel were printed using the same material and parameters, which removed the need for extra assembly steps. This approach offers a cost-effective and efficient way to build integrated sensing platforms. It represents the first example of incorporating functionalized LIG into a 3D-printed microfluidic system using a single, unified process. Two microfluidic channel designs were tested and the triangular microchannel outperformed the rectangular one, with more stability and robustness post-fabricating. As a result, it was selected for subsequent experiments. With the addition of the microfluidic channel, the functionalized LIG electrodes showed a more stable electrochemical response at a scan rate of 5 mV/s. The microchannel likely contributed to more controlled analyte flow and interaction, allowing the system to consistently reach equilibrium. Compared to the non-microfluidic setup, the oxidation and reduction peak current densities increased by 69.1% and 31.6%, respectively, despite the reduced electrode surface area. Despite reduced surface contact due to the microchannel structure, the sensor retained high efficiency for lithium sensing, achieving a LOD of 9.3 mM, LOQ of 56.3 mM, and a sensitivity of 1.243 mA/M. These values are comparable to the

performance of the sensor tested in Chapter 3 without the microfluidic sensor platform, where a larger electrode area was in contact with the analyte solution.

4.5 Conclusion

Here, we demonstrated how LIG and FDM printing with high-temperature thermoplastics can be a promising combination for fabricating a microfluidic-based electrochemical sensor. By the fabricated devices using this streamlined process, Li^+ was successfully detected in DI water as the analyte flowed through the 3D-printed microfluidic channel positioned directly on top of the functionalized LIG electrodes.

A key aspect of this work was optimizing the vertical gap between the LIG surface and the printed microchannel. This parameter was crucial in ensuring integration without damaging the electrode or compromising conductivity, ultimately improving the stability and reproducibility of the sensing platform. With the repeated successful detection of Li^+ ions, it was evident that the printed channel incorporated lithium sensing with functionalized LIG.

The current density of the reduction peaks was higher for the LiCl analyte in this design compared to the sensor presented in Chapter 3, demonstrating the enhanced performance achieved by integrating the microfluidic channel on top of the functionalized LIG electrodes. Key sensor parameters such as LOD, LOQ, and sensitivity were comparable to the earlier design without the microchannel, which further validates the reliability of this integrated platform despite the reduced electrode-electrolyte contact area. These findings confirm that the fully 3D-printed sensing setup operates effectively and provides a promising, low-cost solution for lithium detection. Future

studies involving printed sensors with functionalized LIG electrodes could further broaden the practical applications of LIG technology in electrochemical detection.

5 Conclusion and Future Work

This chapter brings together the key conclusions drawn from each research phase and outlines future directions that can extend the scope and impact of the findings presented in this thesis.

5.1 Thesis Summary and Conclusions

This research comprehensively explores LIG-based electrochemical sensors, from optimizing fabrication parameters to integrating microfluidic platforms for lithium-ion detection. The study demonstrates a series of approaches that offer low-cost, scalable, and effective solutions for sensor development, particularly in detecting lithium ions with selective detection towards lithium.

The initial part of the study concentrated on optimizing plasma treatment duration to enhance and optimize the electrochemical performance of LIG electrodes in the best conditions. At a fixed power level of 25 W, plasma treatment duration significantly modulated the sensor performance. A treatment duration of 50 seconds delivered the most effective results, with a 225% increase in CV peak current measurements. The optimized plasma-treated devices achieved an LOD of 0.07 mM, an LOQ of 0.132 mM, and a sensitivity of 192.9 µA/mM, in contrast to the untreated devices, which exhibited an LOD of 0.927 mM, an LOQ of 1.837 mM, and a sensitivity of 24.32 µA/mM. This improvement is attributed to the optimal balance between enhanced surface wettability and controlled defect formation. While increased wettability facilitates better electrochemical interactions, extended plasma exposure leads to excessive defect formation that hinders charge transfer.

In the next phase, the LIG electrodes were functionalized by dispense-printing LMO onto the working electrode, enabling the development of a lithium-specific electrochemical sensor. Comparative studies showed that electrodes with LMO printed on LIG performed significantly better than those with LMO printed on bare PI, emphasizing the important role of the LIG layer in enhancing electrochemical detection. Electrochemical testing confirmed the adequate sensitivity and selectivity of the LIG_LMO electrodes, with an LOD, LOQ and sensitivity of 10.8 mM, 155 mM, and 2.693 mA/M. The scan rate optimization identified 5 mV/s as the ideal setting for achieving quasi-reversible peaks, and interference studies using Na^+ and K^+ further validated the sensor's selective detection of lithium ions over other interfering ions.

The final stage of this research integrated the electrochemical sensor with a 3D-printed microfluidic sensing platform, showcasing a fully additive manufacturing approach. This is the first reported integration of LIG-based electrodes within a microfluidic device using 3D printing and dispense printing techniques. Two microchannel geometries were tested to identify the most robust and reliable design. The triangular channel with a height of 0.8 mm and width of 1 mm demonstrated superior structural integrity and consistent performance, while the rectangular design showed partial collapse. One important part of the integration was setting the proper vertical gap between the LIG surface and the bottom of the microchannel. If the gap was too small, the 3D printer nozzle could press against the electrode and damage it during the microchannel fabrication. By carefully adjusting this distance, we avoided damaging the LIG, maintained good conductivity, and ensured the sensor stayed stable and leakage-free in the interface after fabrication. Electrochemical measurements using LiCl further confirmed the platform's selective detection of

Li^+ , with a LOD of 9.3 mM, LOQ of 40.5 mM, and sensitivity of 1.243 mA/M consistent with earlier configurations.

5.2 Future Work

Several promising directions can be pursued to further advance the development and application of LIG-based electrochemical sensors. For instance, optimizing laser processing conditions, such as using an inert gas atmosphere like argon during scribing, can significantly modify the surface properties of LIG, including reducing its hydrophobicity. This surface tuning can enhance the sensor's interaction with aqueous solutions, improving its overall performance. Additionally, a particularly exciting avenue is the application of LIG sensors in smart agriculture, where they could be tailored to monitor critical soil nutrients such as nitrate, phosphate, and potassium, enabling more precise and sustainable farming practices. Building on the current findings, another important direction involves functionalizing LIG with other electrochemically active materials beyond LMO to detect a broader range of analytes, including heavy metals, environmental pollutants, and agricultural ions. Materials such as NiO, MoS_2**,** and conductive polymers could be investigated for enhancing selectivity and extending the sensing capabilities of LIG.

Future work should also focus on completing comprehensive evaluations of specificity and selectivity. Specifically, the sensor's ability to accurately detect the target analyte in the presence of potential interferences should be assessed at mid-range concentrations, typically within the range that meets the end user's needs. Selectivity, on the other hand, should be evaluated by testing the sensor's response at the LOD in the presence of competing species at tenfold higher

concentrations. Thoroughly addressing these aspects will be crucial to validate the robustness and practical applicability of LIG-based sensors.

Further performance enhancement can also be achieved by optimizing microfluidic design. Introducing more complex microchannel geometries such as zigzag or serpentine patterns can increase the residence time of analytes near the sensing surface, thereby improving sensitivity through more effective analyte-electrode interaction. In addition, the substrate materials used for LIG generation could be expanded beyond PEI to include alternatives like PSU, PEEK, or carbon-filled polymers, which might offer improved mechanical strength, thermal stability, and bonding compatibility. A comparative study of how different substrates influence LIG quality and sensor performance would provide valuable insights for selecting optimal materials in future designs.

Improving the stability and shelf life of LIG-based sensors is an important area for future research, especially for applications like biosensors that need to work reliably over time. This can be done by finding better ways to protect the LIG surface from damage and environmental exposure. For example, adding protective layers like tetrathiafulvalene [125] or using improved sealing materials could help the sensors last longer and stay effective during storage. Improving the uniformity and reliability of coating conductive layers on top of LIG is another important research direction that could expand the performance window of LIG-based sensors. One of the current challenges is achieving consistent and well-controlled coating, which directly affects the sensor's conductivity and stability. Inkjet printing offers a promising solution, as it allows precise deposition of functional materials with better control over layer thickness and uniformity. Applying inkjet

printing for LIG surface modification could result in more consistent coatings, improved electrical properties, and ultimately better sensor performance.

Beyond sensing, functionalized LIG also holds potential for use in transistors and energy storage devices, opening up new research pathways. Furthermore, surface treatment techniques can play a key role in enhancing sensor performance. While plasma treatment has been widely adopted, it introduces additional steps and uses a vacuum. As an alternative, corona treatment may offer a simpler and more scalable approach to improving LIG wettability and adhesion without significantly altering the fabrication workflow.

References

[1] Y. Li, Z. Wang, L. Sun, L. Liu, C. Xu, and H. Kuang, "Nanoparticle-based sensors for food contaminants," *TrAC Trends in Analytical Chemistry*, vol. 113, pp. 74–83, Apr. 2019, doi: 10.1016/j.trac.2019.01.012.

[2] Y. Liu *et al.*, "A Ratiometric Electrochemical Sensor with Integrated Probe for the Assay of α-glucosidase Activity and Screening of Its Inhibitors," *J. Electrochem. Soc.*, vol. 166, no. 2, p. B133, Feb. 2019, doi: 10.1149/2.1111902jes.

[3] S. Kempahanumakkagari, K. Vellingiri, A. Deep, E. E. Kwon, N. Bolan, and K.-H. Kim, "Metal–organic framework composites as electrocatalysts for electrochemical sensing applications," *Coordination Chemistry Reviews*, vol. 357, pp. 105–129, Feb. 2018, doi: 10.1016/j.ccr.2017.11.028.

[4] T.-Z. Liu *et al.*, "Metal–Organic Framework Nanomaterials as Novel Signal Probes for Electron Transfer Mediated Ultrasensitive Electrochemical Immunoassay," *Anal. Chem.*, vol. 88, no. 24, pp. 12516–12523, Dec. 2016, doi: 10.1021/acs.analchem.6b04191.

[5] K. Avinash and F. Patolsky, "Laser-induced graphene structures: From synthesis and applications to future prospects," *Materials Today*, vol. 70, pp. 104–136, Nov. 2023, doi: 10.1016/j.mattod.2023.10.009.

[6] Z. Zhang *et al.*, "A review of laser-induced graphene: From experimental and theoretical fabrication processes to emerging applications," *Carbon*, vol. 214, p. 118356, Oct. 2023, doi: 10.1016/j.carbon.2023.118356.

[7] A. L. Suherman *et al.*, “Electrochemical Detection and Quantification of Lithium Ions in Authentic Human Saliva Using LiMn2O4-Modified Electrodes,” *ACS Sens.*, vol. 4, no. 9, pp. 2497–2506, Sep. 2019, doi: 10.1021/acssensors.9b01176.

[8] P. P. Paul *et al.*, “A Review of Existing and Emerging Methods for Lithium Detection and Characterization in Li-Ion and Li-Metal Batteries,” *Advanced Energy Materials*, vol. 11, no. 17, p. 2100372, 2021, doi: 10.1002/aenm.202100372.

[9] A. Fernández-la-Villa, D. F. Pozo-Ayuso, and M. Castaño-Álvarez, “Microfluidics and electrochemistry: an emerging tandem for next-generation analytical microsystems,” *Current Opinion in Electrochemistry*, vol. 15, pp. 175–185, Jun. 2019, doi: 10.1016/j.coelec.2019.05.014.

[10] G. Yang, L. Li, W. B. Lee, and M. C. Ng, “Structure of graphene and its disorders: a review,” *Science and Technology of Advanced Materials*, vol. 19, no. 1, pp. 613–648, Dec. 2018, doi: 10.1080/14686996.2018.1494493.

[11] Z. Zhen and H. Zhu, “1 - Structure and Properties of Graphene,” in *Graphene*, H. Zhu, Z. Xu, D. Xie, and Y. Fang, Eds., Academic Press, 2018, pp. 1–12. doi: 10.1016/B978-0-12-812651-6.00001-X.

[12] M. Taghioskoui, “Trends in graphene research,” *Materials Today*, vol. 12, no. 10, pp. 34–37, Oct. 2009, doi: 10.1016/S1369-7021(09)70274-3.

[13] H. Kim and J.-H. Ahn, “Graphene for flexible and wearable device applications,” *Carbon*, vol. 120, pp. 244–257, Aug. 2017, doi: 10.1016/j.carbon.2017.05.041.

[14] A. Minhas-Khan, S. Nambi, and G. Grau, “Low-resistance laser-induced graphitic carbon by maximizing energy delivery and pulse overlap,” *Carbon*, vol. 181, pp. 310–322, Aug. 2021, doi: 10.1016/j.carbon.2021.05.037.

[15] G. Reina, J. Miguel González-Domínguez, A. Criado, E. Vázquez, A. Bianco, and M. Prato, “Promises, facts and challenges for graphene in biomedical applications,” *Chemical Society Reviews*, vol. 46, no. 15, pp. 4400–4416, 2017, doi: 10.1039/C7CS00363C.

[16] U. Harini and C. Ponraj, “Review—Graphene-Based Electrochemical Sensors for Detecting Environmental Pollutants,” *J. Electrochem. Soc.*, vol. 171, no. 2, p. 027521, Feb. 2024, doi: 10.1149/1945-7111/ad26e3.

[17] S. Movaghgharnezhad and P. Kang, “Laser-induced graphene: synthesis advances, structural tailoring, enhanced properties, and sensing applications,” *Journal of Materials Chemistry C*, vol. 12, no. 19, pp. 6718–6742, 2024, doi: 10.1039/D3TC04677J.

[18] A. Behrent, C. Griesche, P. Sippel, and A. J. Baeumner, “Process-property correlations in laser-induced graphene electrodes for electrochemical sensing,” *Microchim Acta*, vol. 188, no. 5, p. 159, Apr. 2021, doi: 10.1007/s00604-021-04792-3.

[19] J. Lin *et al.*, “Laser-induced porous graphene films from commercial polymers,” *Nat Commun*, vol. 5, no. 1, p. 5714, Dec. 2014, doi: 10.1038/ncomms6714.

[20] D. Kwak *et al.*, “Investigation of Laser-Induced Graphene (LIG) on a Flexible Substrate and Its Functionalization by Metal Doping for Gas-Sensing Applications,” *International Journal of Molecular Sciences*, vol. 25, no. 2, Art. no. 2, Jan. 2024, doi: 10.3390/ijms25021172.

[21] S. P. Lee, P. S. Chee, C. H. Tan, K. F. Chong, E. H. Lim, and C. Guan, "A review on laser-induced graphene in flexible energy storage: From materials selection to biomedical applications," *Chemical Engineering Journal*, vol. 499, p. 156110, Nov. 2024, doi: 10.1016/j.cej.2024.156110.

[22] S. G. Jo, R. Ramkumar, and J. W. Lee, "Recent Advances in Laser-Induced Graphene-Based Materials for Energy Storage and Conversion," *ChemSusChem*, vol. 17, no. 5, p. e202301146, 2024, doi: 10.1002/cssc.202301146.

[23] S. Choudhury *et al.*, "Potentiometric ion-selective sensors based on UV-ozone irradiated laser-induced graphene electrode," *Electrochimica Acta*, vol. 387, p. 138341, Aug. 2021, doi: 10.1016/j.electacta.2021.138341.

[24] C.-W. Lee, S.-Y. Jeong, Y.-W. Kwon, J.-U. Lee, S.-C. Cho, and B.-S. Shin, "Fabrication of laser-induced graphene-based multifunctional sensing platform for sweat ion and human motion monitoring," *Sensors and Actuators A: Physical*, vol. 334, p. 113320, Feb. 2022, doi: 10.1016/j.sna.2021.113320.

[25] I. S. Kucherenko *et al.*, "Ion-Selective Sensors Based on Laser-Induced Graphene for Evaluating Human Hydration Levels Using Urine Samples," *Advanced Materials Technologies*, vol. 5, no. 6, p. 1901037, 2020, doi: 10.1002/admt.201901037.

[26] S. Luo, P. T. Hoang, and T. Liu, "Direct laser writing for creating porous graphitic structures and their use for flexible and highly sensitive sensor and sensor arrays," *Carbon*, vol. 96, pp. 522–531, Jan. 2016, doi: 10.1016/j.carbon.2015.09.076.

[27] J. Zhao *et al.*, "Novel multi-walled carbon nanotubes-embedded laser-induced graphene in crosslinked architecture for highly responsive asymmetric pressure sensor," *Sensors and Actuators A: Physical*, vol. 323, p. 112658, Jun. 2021, doi: 10.1016/j.sna.2021.112658.

[28] J. Baranwal, B. Barse, G. Gatto, G. Broncova, and A. Kumar, "Electrochemical Sensors and Their Applications: A Review," *Chemosensors*, vol. 10, no. 9, Art. no. 9, Sep. 2022, doi: 10.3390/chemosensors10090363.

[29] P. Bollella *et al.*, "Beyond graphene: Electrochemical sensors and biosensors for biomarkers detection," *Biosensors and Bioelectronics*, vol. 89, pp. 152–166, Mar. 2017, doi: 10.1016/j.bios.2016.03.068.

[30] M. Bengtsson, G. Thrastardottir, T. S. Hansen, and O. Geschke, "All polymer electrochemical sensor," in *4M 2006 - Second International Conference on Multi-Material Micro Manufacture*, W. Menz, S. Dimov, and B. Fillon, Eds., Oxford: Elsevier, 2006, pp. 365–367. doi: 10.1016/B978-008045263-0/50083-0.

[31] L. Chen and R. G. Compton, "Reference Electrodes for Electrochemical Sensors Based on Redox Couples Immobilized within Nafion Films," *ACS Sens.*, vol. 4, no. 6, pp. 1716–1723, Jun. 2019, doi: 10.1021/acssensors.9b00693.

[32] C. Lefrou, R. P. Nogueira, F. Huet, and H. Takenouti, "1.02 - Electrochemistry," in *Shreir's Corrosion*, B. Cottis, M. Graham, R. Lindsay, S. Lyon, T. Richardson, D. Scantlebury, and H. Stott, Eds., Oxford: Elsevier, 2010, pp. 13–51. doi: 10.1016/B978-044452787-5.00003-2.

[33] J. M. Mohan, K. Amreen, A. Javed, S. K. Dubey, and S. Goel, “Emerging trends in miniaturized and microfluidic electrochemical sensing platforms,” *Current Opinion in Electrochemistry*, vol. 33, p. 100930, Jun. 2022, doi: 10.1016/j.coelec.2021.100930.

[34] S. Hong *et al.*, “Fabrication of screen-printed electrodes with long-term stability for voltammetric and potentiometric applications,” *Sensors and Actuators Reports*, vol. 8, p. 100234, Dec. 2024, doi: 10.1016/j.snr.2024.100234.

[35] M. F. Bergamini and M. V. Boldrin Zanoni, “Anodic Stripping Voltammetric Determination of Aurothiomalate in Urine Using a Screen-Printed Carbon Electrode,” *Electroanalysis*, vol. 18, no. 15, pp. 1457–1462, 2006, doi: 10.1002/elan.200603534.

[36] M. Li, D.-W. Li, G. Xiu, and Y.-T. Long, “Applications of screen-printed electrodes in current environmental analysis,” *Current Opinion in Electrochemistry*, vol. 3, no. 1, pp. 137–143, Jun. 2017, doi: 10.1016/j.coelec.2017.08.016.

[37] R. D. Crapnell and C. E. Banks, “Electroanalytical Overview: Screen-Printed Electrochemical Sensing Platforms,” *ChemElectroChem*, vol. 11, no. 19, p. e202400370, 2024, doi: 10.1002/celc.202400370.

[38] S. R. Benjamin and E. J. Miranda Ribeiro Júnior, “Graphene-Based electrochemical sensors for detection of environmental pollutants,” *Current Opinion in Environmental Science & Health*, vol. 29, p. 100381, Oct. 2022, doi: 10.1016/j.coesh.2022.100381.

[39] B.-R. Adhikari, M. Govindhan, and A. Chen, “Sensitive Detection of Acetaminophen with Graphene-Based Electrochemical Sensor,” *Electrochimica Acta*, vol. 162, pp. 198–204, Apr. 2015, doi: 10.1016/j.electacta.2014.10.028.

[40] X. Wang and Y. Shi, “Fabrication Techniques of Graphene Nanostructures”, Accessed: Apr. 14, 2025. [Online]. Available: https://books.rsc.org/books/edited-volume/1045/chapter/860613/Fabrication-Techniques-of-Graphene-Nanostructures

[41] P. Murugan *et al.*, “Electrochemical Detection of H2O2 Using an Activated Glassy Carbon Electrode,” *ECS Sens. Plus*, vol. 1, no. 3, p. 034401, Jul. 2022, doi: 10.1149/2754-2726/ac7c78.

[42] A. Salimi, H. Mamkhezri, R. Hallaj, and S. Soltanian, “Electrochemical detection of trace amount of arsenic(III) at glassy carbon electrode modified with cobalt oxide nanoparticles,” *Sensors and Actuators B: Chemical*, vol. 129, no. 1, pp. 246–254, Jan. 2008, doi: 10.1016/j.snb.2007.08.017.

[43] M. Taheri, I. A. Deen, M. Packirisamy, and M. J. Deen, “Metal oxide -based electrical/electrochemical sensors for health monitoring systems,” *TrAC Trends in Analytical Chemistry*, vol. 171, p. 117509, Feb. 2024, doi: 10.1016/j.trac.2023.117509.

[44] A. S. Agnihotri, A. Varghese, and N. M, “Transition metal oxides in electrochemical and bio sensing: A state-of-art review,” *Applied Surface Science Advances*, vol. 4, p. 100072, Jun. 2021, doi: 10.1016/j.apsadv.2021.100072.

[45] C. Fenzl, P. Nayak, T. Hirsch, O. S. Wolfbeis, H. N. Alshareef, and A. J. Baeumner, "Laser-Scribed Graphene Electrodes for Aptamer-Based Biosensing," *ACS Sens.*, vol. 2, no. 5, pp. 616–620, May 2017, doi: 10.1021/acssensors.7b00066.

[46] M. Bauer *et al.*, "Electrochemical multi-analyte point-of-care perspiration sensors using on-chip three-dimensional graphene electrodes," *Anal Bioanal Chem*, vol. 413, no. 3, pp. 763–777, Jan. 2021, doi: 10.1007/s00216-020-02939-4.

[47] C. Park *et al.*, "Electrochemical sensor based on laser-induced graphene and CeO2 for sensitive and selective dopamine detection," *Journal of Electroanalytical Chemistry*, vol. 977, p. 118865, Jan. 2025, doi: 10.1016/j.jelechem.2024.118865.

[48] X. Liu *et al.*, "Laser-induced graphene (LIG)-based electrochemical microfluidic chip for simultaneous analysis of multiplex microRNAs," *Chemical Engineering Journal*, vol. 486, p. 150233, Apr. 2024, doi: 10.1016/j.cej.2024.150233.

[49] B. De Chiara *et al.*, "Correction to 'Laser-Induced Metal–Organic Framework-Derived Flexible Electrodes for Electrochemical Sensing,'" *ACS Appl. Mater. Interfaces*, vol. 17, no. 6, pp. 10192–10192, Feb. 2025, doi: 10.1021/acsami.5c01326.

[50] M. D. Wagh, S. K. Sahoo, and S. Goel, "Laser-induced graphene ablated polymeric microfluidic device with interdigital electrodes for taste sensing application," *Sensors and Actuators A: Physical*, vol. 333, p. 113301, Jan. 2022, doi: 10.1016/j.sna.2021.113301.

[51] A. V. Shokurov and C. Menon, “Laser-Induced Graphene Electrodes for Electrochemistry Education and Research,” *J. Chem. Educ.*, vol. 100, no. 6, pp. 2411–2417, Jun. 2023, doi: 10.1021/acs.jchemed.2c01237.

[52] W. A. Ameku *et al.*, “Laser-Scribed Graphene-Based Electrochemical Sensors: A Review,” *Chemosensors*, vol. 10, no. 12, Art. no. 12, Dec. 2022, doi: 10.3390/chemosensors10120505.

[53] A. Dallinger, F. Steinwender, M. Gritzner, and F. Greco, “Different Roles of Surface Chemistry and Roughness of Laser-Induced Graphene: Implications for Tunable Wettability,” *ACS Appl. Nano Mater.*, vol. 6, no. 18, pp. 16201–16211, Sep. 2023, doi: 10.1021/acsanm.3c02066.

[54] H. Lee, I. Ohsawa, and J. Takahashi, “Effect of plasma surface treatment of recycled carbon fiber on carbon fiber-reinforced plastics (CFRP) interfacial properties,” *Applied Surface Science*, vol. 328, pp. 241–246, Feb. 2015, doi: 10.1016/j.apsusc.2014.12.012.

[55] Z. Zhang, J. L. Wilson, B. R. Kitt, and D. W. Flaherty, “Effects of Oxygen Plasma Treatments on Surface Functional Groups and Shear Strength of Carbon Fiber Composites,” *ACS Applied Polymer Materials*, vol. 3, no. 2, pp. 986–995, Feb. 2021, doi: 10.1021/acsapm.0c01270.

[56] C. Li, J. Xiong, and J. Zhao, “Oxygen plasma treatment-enhanced humidity sensing performance of MoS2 nanoparticles-anchored nitrogen-doped laser-induced graphene,” *Sensors and Actuators B: Chemical*, vol. 408, p. 135528, Jun. 2024, doi: 10.1016/j.snb.2024.135528.

[57] J. Zhang, M. Ren, L. Wang, Y. Li, B. I. Yakobson, and J. M. Tour, "Oxidized Laser-Induced Graphene for Efficient Oxygen Electrocatalysis," *Advanced Materials*, vol. 30, no. 21, p. 1707319, 2018, doi: 10.1002/adma.201707319.

[58] M. Nazeri, M. Ghalamboran, and G. Grau, "Laser-Induced Graphene Electrodes for Organic Electrochemical Transistors (OECTs)," *Advanced Materials Technologies*, vol. 8, no. 17, p. 2300188, 2023, doi: 10.1002/admt.202300188.

[59] R. Kumar Biswas, P. McGlynn, G. M. O'Connor, and P. Scully, "Plasma enhanced planar crystal growth of laser induced graphene," *Materials Letters*, vol. 343, p. 134362, Jul. 2023, doi: 10.1016/j.matlet.2023.134362.

[60] R. Khan, C. Ryu, and J. B. In, "Fabrication of modified laser-induced graphene using activated carbon and polyamic acid coating for flexible and high-performance microsupercapacitors," *Carbon*, vol. 230, p. 119646, Nov. 2024, doi: 10.1016/j.carbon.2024.119646.

[61] M. M. Hashemi, F. Hasheminia, and S. Sadeghzadeh, "Alkyd Coated Laser-Induced Graphene Patches For Corrosion Resistance of Metal Substrates," Mar. 31, 2025, *Research Square*. doi: 10.21203/rs.3.rs-6234092/v1.

[62] R. Tabassum, P. P. Sarkar, A. H. Jalal, A. Ashraf, and N. Islam, "Laser-Induced Electrochemical Biosensor Modified with Graphene-Based Ink for Label-Free Detection of Alpha-Fetoprotein and 17β-Estradiol," *Polymers*, vol. 16, no. 14, Art. no. 14, Jan. 2024, doi: 10.3390/polym16142069.

[63] L. Meng, A. P. F. Turner, and W. C. Mak, “Conducting Polymer-Reinforced Laser-Irradiated Graphene as a Heterostructured 3D Transducer for Flexible Skin Patch Biosensors,” *ACS Appl. Mater. Interfaces*, vol. 13, no. 45, pp. 54456–54465, Nov. 2021, doi: 10.1021/acsami.1c13164.

[64] D. Ghosh *et al.*, “Graphene Nanocomposite Ink Coated Laser Transformed Flexible Electrodes for Selective Dopamine Detection and Immunosensing,” *ACS Appl. Bio Mater.*, vol. 7, no. 5, pp. 3143–3153, May 2024, doi: 10.1021/acsabm.4c00166.

[65] A. Tomaszewska *et al.*, “Lithium-ion battery fast charging: A review,” *eTransportation*, vol. 1, p. 100011, Aug. 2019, doi: 10.1016/j.etran.2019.100011.

[66] Z. Li, J. Huang, B. Yann Liaw, V. Metzler, and J. Zhang, “A review of lithium deposition in lithium-ion and lithium metal secondary batteries,” *Journal of Power Sources*, vol. 254, pp. 168–182, May 2014, doi: 10.1016/j.jpowsour.2013.12.099.

[67] M. I. Albero, J. A. Ortuño, M. S. García, M. Cuartero, and M. C. Alcaraz, “Novel flow-through bulk optode for spectrophotometric determination of lithium in pharmaceuticals and saliva,” *Sensors and Actuators B: Chemical*, vol. 145, no. 1, pp. 133–138, Mar. 2010, doi: 10.1016/j.snb.2009.11.053.

[68] E. Hirayama, T. Sugiyama, H. Hisamoto, and K. Suzuki, “Visual and colorimetric lithium ion sensing based on digital color analysis,” *Anal Chem*, vol. 72, no. 3, pp. 465–474, Feb. 2000, doi: 10.1021/ac990588w.

[69] E. X. Vrouwe, R. Luttge, and A. van den Berg, “Direct measurement of lithium in whole blood using microchip capillary electrophoresis with integrated conductivity detection,” *ELECTROPHORESIS*, vol. 25, no. 10–11, pp. 1660–1667, 2004, doi: 10.1002/elps.200405885.

[70] N. Lewen and D. Nugent, “The use of inductively coupled plasma-atomic emission spectroscopy (ICP-AES) in the determination of lithium in cleaning validation swabs,” *Journal of Pharmaceutical and Biomedical Analysis*, vol. 52, no. 5, pp. 652–655, Sep. 2010, doi: 10.1016/j.jpba.2010.02.015.

[71] D. B. Stubing, S. Heng, and A. D. Abell, “Crowned spiropyran fluoroionophores with a carboxyl moiety for the selective detection of lithium ions,” *Org. Biomol. Chem.*, vol. 14, no. 15, pp. 3752–3757, Apr. 2016, doi: 10.1039/C6OB00468G.

[72] K. J. Cloete, B. Jenčič, Ž. Šmit, M. Kelemen, K. Mkentane, and P. Pelicon, “Detection of lithium in scalp hair by time-of-flight secondary ion mass spectrometry with high energy (MeV) primary ions,” *Anal. Methods*, vol. 9, no. 36, pp. 5249–5253, Sep. 2017, doi: 10.1039/C7AY01616F.

[73] M. N. Sweilam, J. R. Varcoe, and C. Crean, “Fabrication and Optimization of Fiber-Based Lithium Sensor: A Step toward Wearable Sensors for Lithium Drug Monitoring in Interstitial Fluid,” *ACS Sens.*, vol. 3, no. 9, pp. 1802–1810, Sep. 2018, doi: 10.1021/acssensors.8b00528.

[74] I. A. Vitale, G. Selvolini, and G. Marrazza, “Smart Sensor for Lithium Detection: An Environmental Application,” *Chemosensors*, vol. 11, no. 2, Art. no. 2, Feb. 2023, doi: 10.3390/chemosensors11020077.

[75] F. Criscuolo, I. Taurino, F. Stradolini, S. Carrara, and G. De Micheli, “Highly-stable Li+ ion-selective electrodes based on noble metal nanostructured layers as solid-contacts,” *Analytica Chimica Acta*, vol. 1027, pp. 22–32, Oct. 2018, doi: 10.1016/j.aca.2018.04.062.

[76] R. B. Kristiawan, F. Imaduddin, D. Ariawan, Ubaidillah, and Z. Arifin, “A review on the fused deposition modeling (FDM) 3D printing: Filament processing, materials, and printing parameters,” *Open Engineering*, vol. 11, no. 1, pp. 639–649, Jan. 2021, doi: 10.1515/eng-2021-0063.

[77] X. Ma *et al.*, “PEI doped In2O3 nanospheres based gas sensor for high-performance formaldehyde detection,” *Sensors and Actuators B: Chemical*, vol. 431, p. 137374, May 2025, doi: 10.1016/j.snb.2025.137374.

[78] M. Tavakkoli Gilavan, M. S. Rahman, A. Minhas-Khan, S. Nambi, and G. Grau, “One-Step Fabrication of Low-Resistance Conductors on 3D-Printed Structures by Laser-Induced Graphene,” *ACS Appl. Electron. Mater.*, vol. 3, no. 9, pp. 3867–3875, Sep. 2021, doi: 10.1021/acsaelm.1c00480.

[79] M. Wu *et al.*, “Influence of defocusing of UV pulse laser radiation on LIG synthesis on Polyetheretherketone,” *Diamond and Related Materials*, vol. 150, p. 111701, Dec. 2024, doi: 10.1016/j.diamond.2024.111701.

[80] J. Vandervelde, Y. Yoon, R. Shahriar, S. B. Cronin, and Y. Chen, “Additive and Laser Manufacturing for Multifunctional Electronics on High-Performance Polymers,” *Small Science*, vol. n/a, no. n/a, p. 2500022, doi: 10.1002/smsc.202500022.

[81] G. M. Whitesides, “The origins and the future of microfluidics,” *Nature*, vol. 442, no. 7101, pp. 368–373, Jul. 2006, doi: 10.1038/nature05058.

[82] A. Doostmohammadi, H. Huang, S. Naushad, and P. Rezai, “Portable cell imprinted polymer-based microfluidic sensor for bacteria detection in real water,” *Microchemical Journal*, vol. 206, p. 111611, Nov. 2024, doi: 10.1016/j.microc.2024.111611.

[83] S. Li *et al.*, “Electrochemical microfluidics techniques for heavy metal ion detection,” *Analyst*, vol. 143, no. 18, pp. 4230–4246, 2018, doi: 10.1039/C8AN01067F.

[84] S. Halldorsson, E. Lucumi, R. Gómez-Sjöberg, and R. M. T. Fleming, “Advantages and challenges of microfluidic cell culture in polydimethylsiloxane devices,” *Biosensors and Bioelectronics*, vol. 63, pp. 218–231, Jan. 2015, doi: 10.1016/j.bios.2014.07.029.

[85] C. Iliescu, H. Taylor, M. Avram, J. Miao, and S. Franssila, “A practical guide for the fabrication of microfluidic devices using glass and silicon,” *Biomicrofluidics*, vol. 6, no. 1, p. 016505, Mar. 2012, doi: 10.1063/1.3689939.

[86] C. M. Pandey *et al.*, “Microfluidics Based Point-of-Care Diagnostics,” *Biotechnology Journal*, vol. 13, no. 1, p. 1700047, 2018, doi: 10.1002/biot.201700047.

[87] C.-W. Tsao, “Polymer Microfluidics: Simple, Low-Cost Fabrication Process Bridging Academic Lab Research to Commercialized Production,” *Micromachines*, vol. 7, no. 12, Art. no. 12, Dec. 2016, doi: 10.3390/mi7120225.

[88] B. K. Gale *et al.*, “A Review of Current Methods in Microfluidic Device Fabrication and Future Commercialization Prospects,” *Inventions*, vol. 3, no. 3, Art. no. 3, Sep. 2018, doi: 10.3390/inventions3030060.

[89] H. van Heeren, R. Tantra, and P. Salomon, “Microfluidic devices: a road forward by standardization of interconnects and classification,” *Microfluid Nanofluid*, vol. 19, no. 5, pp. 1203–1207, Nov. 2015, doi: 10.1007/s10404-015-1639-4.

[90] B. Neuhaus, M. K. Idris, P. Naderi, Y. El-Hajj, and G. Grau, “Low-Roughness 3D-Printed Surfaces by Ironing for the Integration with Printed Electronics,” *Adv Eng Mater*, vol. 26, no. 3, p. 2301711, Feb. 2024, doi: 10.1002/adem.202301711.

[91] B. M. de C. Costa, S. Griveau, F. Bedioui, F. d’Orlye, J. A. F. da Silva, and A. Varenne, “Stereolithography based 3D-printed microfluidic device with integrated electrochemical detection,” *Electrochimica Acta*, vol. 407, p. 139888, Mar. 2022, doi: 10.1016/j.electacta.2022.139888.

[92] R. Su, F. Wang, and M. C. McAlpine, “3D printed microfluidics: advances in strategies, integration, and applications,” *Lab Chip*, vol. 23, no. 5, pp. 1279–1299, Mar. 2023, doi: 10.1039/D2LC01177H.

[93] C. M. Benjamin Ho, S. Huan Ng, K. H. Holden Li, and Y.-J. Yoon, “3D printed microfluidics for biological applications,” *Lab on a Chip*, vol. 15, no. 18, pp. 3627–3637, 2015, doi: 10.1039/C5LC00685F.

[94] S. Ma *et al.*, “A portable microfluidic electrochemical sensing platform for rapid detection of hazardous metal Pb2+ based on thermocapillary convection using 3D Ag-rGO-*f*-Ni(OH)2/NF as a signal amplifying element,” *Journal of Hazardous Materials*, vol. 448, p. 130923, Apr. 2023, doi: 10.1016/j.jhazmat.2023.130923.

[95] L.-L. Shen, G.-R. Zhang, W. Li, M. Biesalski, and B. J. M. Etzold, “Modifier-Free Microfluidic Electrochemical Sensor for Heavy-Metal Detection,” *ACS Omega*, vol. 2, no. 8, pp. 4593–4603, Aug. 2017, doi: 10.1021/acsomega.7b00611.

[96] C. Griesche, K. Hoecherl, and A. J. Baeumner, “Substrate-Independent Laser-Induced Graphene Electrodes for Microfluidic Electroanalytical Systems,” *ACS Appl. Nano Mater.*, vol. 4, no. 3, pp. 3114–3121, Mar. 2021, doi: 10.1021/acsanm.1c00299.

[97] Z. T. Johnson *et al.*, “Enhanced Laser-Induced Graphene Microfluidic Integrated Sensors (LIGMIS) for On-Site Biomedical and Environmental Monitoring,” *Small*, vol. n/a, no. n/a, p. 2500262, doi: 10.1002/smll.202500262.

[98] B. Chen *et al.*, “Tuning the Structure, Conductivity, and Wettability of Laser-Induced Graphene for Multiplexed Open Microfluidic Environmental Biosensing and Energy Storage Devices,” *ACS Nano*, vol. 16, no. 1, pp. 15–28, Jan. 2022, doi: 10.1021/acsnano.1c04197.

[99] P. Chytrosz-Wrobel, M. Golda-Cepa, E. Stodolak-Zych, J. Rysz, and A. Kotarba, “Effect of oxygen plasma-treatment on surface functional groups, wettability, and nanotopography features of medically relevant polymers with various crystallinities,” *Applied Surface Science Advances*, vol. 18, p. 100497, Dec. 2023, doi: 10.1016/j.apsadv.2023.100497.

[100] S. F. Jafri *et al.*, “Large Orbital Magnetic Moment Measured in the [TpFeIII(CN)3]− Precursor of Photomagnetic Molecular Prussian Blue Analogues,” *Inorg. Chem.*, vol. 55, no. 14, pp. 6980–6987, Jul. 2016, doi: 10.1021/acs.inorgchem.6b00664.

[101] I. Taurino, S. Carrara, M. Giorcelli, A. Tagliaferro, and G. De Micheli, “Comparison of two different carbon nanotube-based surfaces with respect to potassium ferricyanide electrochemistry,” *Surface Science*, vol. 606, no. 3, pp. 156–160, Feb. 2012, doi: 10.1016/j.susc.2011.09.001.

[102] J. A. Ribeiro, E. Silva, P. S. Moreira, and C. M. Pereira, “Electrochemical Characterization of Redox Probes at Gold Screen-Printed Electrodes: Efforts towards Signal Stability,” *ChemistrySelect*, vol. 5, no. 17, pp. 5041–5048, 2020, doi: 10.1002/slct.202001411.

[103] L. Shen *et al.*, “Highly porous nanofiber-supported monolayer graphene membranes for ultrafast organic solvent nanofiltration,” *Science Advances*, vol. 7, no. 37, p. eabg6263, Sep. 2021, doi: 10.1126/sciadv.abg6263.

[104] J. F. S. Pereira *et al.*, “Reactive oxygen plasma treatment of 3D-printed carbon electrodes towards high-performance electrochemical sensors,” *Sensors and Actuators B: Chemical*, vol. 347, p. 130651, Nov. 2021, doi: 10.1016/j.snb.2021.130651.

[105] M. Garzia Trulli *et al.*, “Towards highly stable aqueous dispersions of multi-walled carbon nanotubes: the effect of oxygen plasma functionalization,” *Journal of Colloid and Interface Science*, vol. 491, pp. 255–264, Apr. 2017, doi: 10.1016/j.jcis.2016.12.039.

[106] Y. Koç, U. Morali, S. Erol, and H. Avci, “Investigation of electrochemical behavior of potassium ferricyanide/ferrocyanide redox probes on screen printed carbon electrode through cyclic voltammetry and electrochemical impedance spectroscopy,” *Turk J Chem*, vol. 45, no. 6, pp. 1895–1915, 2021, doi: 10.3906/kim-2105-55.

[107] D. A. Armbruster and T. Pry, “Limit of Blank, Limit of Detection and Limit of Quantitation,” *Clin Biochem Rev*, vol. 29, no. Suppl 1, pp. S49–S52, Aug. 2008.

[108] R. A. Robinson and R. H. Stokes, *Electrolyte Solutions: Second Revised Edition*. Courier Corporation, 2002.

[109] S. D. Shovan, S. A. Ringky, A. M. Islam, S. Islam, and M. J. Rashid, “Maximizing the solar output power using hybrid (CdS/ZnSe) buffer for CIGS thin film solar cell,” *Physica Scripta*, vol. 98, no. 11, p. 115945, 2023.

[110] K. Ariyoshi *et al.*, “Electrochemical Impedance Spectroscopy Part 1: Fundamentals,” *Electrochemistry*, vol. 90, no. 10, pp. 102007–102007, 2022, doi: 10.5796/electrochemistry.22-66071.

[111] F. Priante, M. Salim, L. Ottaviano, and F. Perrozzi, “XPS study of graphene oxide reduction induced by (100) and (111)-oriented Si substrates,” *Nanotechnology*, vol. 29, no. 7, p. 075704, Feb. 2018, doi: 10.1088/1361-6528/aaa320.

[112] X. Lu, W.-L. Yim, B. H. R. Suryanto, and C. Zhao, “Electrocatalytic Oxygen Evolution at Surface-Oxidized Multiwall Carbon Nanotubes,” *J. Am. Chem. Soc.*, vol. 137, no. 8, pp. 2901–2907, Mar. 2015, doi: 10.1021/ja509879r.

[113] J.-B. Wu, M.-L. Lin, X. Cong, H.-N. Liu, and P.-H. Tan, “Raman spectroscopy of graphene-based materials and its applications in related devices,” *Chemical Society Reviews*, vol. 47, no. 5, pp. 1822–1873, 2018, doi: 10.1039/C6CS00915H.

[114] A. C. Ferrari and D. M. Basko, “Raman spectroscopy as a versatile tool for studying the properties of graphene,” *Nature Nanotech*, vol. 8, no. 4, pp. 235–246, Apr. 2013, doi: 10.1038/nnano.2013.46.

[115] C. Li, J. Xiong, and J. Zhao, “Oxygen plasma treatment-enhanced humidity sensing performance of MoS2 nanoparticles-anchored nitrogen-doped laser-induced graphene,” *Sensors and Actuators B: Chemical*, vol. 408, p. 135528, Jun. 2024, doi: 10.1016/j.snb.2024.135528.

[116] Y. Liu, B. Ma, Y. Lü, C. Wang, and Y. Chen, “A review of lithium extraction from natural resources,” *Int J Miner Metall Mater*, vol. 30, no. 2, pp. 209–224, Feb. 2023, doi: 10.1007/s12613-022-2544-y.

[117] Q. Mu, C. K. Dunn, L. Wang, M. L. Dunn, H. J. Qi, and T. Wang, “Thermal cure effects on electromechanical properties of conductive wires by direct ink write for 4D printing and soft machines,” *Smart Mater. Struct.*, vol. 26, no. 4, p. 045008, Feb. 2017, doi: 10.1088/1361-665X/aa5cca.

[118] J. Waelder and S. Maldonado, “Beyond the Laviron Method: A New Mathematical Treatment for Analyzing the Faradaic Current in Reversible, Quasi-Reversible, and Irreversible Cyclic Voltammetry of Adsorbed Redox Species,” *Anal. Chem.*, vol. 93, no. 37, pp. 12672–12681, Sep. 2021, doi: 10.1021/acs.analchem.1c02503.

[119] R. Agarwal, “Dos and Dont’s in Determination of Electrochemical Kinetic Parameters of Reversible and Irreversible Redox couples using Cyclic Voltammetry,” *J. Chem. Educ.*, vol. 102, no. 1, pp. 66–77, Jan. 2025, doi: 10.1021/acs.jchemed.4c01224.

[120] M. Kerroumi *et al.*, “Unveiling electrochemical insights of lithium manganese oxide cathodes from manganese ore for enhanced lithium-ion battery performance,” *Electrochimica Acta*, vol. 509, p. 145286, Jan. 2025, doi: 10.1016/j.electacta.2024.145286.

[121] H. Fu, W. Xu, Z. Yu, L. He, and Z. Zhao, “Identifying electrochemical performance of LiFePO4 with different exposed crystal facets for voltammetric determination of Li+,” *Journal of Electroanalytical Chemistry*, vol. 973, p. 118672, Nov. 2024, doi: 10.1016/j.jelechem.2024.118672.

[122] J.-H. Weng, C.-Y. Lai, and L.-C. Chen, “Microfluidic amperometry with two symmetric Au microelectrodes under one-way and shuttle flow conditions,” *Electrochimica Acta*, vol. 297, pp. 118–128, Feb. 2019, doi: 10.1016/j.electacta.2018.11.128.

[123] J. Holmes, P. Pathirathna, and P. Hashemi, “Novel frontiers in voltammetric trace metal analysis: Towards real time, on-site, *in situ* measurements,” *TrAC Trends in Analytical Chemistry*, vol. 111, pp. 206–219, Feb. 2019, doi: 10.1016/j.trac.2018.11.003.

[124] Z. Liu *et al.*, “Electrochemical sensor integrated microfluidic device for sensitive and simultaneous quantification of dopamine and 5-hydroxytryptamine,” *Sensors and Actuators B: Chemical*, vol. 273, pp. 873–883, Nov. 2018, doi: 10.1016/j.snb.2018.06.123.

[125] K. Hyun, J. Lee, S. Kang, and Y. Kwon, “Effect of the protection layer formed by cross-linked gelatin on the stability and performance of glucose and oxygen fuel cells,” *Journal of Energy Chemistry*, vol. 61, pp. 155–162, Oct. 2021, doi: 10.1016/j.jechem.2021.01.033.